Modeling of High Impedance Surface Structures

Yu Zhu

N° 2011PA112081

THÈSE DE DOCTORAT

SPECIALITE : PHYSIQUE

Ecole Doctorale « Sciences et Technologies de l'Information des Télécommunications et des Systèmes »

Présentée par : Yu ZHU

Sujet : MODELISATION DE STRUCTURES A HAUTE IMPEDANCE

Soutenue le 29 juin, 2011 devant les membres du jury :

Saïd ZOUHDI	Professeur à Université Paris Sud	Directeur de la thèse
Alain BOSSAVIT	Chercheur à Laboratoire de Génie Electrique de Paris	Co-directeur
Alain PRIOU	Professeur à Université Paris Ouest Nanterre la Défense	Rapporteur
Xavier BEGAUD	Maître de Conférences Habilité à Diriger des Recherches à Télécom Paris Tech	Rapporteur
Victor Fouad HANNA	Professeur à l'Université Pierre et Marie CURIE	Examinateur

Acknowledgment

This thesis explains all my work during my PhD study in the Group "ICHAMS" (Interaction Champs-Matériaux et Structures) of LGEP (Laboratoire de génie électrique de Paris) under the supervision of Professor Said Zouhdi. My first appreciation is due, of course, to my supervisor for offering me the opportunity to be able to work on this interesting topic for my thesis and for the guidance of bringing me into the metamaterial domain. During my study, many of his suggestions inspired me a lot.

I would like to express my deep gratitude to Professor Alain Bossavit for his helpful guidance, inestimable encouragements, fruitful discussion and unbelievable patience. He is such a kind person who not only passed his passion in scientific research to me, but also shaped and widened my knowledge in theory of electromagnetism and finite element methods. Furthermore, many thanks to his meticulous revision of the first draft of this thesis.

I also thank Hicham Belyamoun, Gislain Remy, Philippe Spruty for their help in fabricating the samples and testing the samples as well as Laurent Santandrea, Alejandro Ospina Vargas, Lionel Pichon for their help in understanding the finite element method and matlab programming.

Furthemore, I am thankful to my parents and all my family members for their encouragements during the whole course of my studies, especially to my grandmother Xiaoshan WANG, who devoted all her love on me from always and financially supported my study of Master Degree in France. The thesis will be in the memory of her, who passed away at the end my first year's PhD study.

Last but not least, I am also grateful to my colleagues in LGEP for their encouragements and supports.

Yu ZHU

Gif-sur-Yvette, April, 2011.

Résumé de la thèse en français

Introduction aux S.H.I.

Des plans métalliques sont fréquemment utilisés comme plan de masse pour une antenne. Ce plan fonctionne comme un réflecteur qui puisse diriger les ondes émises vers l'autre côté. Par conséquent, on isole la partie qu'on ne désire pas soumettre au rayonnement en ayant un gain de puissance d'environ 3 dB de l'autre côté. Cependant, si la distance à laquelle on place ce plan par rapport à l'antenne est très petite, la phase de l'onde à la réflection sera inversée par rapport à l'onde incidente. Tout cela va annuler l'onde émise par l'antenne ou tout au moins entraîner un rayonnement anormal ou inefficace. La solution classique consiste à mettre le plan métallique à une distance de l'antenne égale au quart de la longueur d'onde. Figure 1 montre que les ondes réfléchies interfèrent alors constructivement avec les ondes émises par l'antenne dans la direction désirée.

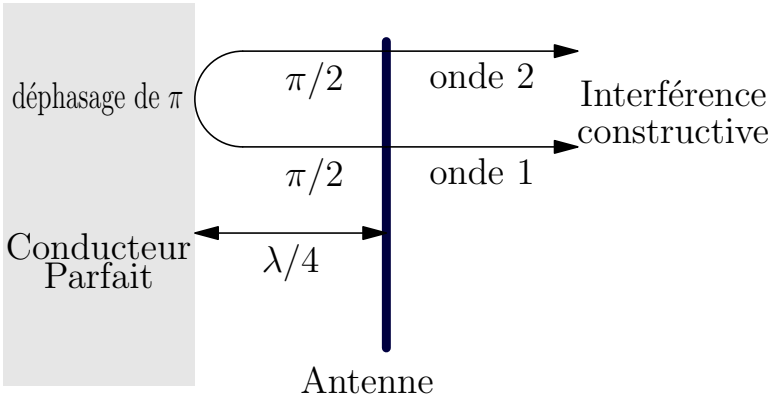

Figure 1 – Antenne avec conducteur parfait comme plan de masse

Un problème avec cette technique est qu'elle ne permet pas de faire des antennes compactes. Ce n'est pas son seul inconvénient. On sait que, dans l'environnement électromagnétique, les courants de fuite se propagent à la surface du conducteur et vont générer du rayonnement

lorsqu'ils arrivent à un bord ou un coin. De ce fait, des interférences non souhaitables vont être générées à l'extrémité des plans du conducteur. Les structures de Surface à Haute Impédance (SHI) ont été proposées pour remédier à ces défauts.

La structure de « Surface à haute impédance » peut être considérée comme un assemblage d'éléments périodiques et présente une impédance très élevée dans une ou plusieurs bandes de fréquences déterminées. La structure général consiste en une surface sélective en fréquence en haut, un substrat au milieu et un plan métallisé en bas. Une géométrie de structure SHI en champignon a été montrée en Fig. 2 et en Fig. 3. Cette structure peut être modélisée comme un réseau équivalent avec les éléments de capacitance et d'inductance en parallèle. La capacitance est due à l'étroitesse de l'espace entre les deux motifs métalliques sur la surface en haut et l'inductance résulte du cylindre métallique (appelé « via ») qui relie la surface du haut au plan de masse en bas.

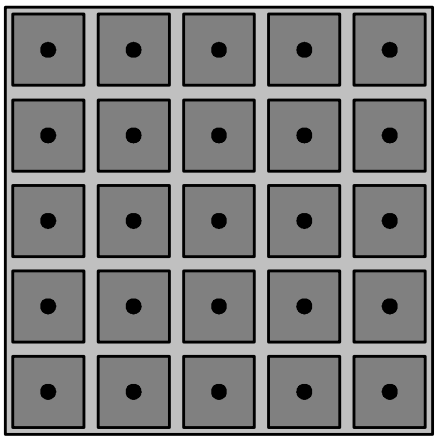

FIGURE 2 – Géometrie de structure SHI en champignons, vue de dessus

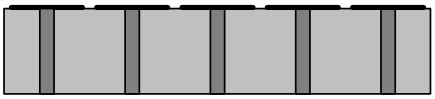

FIGURE 3 – Géometrie de structure SHI en champignons, vue de côté

Dans la gamme de fréquences où l'impédance de surface est extrêmement élevée, le champ magnétique tangentiel sur la surface est presque nul. Une telle structure peut donc être appelée Conducteur Magnétique Parfait (CMP). Si un dipôle simple est adjacent à un plan de masse fait d'un CMP, le courant image va générer une interférence constructive plutôt qu'une interférence destructive. Donc, théoriquement, la surface CMP est un matériau idéal pour fabriquer le plan de masse d'une antenne. Malheureusement, ce type de matériaux n'existe pas dans la nature.

Dans [31], l'auteur a effectué des simulations numériques avec une antenne de dipôle placée très près des trois types de plan de masse : le plan totalement métallique (autrement dit le plan en Conducteur Electrique Parfait, CEP), le plan en CMP et le plan en SHI. Nous avons refait ces mêmes simulations à l'aide du logiciel CST microwave studio. La perte d'adaptation de chaque

cas a été testée et les résultats ont été présentés en Fig. 4. Ils montrent que le rayonnement de l'antenne dans le cas du plan CEP est totalement perturbé. Le plan CMP ne donne plus un bon résultat en raison d'un mauvaise adaptation à l'impédance d'entrée. Parmi les trois cas, la meilleure solution est donnée par le plan en SHI qui se comporte comme un plan CMP dans une bande de fréquences autour de sa résonance, sans aucun problème de découplage.

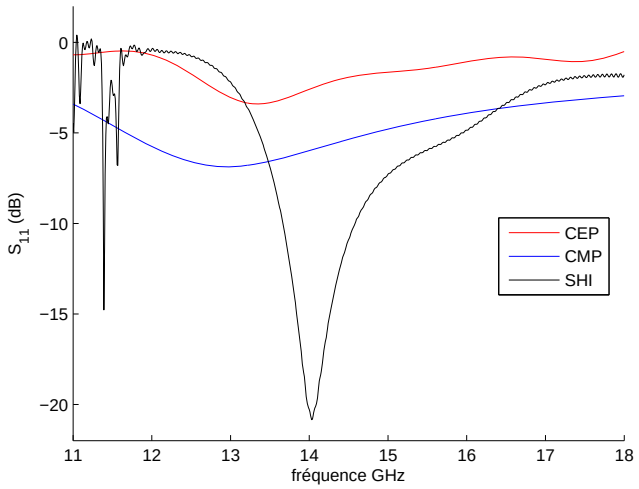

FIGURE 4 – Perte d'adaptation simulé avec une dipôle placée près d'un plan de masse de trois types

En résumé, au sein d'une certaine bande de fréquences, les SHI peuvent améliorer le gain d'une antenne et réaliser un meilleur couplage de circuits, tout en supprimant les ondes de surface non désirées. Un autre avantage de l'utilisation de cette structure est que le champ électrique réfléchi est en phase avec le champ incident plutôt qu'en opposition de phase (phase 180°) d'où une réduction d'épaisseur (voir Fig. 5). Grâce à ces propriétés, les structures de SHI se sont révélées de bons candidats pour améliorer leurs performances ou réduire les dimensions des antennes.

Depuis l'introduction des SHI par D.F. Sievenpiper en 1999 [22], diverses géométries sont été proposées et examinées. Dans notre travail, la structure SHI en champignons avec patchs carrés est étudiée d'abord, car elle est simple et flexible en même temps qu'elle bénéficie d'une bande passante relativement large. Un inconvénient de cette structure est que son impédance de surface est sensible à l'angle d'incidence, vu que la surface du haut de la structure SHI est largement couverte par du métal et qu'il n'est donc pas facile pour l'onde de pénétrer à l'intérieur du substrat. Afin d'avoir un résultat plus stable par rapport à la variation de l'angle d'incidence, une structure de SHI avec croix de Jérusalem dessus, dont la surface est moins métallique, est

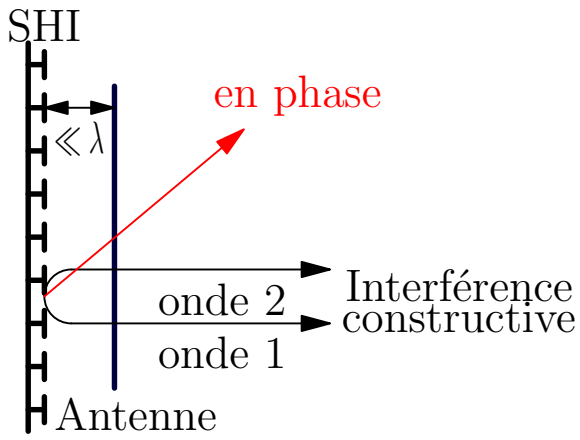

FIGURE 5 – Antenne avec SHI comme plan de masse

étudiée ensuite. Après avoir examiné les deux premières structures, qui sont symétriques par rapport à la diagonale du motif de surface, on continue la recherche sur quelques structures asymétriques, par exemple, celle en forme de fourchette, celle en forme de la lettre F, etc.

Loin d'être un sujet d'étude académique, les structure de SHI ont déjà ouvert la porte à beaucoup d'applications : renforcer la directivité de l'antenne [47], supprimer les bruits de commutation [49, 50], réduire le couplage mutuel entre éléments adjacents [51], etc. Elles sont donc vraiment intéressantes à étudier.

Modélisation Analytique des S.H.I.

Dans la littérature, différents modèles analytiques ont déjà été proposés et appliqués aux structures SHI. De tels modèles analytiques permettent de donner une prédiction rapide des caractéristiques de structures SHI simples et de comprendre certains comportements liés à la géométrie de la structure.

Premièrement, on étudie un modèle à éléments localisés, proposé par Sievenpiper [22] et applicable à la structure de SHI en champignons carrés (voir Fig. 6). Le circuit équivalent de cette structure est modélisé comme une combinaison de capacitance et inductance en parallèle (voir Fig. 7). L'impédance équivalente de cette structure est définie comme :

$$Z_s(\omega) = \frac{j\omega L}{1 - \omega^2 LC}, \tag{1}$$

où, l'inductance L et la capacité C sont déterminées par la géométrie de structure de SHI, avec :

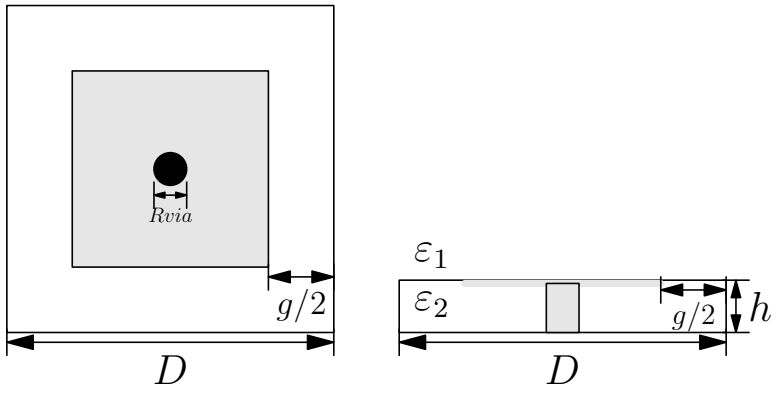

FIGURE 6 – Géométrie d'une cellule de structure SHI en champignion

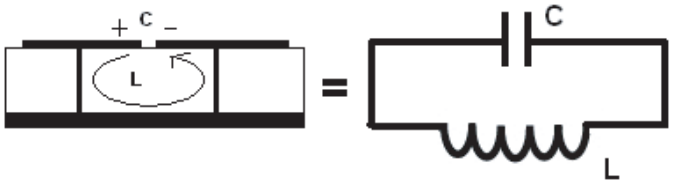

FIGURE 7 – Circuit équivalent pour une cellule de structure SHI en champighion

$$C = \frac{(D-g)(\varepsilon_1+\varepsilon_2)}{\pi} cosh^{-1}\left(\frac{D}{g}\right), \tag{2}$$

où D est la période d'une cellule élémentaire, g est l'espace entre deux patchs, $\varepsilon_1 = \varepsilon_0$ et $\varepsilon_2 = \varepsilon_0\varepsilon_r$ est la permittivité des deux milieux à côte du patch ;

$$L = \mu h, \tag{3}$$

où μ et h est la perméabilité et la hauteur du substrat.

Deuxièmement, un modèle d'une ligne de transmission en régime quasi statique a été proposé par Simovski [79]. Figure 8 représente le principe de ce modèle en utilisant un exemple de structure en champignon. L'impédance surfacique Z_s de la structure de SHI est considérée comme la mise en parallèle d'une impédance de substrat Z_d et d'une impédance de grille Z_g :

$$Z_{s\,(input)} = \left(Z_g^{-1} + Z_d^{-1}\right)^{-1}. \tag{4}$$

Ce modèle d'une ligne de transmission, basé sur la théorie de l'homogénéisation, est valable

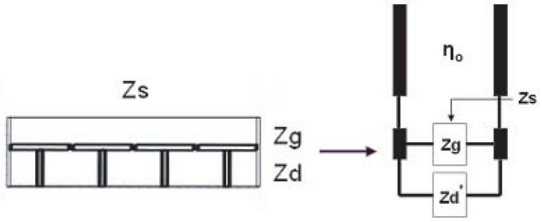

Figure 8: Modèle d'une ligne de transmission appliqué à la structure SHI en champignions

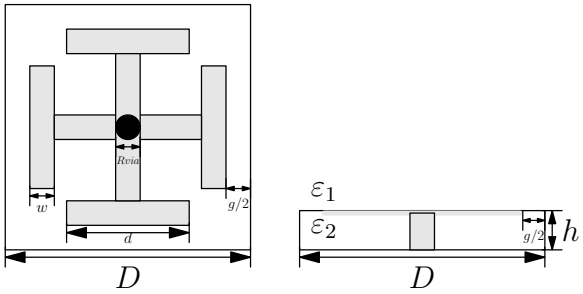

Figure 9: Géométrie d'une cellule de structure SHI en croix de Jérusalem

quand la longueur de l'onde effective est très supérieure à la dimension de chaque cellule de la structure de SHI. Selon la polarisation de l'onde d'excitation, les expressions de Z_d et Z_g sont comme ci-dessous :

$$Z_d^{TE} = \frac{j\eta_0}{\sqrt{\varepsilon_r - sin^2\theta}} \tan(k_{zd}h),\ Z_d^{TM} = \frac{j\eta_0}{\sqrt{\varepsilon_r}} \tan(k_{zd}h), \tag{5}$$

$$Z_g^{TE} = \frac{1}{j\omega C_g \cos^2\theta},\ Z_g^{TM} = \frac{1}{j\omega C_g}. \tag{6}$$

En effet, le modèle d'une ligne de transmission peut aussi être appliqué à la structure de SHI en croix de Jérusalem (voir Fig. 9). Pour cette structure, l'impédance de substrat peut être traitée comme dans le cas de la structure en champignons, l'impédance de grille étant définie comme :

$$Z_g^{TE} = (j\omega L_g^{JC} + \frac{1}{j\omega C_g^{JC}}),\ Z_g^{TM} = cos^2\theta((j\omega L_g^{JC} + \frac{1}{j\omega C_g^{JC}}). \tag{7}$$

En troisième lieu, on examine également deux autres modèles analytiques. L'un est proposé par Olli [102], qui combine la conception d'une ligne de transmission, le principe de Babinet

et la théorie de l'homogénéisation, et surtout améliore la précision du calcul de l'impédance surfacique dans le cas d'une onde incidente oblique. Un autre est proposé par Hosseini [81], qui considère l'influence de plan de masse sur l'impédance du substrat.

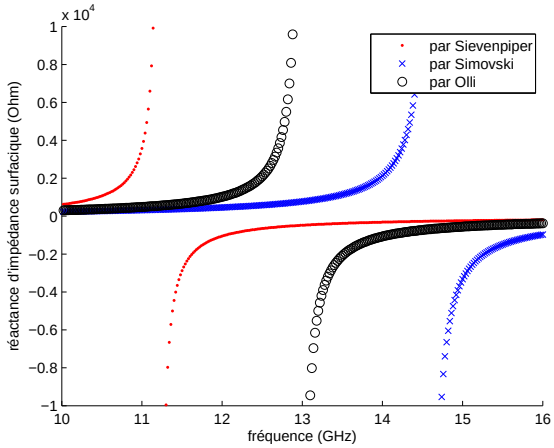

FIGURE 10 – Comparaison d'impédance surfacique des différents méthodes analytiques avec la structure en champignon (D = 10mm, g = 5mm, h = 2mm, $\varepsilon_r = 4.4$)

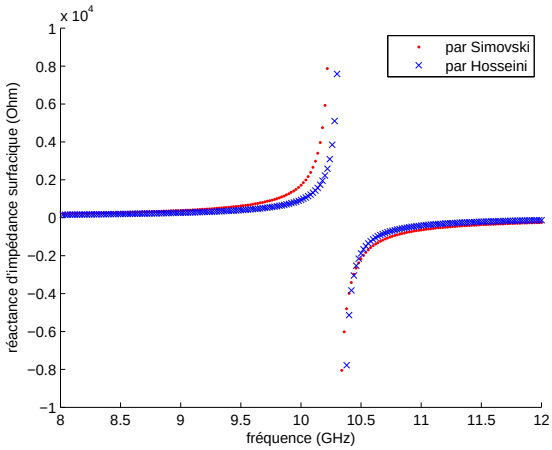

FIGURE 11 – Comparaison d'impédance surfacique des différents méthodes analytiques avec la structure en croix de Jérusalem (D = 2.4mm, g = 0.4mm, d = 1.4mm, w = 0.2mm, h = 3mm, $\varepsilon_r = 4.4$)

Enfin, on effectue une étude sur les paramètres de géométrie et on compare les résultats calculés par différentes méthodes. Figure 10 montre une comparaison de résultats de trois modèles analytiques différents concernant la structure en champignons carrés. Figure 11 montre un exemple relatif à la structure en croix de Jérusalem.

En règle générale, les modèles analytiques ne sont pas très rigoureux, en raison de l'ignorance sur le comportement des capacité et des inductances à haute fréquence. La précision de modèle s'améliore lorsqu'on diminue la taille de la cellule de base, puisqu'on s'approche de la zone de validité de l'homogénéisation.

Modélisation Numérique des S.H.I.

Modèle Numérique

Si les modèles analytiques donnent bien les caractéristiques de certaines structures de SHI, ils ne peuvent le faire pour des structures à géométrie complexe. C'est pourquoi plusieurs types de méthodes numériques sont proposés et adaptés aux structures de SHI.

Dans notre travail, la méthode des éléments finis avec éléments d'arête a été choisie comme méthode numérique. On prendra un exemple de structure SHI en champignons et on expliquera les détails de la construction du modèle numérique (voir Fig. 12). Grace à la symétrie de la cellule de base, l'analyse de l'ensemble d'une structures SHI peut être réduite à celle d'une cellule élémentaire.

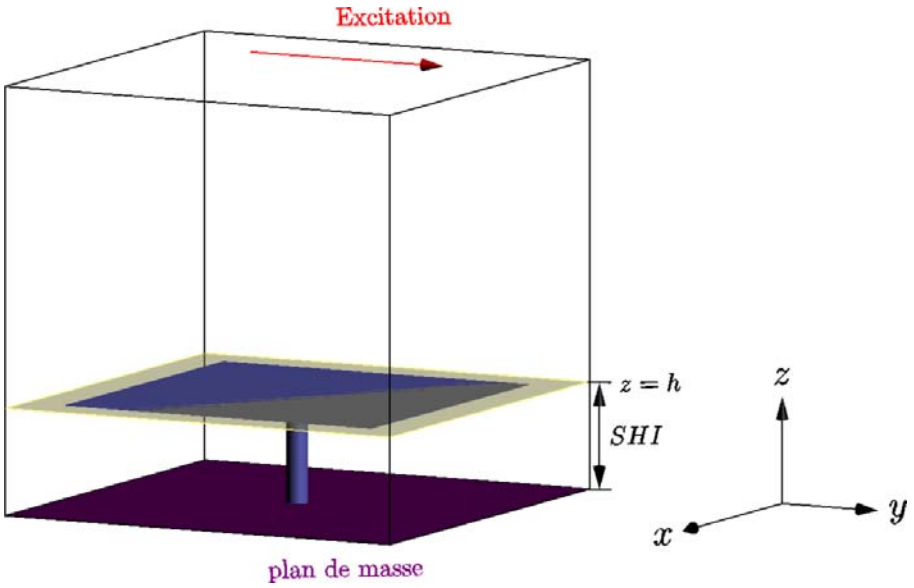

FIGURE 12 – Modélisation numérique d'une cellule de structure SHI

1) Le plan xoy est le plan de base du domaine d'étude et aussi représente le plan de masse de la structure. Dans la modélisation numérique, la condition à la limite CEP va être appliquée à cette surface.

2) La région intermédiaire ($0 < z < h$) représente le substrat, avec une certaine perméabilité et une certaine permittivité. Les deux peuvent être complexes, et dépendre de la fréquence, mais sont des valeurs constantes dans notre travail.

3) La surface du haut de la structure SHI se trouve à $z = h$. Si la structure possède une fine colonne liant le plan de masse à la surface du haut en traversant le substrat, on peut ajouter un cylindre fin entre $z = 0$ et $z = h$. La condition à la limite CEP va être appliquée à tous les éléments métalliques.

4) La région $z > h$ correspond à l'espace libre.

5) L'excitation est un champ électromagnétique alternatif, produit par un champ éléctrique homogène à la surface en haut du domaine d'étude. Cette surface va être traitée numériquement comme portant une condition de Dirichlet.

6) Si la structure de SHI est symétrique et l'incidence d'onde est normal, deux types de conditions aux limites peuvent être utilisées aux quatre murs autour du domaine d'étude. 1) appliquer directement deux groupes de conditions périodiques ; 2) appliquer des conditions CEP à deux surfaces opposées et des conditions CMP aux deux autres surfaces, en respectant l'orientation de l'excitation. Un exemple de ces deux propositions est donné dans la Figure 13.

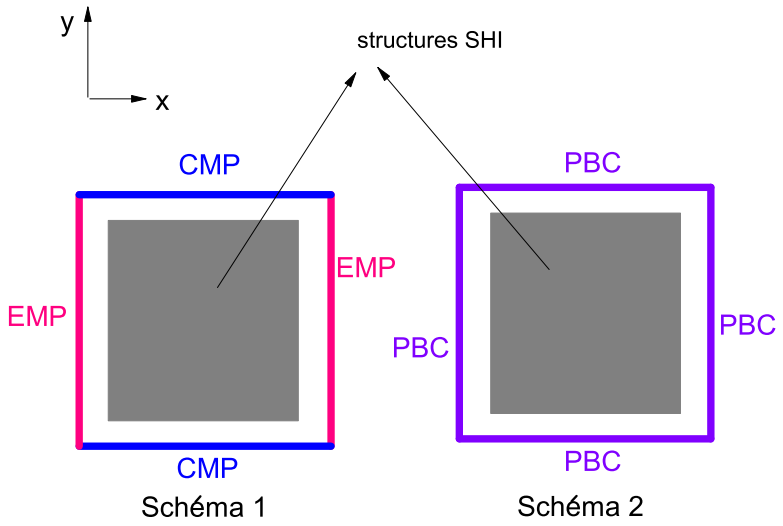

FIGURE 13 – Deux shémas de condition aux limites appliqués à la structure de SHI symétrique. (L'excitation de champ électrique est parallèle à l'axe x.)

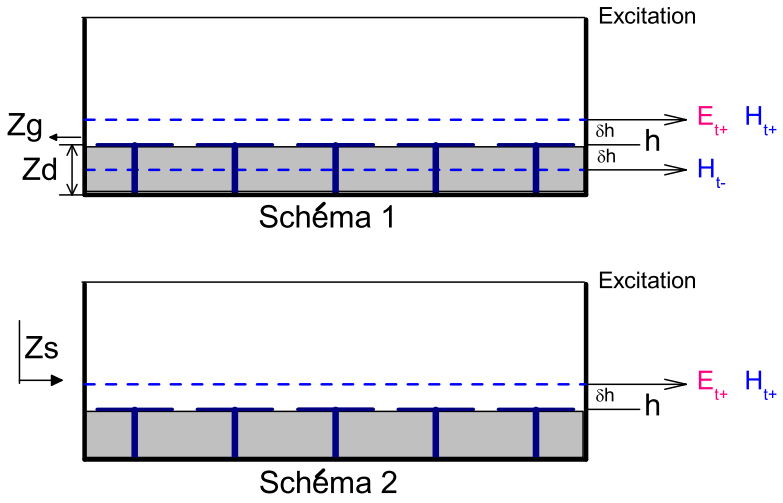

FIGURE 14 – Deux schémas de modèle pour calculer l'impédance surfacique de structure SHI

Au début de la modélisation, on a essayé de calculer l'impédance surfacique selon deux

schémas (voir Fig. 14). Dans le Schéma 1, Z_s s'obtient par un calcul mi-analytique et mi-numérique :

$$Z_s(schéma\ 1) = \frac{Z_g(numerical) \cdot Z_d(analytical)}{Z_g(numerical) + Z_d(analytical)}, \tag{8}$$

avec Z_g , obtenu par un calcul numérique et défini comme :

$$\langle Z_g \rangle = \frac{\langle E_{t+} \rangle}{\langle H_{t+} \rangle - \langle H_{t-} \rangle}, \tag{9}$$

où $t+$ representes les valeurs tangential sur un plan d'observation au-dessus de la surface du haut de la SHI ; $t-$ represente les valeurs tangentielles sur un plan d'observation au-dessous de la surface du haut de la SHI ; $< X >$ dénote la moyenne de la quantité X et Z_d, est calculé par la méthode analytique de l'équation 5.

Dans le Schéma 2, on suppose que l'information électromagnétique sur la surface d'observation au dessus de la structure SHI peut bien représenter la réaction du bas. Donc, la définition de Z_s dépend des calculs du champ électromagnétique tangentiel sur la surface d'observation :

$$Z_s(schéma\ 2) = \frac{\langle E_{t+} \rangle}{\langle H_{t+} \rangle}. \tag{10}$$

Le Z_s calculé avec le Schéma 2 ne contient que le calcul numérique. Les valeurs de champ sont toutes des valeurs moyennes obtenues sur la surface.

Pour une structure SHI générale, Z_s est un opérateur en deux dimensions. Néanmoins, si la géométrie de la surface supérieure est symétrique par rapport à la diagonale de la cellule de base, le calcul de Z_s peut être simplifié comme suit :

$$Z_s = \begin{bmatrix} Z_{11} & Z_{12} \\ Z_{21} & Z_{22} \end{bmatrix} \Longrightarrow Z_s = \begin{bmatrix} Z_s & 0 \\ 0 & Z_s \end{bmatrix}. \tag{11}$$

Ainsi, un résultat 1D est suffisant pour reconstituer la matrice en 2D. Figure 15 compare les méthodes numériques et les méthodes analytiques appliquées au cas d'une structure SHI en champignons et Figure 16 donne la même comparaison pour une structure SHI en croix de Jérusalem. La tendance des résultats est la même, mais il existe des différences entre les méthodes analytiques et les méthodes numériques. Après une série de tests, il s'avère que la méthode numérique avec Schéma 1 est moins performante que les autres. En conséquence, ce schéma 1 a été éliminé dans les simulations suivantes.

La méthode numérique est validée, mais il est difficile de juger quelle méthode fonctionne le

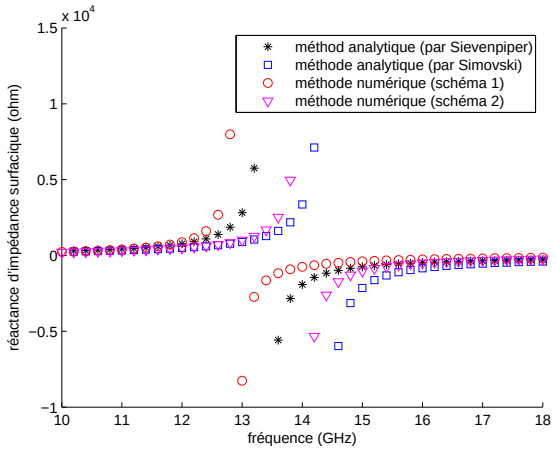

FIGURE 15 – Comparaison d'impédance surfacique entre les résultats analytiques et numériques (structure en champgninons)

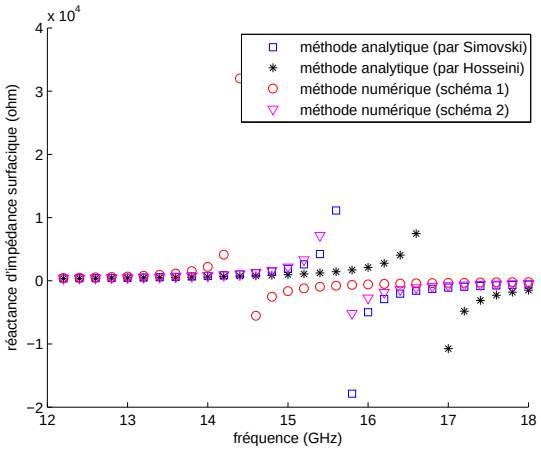

FIGURE 16 – Comparaison d'impédance surfacique entre les résultats analytiques et numériques (structure en croix de Jérusalem)

mieux sans référence à un résultat expérimental.

Deux nouvelles méthodes numériques en calculant l'impédance surfacique de structure SHI

Si la structure de SHI n'est pas symétrique, le calcul de l'impédance surfacique en 1D n'est pas suffisant pour récupérer toutes les caractéristiques de la structure SHI. On a donc proposé deux nouvelles méthodes numériques pour calculer l'impédance surfacique de structure SHI en 2D : la méthode du flux Poynting et la méthode dite « <E>/<H> ».

Dans ces deux cas, le problème du calcul de l'impédance surfacique revient à déterminer une condition d'impédance. Figure 12 présente notre problème dans un domaine d'étude cubique, qui ressemble à un guide d'onde. Ce domaine a été coupé en deux parties par une surface d'observation So : la partie du bas, comprenant les structures SHI, est considérée comme une boîte noire, et caractérisée par l'impédance surfacique sur So ; la partie du haut est un espace libre. Cette condition d'impédance est définie par le rapport entre les valeurs moyennes du champ magnétique tangentiel et du champ électrique tangentiel sur So :

$$n\times < H_S > +Y < E_S >= 0, \tag{12}$$

où Y représente une relation linéaire entre deux vecteurs complexes et s'interprète physiquement comme l'admittance de la surface. Quant à la matrice d'impédance surfacique, on s'obtient

facilement par inversion de Y en 2D.

Supposant la surface d'observation contenue dans le plan $x-y$, le champ électrique tangentiel sur cette surface est défini par ses deux composantes : E_{sx}, E_{sy}. En considérant deux excitations différentes, on note les champs correspondant à ces deux cas E_1, H_1 et E_2, H_2. .

Dans la méthode du flux de Poynting, l'impédance surfacique s'obtient à partir du flux qui traverse la surface d'observation. Ce flux est une fonction quadratique de E tangentiel, et l'admittance surfacique est la matrice Y_0 associée à cette forme. Dans ce cas, le système s'exprime par :

$$\int_D (i\omega\varepsilon E_i \cdot E_j + i\omega\mu H_j H_i) + \int_S (Y_0 \cdot E_{iS}) \cdot E_{jS} = 0. \ (i,j = 1,2) \tag{13}$$

Les quatre équations ci-dessus suffisent à obtenir les quatre entrées inconnues de la matrice Y_0.

Comparé avec la méthode du flux de Poynting, le calcul par la méthode dite <E>/<H> est un peu moins lourd, car il n'utilise que les champs électromagnétiques tangentiels sur la surface d'observation. Mais l'effort effectué dans le pré-calcul de la circulation du champ électrique sur les arêtes dans tout le domaine est le même. Dans ce cas, la matrice Y peut être obtenue par l'équation suivante :

$$\begin{bmatrix} -H_{1sy} & -H_{2sy} \\ H_{1sx} & H_{2sx} \end{bmatrix} = - \begin{bmatrix} Y_{xx} & Y_{xy} \\ Y_{yx} & Y_{yy} \end{bmatrix} \cdot \begin{bmatrix} E_{1sx} & E_{2sx} \\ E_{1sy} & E_{2sy} \end{bmatrix}. \tag{14}$$

Comparaisons entre les résultats analytiques, numériques et expérimentaux

Afin de s'assurer de la précision de nos méthodes numériques, quelques échantillons ont été fabriqués et mesurés. Dans le tableau 1 suivant, on prend la structure de champignons comme exemple et on compare les résultats obtenus par différentes méthodes. Avec le résultat expérimental comme référence, nos deux méthodes numériques fonctionnent correctement et mieux que les autres méthodes analytiques.

De plus, on teste non seulement les structures symétriques, mais aussi les structures asymétriques. La structure asymétrique ne se comporte pas de la même façon pour différentes orientations de l'excitation. Fig. 17 et Fig. 18 montrent les résultats correspondant à la structure SHI en champignons rectangulaires pour une excitation horizontale et une excitation verticale.

Fig. 19 et Fig. 20 montrent les résultats correspondant à la structure SHI en champignons carrés avec une fente rectangulaire sur le côté, également pour les deux orientations de l'excita-

Méthode	Résonance (GHz)	Bande passante (GHz)
Mesure	11.74	10.33 - 12.77
méthode analytique de Sievenpiper	11.2	9.3 - 13.6
méthode analytique de Olli	13	10.5 - 16
méthode analytique de Simovski	14.6	11.5 - 18.2
méthode numérique dite <E>/<H>	11.74	10.3 - 12.7
méthode numérique du flux de Poynting	11.5	10.2 - 12.4
Simulation CST	11.02	9.85 - 11.9

TABLE 1 – Comparaison de résoance et bande passante parmi différents méthodes avec structure SHI en champignons (Dimension de l'échantillon : D = 10 mm, g = 5 mm, h = 1.6 mm, ε_r = 4.4.)

tion.

Les courbes confirment que nos méthodes numériques sont capables de détecter les différentes résonances de structures asymétriques répondant aux différentes orientations d'excitation.

Discussions

Il est généralement admis que la longueur d'onde du signal doit être au moins 10 fois supérieure à la dimension de la cellule SHI lorsqu'on recourt à l'homogénéisation. Mais ceci n'a rien d'absolu, et au vu des résultats obtenus, le modèle numérique est encore valable quand le rapport est voisin de 7. Toutefois, les résultats autour de la résonance sont moins fiables, en raison du mauvais conditionnement de la matrice du système linéaire dans ce cas.

Dans la modélisation numérique, deux schémas différents, correspondant à différentes combinaisons de conditions aux limites, sont appliqués à la structure SHI symétrique. Le schéma combinant les conditions CEP et CMP a d'abord été choisi pour deux raisons : 1) Il est plus facile à programmer ; 2) Il demande moins de temps de calcul. Mais il a aussi deux inconvénients : 1) Exiger un maillage parfaitement symétrique par rapport au plan de symétrie médian, sinon on a un mauvais résultat ; 2) Ne pas s'adapter aux structures SHI asymétriques. Comme ses désavantages sont plus importants que ses avantages, ce schéma n'est pas à recommander, même pour des structures symétriques.

La finesse du maillage doit être considérée au début de simulation. Une série de simulations avec des maillages de finesses différentes a été faite pour trouver celui qui donne un résultat acceptable en un temps de calcul raisonnable. La finesse de maillage est donc déterminée par deux facteurs : la qualité des résultats et le temps de calcul.

La hauteur de la surface d'observation est importante dans la modélisation numérique. On

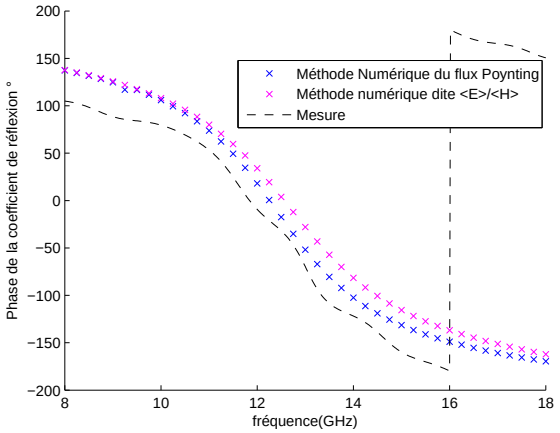

FIGURE 17 – Comparaison des résultats numériques avec la mesure (Polarisation verticale, échantillon réctangulaire : Dx = 4 mm, Dy = 6 mm, W = 7 mm, L = 9mm, h = 1.6 mm, $\varepsilon_r = 4.2$.)

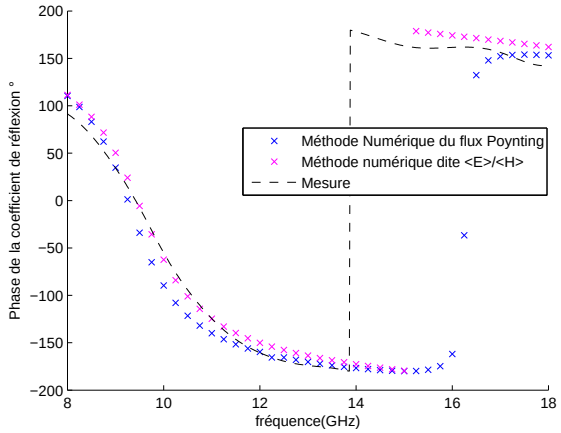

FIGURE 18 – Comparaison des résultats numériques avec la mesure (Polarisation horizontale, échantillon réctangulaire : Dx = 4 mm, Dy = 6 mm, W = 7 mm, L = 9mm, h = 1.6 mm, $\varepsilon_r = 4.2$.)

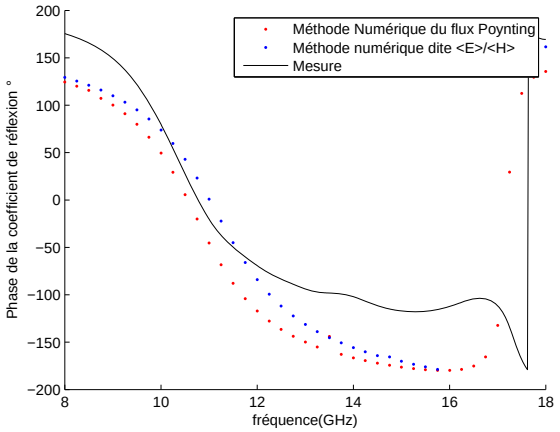

FIGURE 19 – Comparaison des résultats numériques avec la mesure (Polarisation horizontale, échantillon avec une fênte à côté du carré métal)

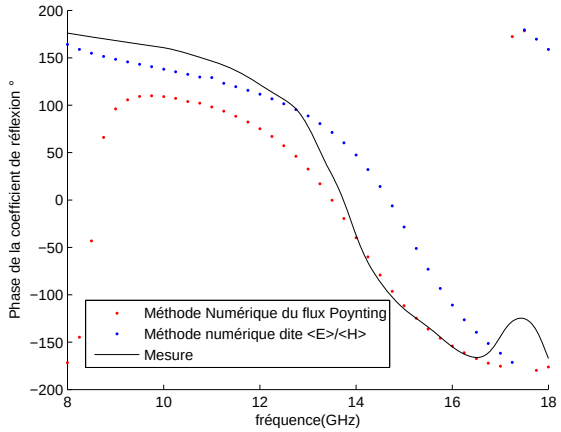

FIGURE 20 – Comparaison des résultats numériques avec la mesure (Polarisation verticale, échantillon avec une fênte à côté du carré métal)

sait que l'excitation au niveau de la surface du haut est uniforme, mais la présence de structures SHI va perturber le champ électromagnétique dans le domaine. En particulier, le champ électrique autour de cette structure est inhomogène. Théoriquement, plus la surface d'observation est haute, plus notre modèle numérique est valable. Cela semble indiquer que la hauteur devrait être aussi grande que possible. Mais par ailleurs, l'objectif de la modélisation des structures

SHI est de s'appliquer à un outil de simulation de l'antenne, et pour cela, la hauteur de la surface d'observation doit être inférieure à celle où se situe l'antenne. Par conséquent, on cherche une solution de compromis pour la hauteur de la surface d'observation en tenant compte des différentes conditions.

En outre, on trouve que la méthode du flux de Poynting fonctionne mieux si le maillage de la surface d'observation est un sous-maillage de du maillage tridimensionnel. On dira dans ce cas que la surface d'observation est "prédéfinie". Par contre, le fait de prédéfinir ainsi une surface d'observation peut dégrader le résultat avec la méthode <E>/<H>.

Un Modèle Equivalent pour les S.H.I.

Principe

Du fait de la complexité et de la diversité des structures SHI, des éléments minuscules exigent un raffinement du maillage dans les simulations numériques, ce qui entraîne une grosse dépense à la fois en mémoire et en temps de calcul.

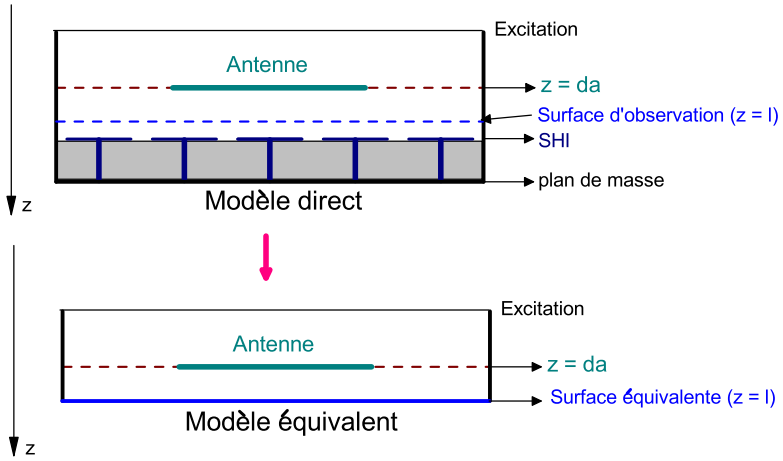

FIGURE 21 – Concept de modèle équivalent

L'idée de principe d'un modèle équivalent est représentés dans la Fig. 21. Le modèle avec tous les motifs SHI détaillés s'appelle « modèle direct » et le modèle avec la couche homogène, qui remplace tous les structures hétérogènes, s'appelle « modèle équivalent ». Pour construire ce modèle équivalent, on a besoin de trois étapes : 1) Choisir une surface d'observation dans le modèle direct à la hauteur l (On note que l doit être supérieur à la hauteur de structure SHI, et inférieur à la position de l'antenne da.) ; 2) Calculer l'impédance surfacique à la surface

d'observation dans le modèle direct et couper le modèle direct en deux parties avec la surface d'observation ; 3) Construire le modèle équivalent en gardant la même taille pour la partie haute du modèle direct, dont la surface en bas sera équipée de la condition d'impédance.

Simulation

Afin de vérifier l'efficacité du modèle équivalent, on compare le champ électrique dans le modèle direct et dans le modèle équivalent en prenant un exemple de structure en champignon sans via ($D = 10\,mm$, $g = 4\,mm$, $h = 1.6\,mm$, $\varepsilon_r = 4.3$). Dans le modèle direct, deux lignes d'observation ont été choisies : la ligne 1, qui traverse le patch métallique, et la ligne 2, qui se trouve dans l'intervalle entre le patch et la frontière du domaine d'étude (voir Fig. 22). Dans le modèle équivalent, les résultats sur n'importe quelle ligne verticale sont les mêmes. Donc, deux lignes d'observation sont aléatoirement sélectionnées (vue dans la Fig. 23).

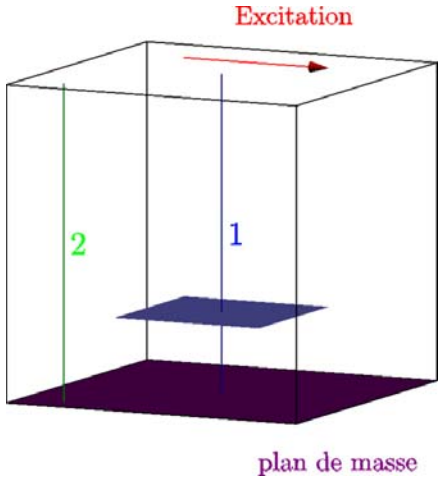

Figure 22: Lignes d'observation dans le modèle direct

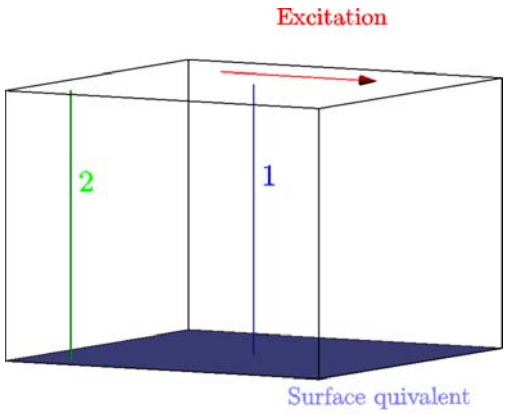

Figure 23: Lignes d'observation dans le modèle équivalent

Dans la dernière partie, on a presenté deux méthodes numériques pour calculer l'impédance surfacique de structure SHI. Ici, on va constuire le modèle équivalent à partir des résultats d'impédance surfacique obtenus par ces deux méthodes.

Dans la Fig. 24, on trouve quatre résultats différents, dont deux corrrespondent aux calculs dans le modèle direct et deux autres à ceux avec modèle équivalent. La courbe noire correspond à la ligne d'observation dans le modèle direct, traversant le patch. Une atténuation du champ électrique est manifeste à la hauteur de ce patch vers z = 1.6 mm. La courbe verte correspond à la ligne qui ne touche pas le patch. Donc, il n'y a pas d'atténuation du champ électrique au niveau du patch. Les résultats obtenus par le modèle équivalent ressemblent tous à celui du

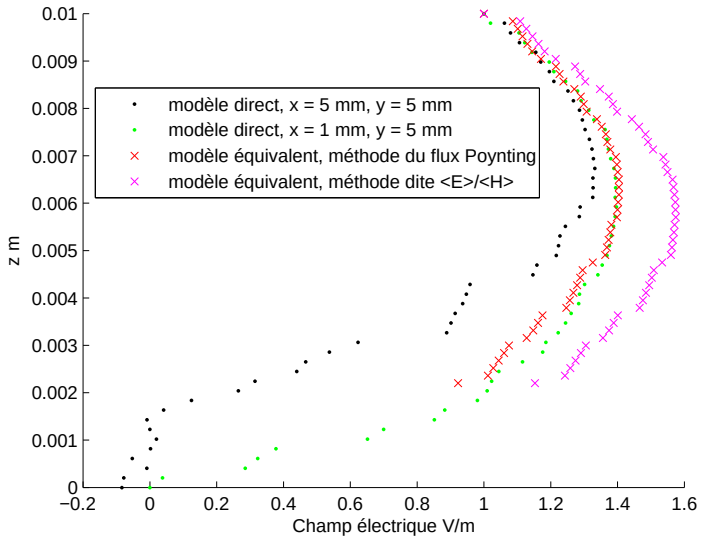

Figure 24: Comparaison de champ électrique entre le modèle direct et le modèle équivalent

modèle direct, avec toutefois quelques différences. Ce phénomène est normal, puisque le modèle équivalent ne peut pas se comporter assez finement que le modèle direct, surtout autour de la région où le patch produit une réaction forte. Même si le modèle offre seulement un résultat approché, la réduction du temps du calcul peut compenser ce défaut.

Discussion

Quand on construit le modèle équivalent, la finesse de maillage doit être bien considérée. Comme mentionné plus haut, on compare le temps de calcul et la qualité du résultat afin de décider de la finesse. De plus, on trouve que le modèle équivalent se comporte moins bien quand la fréquence d'opération est proche de la résonance. Cela est également dû à un mauvais conditionement de la matrice du système linéaire au viosinage de la résonance. La Méthode de déflation peut être utilisé pour améliorer la précision des résultats autout de la résonance.

Le modèle équivalent se forme par une couche homogène, caractérisée par l'impédance surfacique de la structure de SHI. Cette valeur peut être obtenue par deux méthodes : la méthode du flux de Poynting et la méthode dite « <E>/<H> ». Après une série de tests, on trouve que l'influence de la hauteur de surface d'observation sur la première méthode est faible. Par contre, les résultats de la deuxième méthode sont sensibles à la variation de la hauteur d'observation. On trouve également que la différence est plus évidente losque la fréquence d'opération s'approche de la résonance.

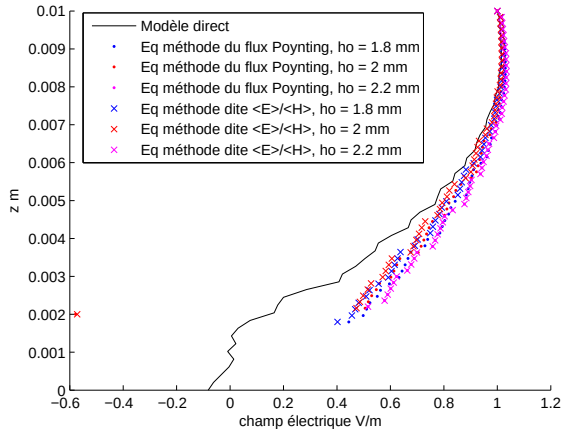

FIGURE 25 – Comparaison entre la méthode du flux Poynting et la méthode dite <E>/<H> avec la structure de champignions à 8 GHz.

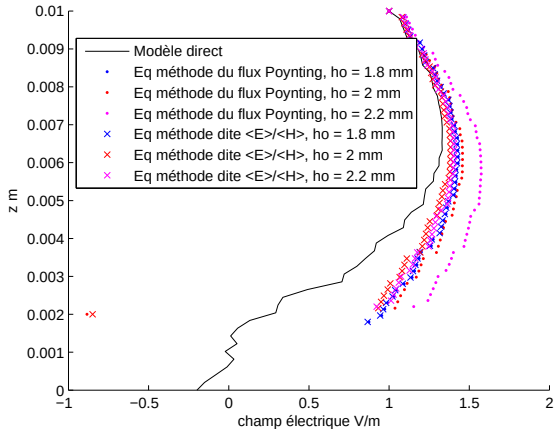

FIGURE 26 – Comparaison entre la méthode du flux Poynting et la méthode dite <E>/<H> avec la structure de champignions à 10 GHz.

Deux résultats de simulations sont montrés dans la Fig. 25 et la Fig. 26. Ils montrent que la méthode dite « <E>/<H> » marche toujours mieux que la méthode du flux Poynting. De plus, la surface d'observation prédéfinie dans le maillage n'améliore pas forcément le résultat de la méthode du flux de Poynting. Pour le moment, on n'a pas réponse claire à ce problème.

Organisation de la thèse

Au cours de la dernière décennie, les métamatériaux (MTM) ou plus particulièrement les Surfaces à Haute Impédance (SHI) ont suscité un grand intérêt dans le monde. Ces structures ont déjà été largement étudiées pour améliorer toutes sortes de performances des antennes, comme le gain, le facteur de qualité, les formes et dimensions.

Une question a été posée : Comment intégrer de telles structures dans le système de l'antenne afin de répondre aux différents besoins ? En conséquence, l'objectif de cette thèse est de modéliser les structures de SHI et de caractériser leurs performances en vue de futures applications aux antennes.

Ce mémoire commence par une brève introduction aux métamatériaux, vu que les structures SHI appartiennent à cette famille de matériaux. L'essentiel du premier chapitre est consacré à une introduction aux SHI, y compris leur histoire, leurs performances, leurs diverses géométries et leurs applications. Dans ce chapitre, on présente aussi, brièvement, la méthode des éléments finis. Tous les concepts et formalisation présentés ont un lien avec notre modèle numérique des

structures de SHI. Par ailleurs, on évoque aussi les techniques de programmation correspondant au problème.

Dans le Chapitre 2, nous étudions quelques modèles analytiques fréquemment traités dans la littérature. Cela nous aide à mieux comprendre les propriétés des SHI et nous donne une référence pour l'étude numérique plus tard. Deux structures parmi celles les plus souvent étudiées (la structure en champignons et la structure en croix de Jérusalem) sont choisies et l'effort principal est mis sur la façon de calculer l'impédance de surface. Une étude de paramétrage a également effectué afin de mieux comprendre les structures SHI.

Dans le Chapitre 3, nous proposons des modèles numériques basés sur la méthode des élément finis (MEF) en considérant différents schémas et différents choix de conditions aux limite. On reprend les mêmes structures de SHI introduites dans le deuxième chapitre et on valide le modèle numérique par des comparaisons entre les différents résultats analytiques et numériques. En outre, de nombreuses analyses ont été effectuées pour vérifier l'efficacité de ce modèle. Ensuite, deux nouvelles méthodes numériques sont proposées pour calculer l'impédance de surface d'une structure SHI : la méthode du flux de Poynting et la méthode dite « <E>/<H> ». Ces deux méthodes sont validées sur des structures symétriques, puis mises en oeuvre sur des structures asymétriques.

Dans le Chapitre 4, quelques échantillons ont été fabriqués et testés. Ces mesures expérimentales sont effectuées afin de vérifier la précision des nouvelles méthodes numériques.

Dans le Chapitre 5, nous présentons un modèle équivalent basé sur l'idée de remplacer les structures hétérogènes de SHI par une surface homogène, caractérisée par son impédance surfacique. Ce modèle nous permet d'avoir une prédiction avec un temps de calcul et une qualité de mémoire PC largement réduits. Un tel modèle pourrait être intégré dans un outil de simulation afin d'offrir une prédiction rapide des caractéristiques des antennes au stade de la conception de celles-ci.

En conclusion, nous évoquerons les perspectives possibles de cette étude concernant l'amélioration du modèle.

Contents

Abstract

High impedance surfaces (HIS), as one kind of metamaterials, have proved to be good candidates for antenna miniaturization or improving antennas performance. Within a certain frequency band, they can enhance the gain of an antenna while simultaneously suppressing the unwanted surface waves. Thanks to these two properties, a better coupling to the surrounding circuits and more desirable antenna's radiation patterns can be achieved.

In this thesis, the performances of different HIS structures have been investigated. The focus of our work is on numerical modeling of these structures by using the finite element method (FEM) based on edge elements.

One of our contributions is that we put forward two new numerical methods (the Poynting flux method and <E>/<H> method) to calculate the surface impedance not only for HIS structures with symmetric geometries, but also for those with asymmetric geometries. These two numerical methods have been validated through the comparison among analytical, numerical and experimental results, so we believe they can be used to characterize HIS structures.

Another significant contribution of the thesis is that we introduce an equivalent model, based on the idea of replacing the heterogeneous HIS structures by an homogeneous surface, characterized by its surface impedance. In comparison with the normal model, adopting this equivalent model can save computing time and memory space. The preliminary results indicate that such kind of model could be integrated into some emulation package so as to give some initial insights on the antenna design.

A short summary and a future outlook about optimization of our numerical method are given at the end of this dissertation.

keywords: High Impedance Surface (HIS), Homogenization, Finite Element Method (FEM), Surface Impedance.

Chapter 1

Introduction

1.1 Metamaterials

The word "meta", in Greek language, means beyond. It implies that the electromagnetic response of metamaterials (MTMs) is unachievable or unavailable in conventional materials.

Many efforts have been done to search for an adequate definition for MTMs. In 2002, J.B. Pendry wrote in a conference paper: "meta-materials, materials whose permeability and permittivity derive from their structure". Later, in 2006, C. Caloz and T. Itoh wrote: "Electromagnetic metamaterials are broadly defined as artificial effectively homogeneous electromagnetic structures with unusual properties not readily available in nature" [1]. Perhaps, a serious obstacle on the road to a universal definition for the term MTMs is the fact that researchers working with these objects do not commonly agree on their most essential characteristics. In [2] and [3], some of the problematic aspects of the non-naturality definition were raised, like the difficulty in separating classical composites from the new class of metamaterials. Another argument against the "not found in nature" property is that it unnecessary excludes impressive examples of natural media that could be called metamaterials par excellence, such as structural colors [4].

MTMs cover an extremely large scientific domain which ranges from optics to nanoscience and from material science to antenna engineering. In this thesis, we focus primarily on the subject of MTMs in the electromagnetic field. Personally, I prefer the definition given by D.R. Smith: Electromagnetic metamaterials are artificially structured materials that are designed to interact with and control electromagnetic waves [5]. The term "artificial" refers to the fact that the electromagnetic response of these materials is dominated by scattering from periodically or amorphously placed inclusions (e.g., metallic or dielectric spheres, wires, and loops) [6].

In the family of MTMs, "left-handed" (LH) media drew an enormous amount of interest.

This concept was first put forward by a Russian physicist, Victor Veselago, in 1968, for whom the medium is characterized by a simultaneously negative electric permittivity and negative magnetic permeability [7]. Veselago argued that such media are allowed by Maxwell's equations and that electromagnetic plane waves can propagate inside them, but the phase velocity of such a plane wave is in the opposite direction of the Poynting vector. Hence, some researchers use the term "backward wave media" (BWM) to describe these LH materials [8]. When such media are interfaced with conventional dielectrics, Snell's Law is reversed, leading to the negative refraction of an incident plane wave as shown in Fig. 1.1. Nevertheless, Veselago's conjecture was essentially ignored for thirty years due to the absence of naturally occurring materials or compounds that possess simultaneously negative permittivity and permeability.

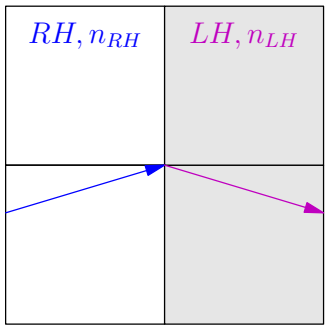

Figure 1.1: A negative reflection

In 2000, a metamaterial, based on conducting wires [9] and split-ring resonators (SRRs) [10], was demonstrated to have a negative refractive index over a certain range of microwave frequencies [11]. Wires, either continuous or with periodic breaks, can provide a positive or a negative effective permittivity. Planar SRRs or wound coils (also known as Swiss Rolls) can provide a positive or a negative effective permeability. One geometry of the conducting wires and SRRs is shown in Fig. 1.2 (a), and a photo of the real fabricated sample is shown in Fig. 1.2 (b). Since the birth of this structure, the conduction wire and SRR inclusions with their variations have been widely used as the fundamental building blocks in artificial materials to provide tailored artificial electric and magnetic responses [12]. Harnessing the phenomenon of negative refraction, these metamaterials offer a good potential for all kinds of applications, such as "perfect" lens [13], imaging [14], resonators [15], and cloaking [16].

Metamaterials possessing these properties are also frequently named "Negative Refractive Index (NRI)" and "Double Negative (DNG) material". In addition to the materials with simultaneously negative permittivity and negative permeability, the single negative metamaterials have also drawn a great interest. Applications are found for these materials either with a negative

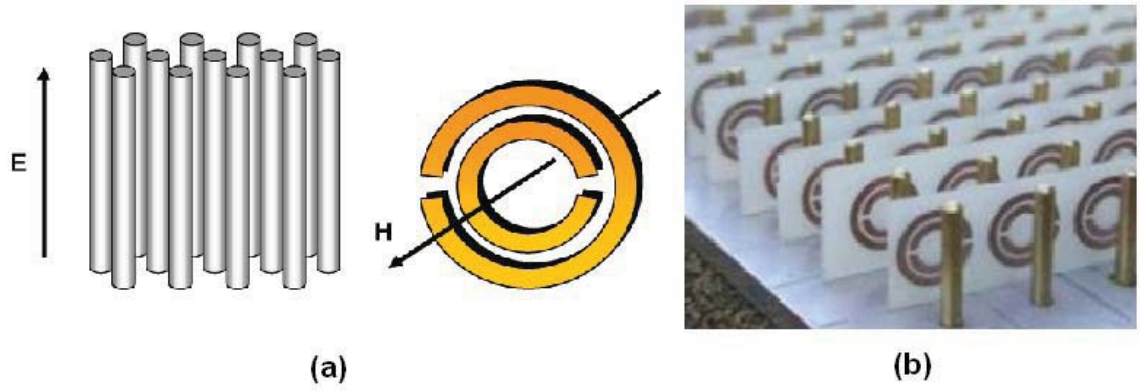

Figure 1.2: (a) Array of thin metallic wires mimicking microwave plasma with negative permittivity for electric fields and splitring resonator (SRR) particle yielding negative permeability for magnetic fields as shown (b) Photo of a real wire and SRRs sample

permittivity "Epsilon Negative (ENG)" [17] or a negative permeability "Mu Negative (MNG)" [18]. Besides, materials with the properties of "Epsilon Near Zero (ENZ)" [19] and "Mu Near Zero (MNZ)", known as "nihility" materials have also been studied. A simple synopsis of these metamaterials can be found in Fig. 1.3, where the angular frequencies ω_{pe} and ω_{pm} represent respectively the electric and magnetic plasma frequency [20].

Up to now, we talked about metamaterials who exhibit their great performances by artificially tailoring the permittivity or permeability. Besides, the term "metamaterial" has also been used by some authors to describe other periodic structures such as electromagnetic bandgap (EBG) structures or photonic crystals, when the period is much smaller in physical size than the wavelength of the impinging electromagnetic wave. The electromagnetic response of such structures is dominated by Bragg-type scattering and involves higher order spatial harmonics (Bloch-Floquet modes) [6]. In this thesis, we focus on such a kind of metamaterial, the so-called "high impedance surface" (HIS).

1.2 High Impedance Surfaces

Background

Electrically conductive surfaces are usually used to act as ground planes for antenna, aiming at gaining a significant front-to-back radiation ratio. The conducting ground plane can redirect part of the radiation into the opposite direction and partially shield the electromagnetic propagation on the other side of the ground plane. However, if an antenna is placed parallel to

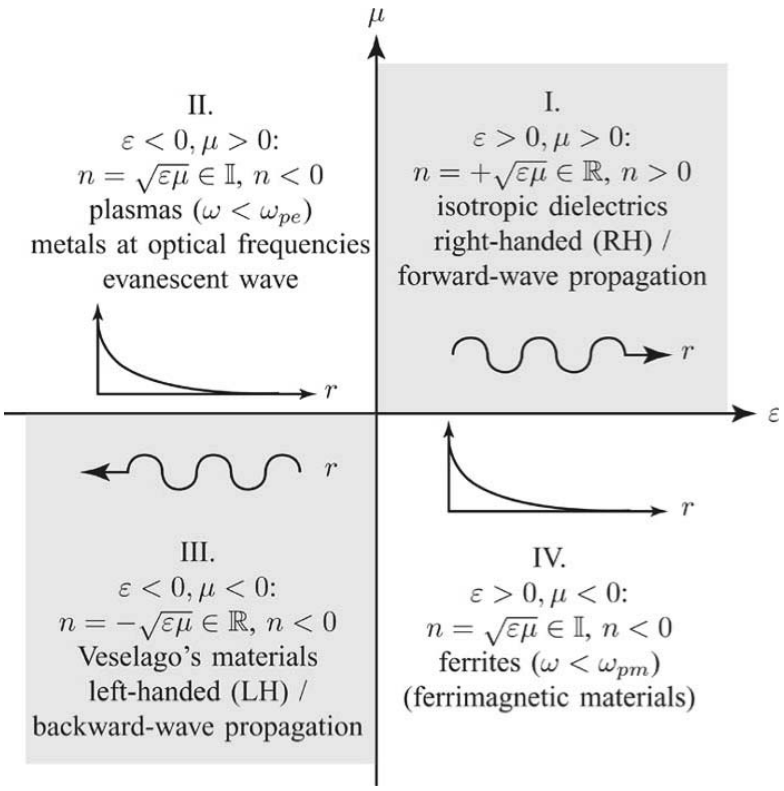

Figure 1.3: Permittivity, permeability and refractive index diagram.

the ground plane in close proximity, the radiated field coming from the antenna current will be cancelled by the radiated field from the image of the antenna current and hence the working efficiency of the antenna will be greatly reduced.

Usually, a quarter wavelength space is included between the antenna and the metal ground plane. This distance can create a 90° phase shift in transmitting wave and a round trip of such distance results in a 180° phase shift, which can compensate the opposite phase influence caused by the ground plane. As illustrated in Fig. 1.4, wave 2 emitted from the antenna to the ground plane surface and reflected to the antenna is in phase with wave 1, which is directly emitted by the antenna on the other side.

One disadvantage of such an antenna system is its huge dimension, since it needs to be around one quarter working wavelength; another disadvantage is the fact that it supports the propagation of surface waves.

A "surface wave" is a wave that travels along the interface between two different media. It is also called "surface plasmon" in optics [21]. In microwaves or radio communication, this wave can be described by surface current. An infinite perfect electric conductor does not support any surface wave. In reality, the conducting ground plane is not an ideally perfect conductor and

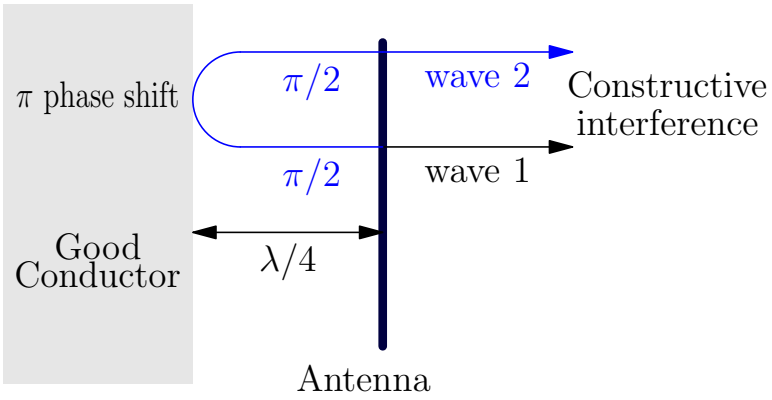

Figure 1.4: Antenna with metallic ground plane

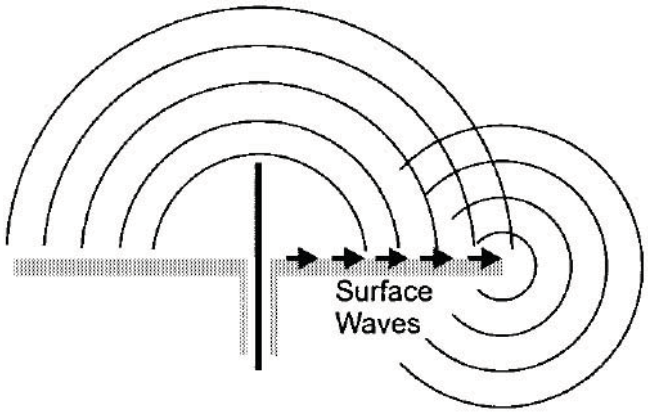

Figure 1.5: An antenna with a traditional ground plane, which supports surface waves

has finite size, so surface currents will be induced and will propagate until they reach an edge or a corner, which will bring about ripples and influence the radiation patterns (as seen in Fig. 1.5). Moreover, if multiple antennas share the same ground plane, surface currents can cause unwanted mutual coupling among them.

A "high impedance surface" is an artificial material/structure formed by periodic metallic arrays printed on a metal-backed substrate [22], which exhibits extremely high impedance ($Z_{HIS} \gg Z_{free\,space}$) in one or several frequency ranges. This man-made material can play the same role as a conducting ground plane in the antenna system, while simultaneously avoiding the propagation of the surface waves and reducing the thickness of the whole system.

The study of such artificial surfaces dates back from the early 1950s [23, 24]. At first, research in America purported to minimize the visibility of aircraft by radar systems. In order to absorb the electromagnetic radiation, some structures, involving arrays of conducting metal (which acted like resistive, capacitive or inductive circuit components), were designed. Before

the existence of HIS structures, corrugated surfaces have been intensively studied in a variety of forms. P. S. Kildal [25] identified a one-dimensional corrugated sheet as a soft surface, by analogy with acoustic boundary conditions. S. Lee and W. Jones [26] analyzed a two-dimensional corrugated surface resembling a lattice of rectangular metal pipes, and derived the surface wave dispersion relation for such a structure. The drawback of such structures is that they are heavy and not easy to fabricate.

In 1978, E. Yablonovitch published a pioneering work on photonic crystals [27]. He found that the spontaneous emission by atoms can be inhibited in a microwave cavity by an electron-hole radiative recombination. Furthermore, he also suggested that a three-dimensional spatial periodic structure can result in a forbidden gap in the electromagnetic spectrum, just as the electronic spectrum has a band gap in crystals. Inspired by this idea, a nearly flat conductor covered with a two-dimensional lattice of small bumps is evolved from a flat sheet [28, 29].

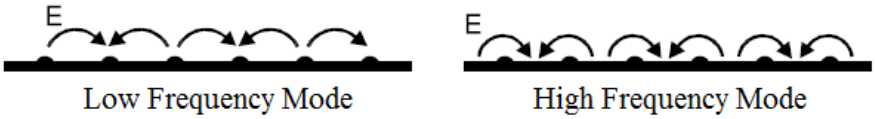

Figure 1.6: A bumpy metal sheet with a narrow surface wave band gap

When the wavelength is much longer than the period of the two-dimensional lattice, the surface waves hardly notice the small bumps. But when the wavelength is comparable to the period, the effects of the surface texture cannot be neglected. When one-half wavelength fits the distance between the two adjacent rows of bumps, this corresponds to the case with a Brillouin zone boundary [30] on a two-dimensional lattice. At this wavelength, a standing wave on the surface may have two possible positions: with the wave crests centered on the bumps, or with the nulls centered on the bumps, as shown in Fig. 1.6. These two modes have slightly different frequencies, separated by a small band gap within which surface waves cannot propagate.

Small bumps only provide a narrow bandwidth because they contribute only a small perturbation to the flat metal surface. If the bumps are enlarged, the bandwidth of the gaps will increase. When the bumps were stretched toward each other, like mushrooms or thumbtacks standing up on the surface, the electric field would be localized to the narrow separation between them, and the first "High Impedance Surface" structure was born. This structure was proposed by D. Sievenpiper in 1999 [22], its properties are similar to those of the corrugated slab, but it is low-cost and easily fabricated.

Generally, HIS is composed of metal plates arranged in a two-dimensional periodic structure backed with a continuous metal sheet. These planar metal plates may connect to the continuous

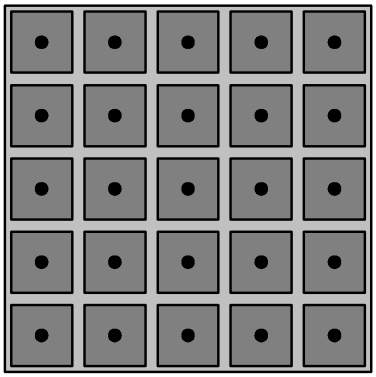

Figure 1.7: Geometry of a mushroom HIS structure (top view)

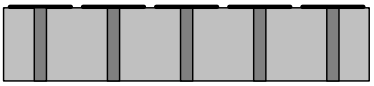

Figure 1.8: Geometry of a mushroom HIS structure (cross view)

lower conductor by vertical posts. For instance, Fig. 1.7 and Fig. 1.8 depicts a top and a cross view of one kind of HIS structure. The square metal patches are raised above the surface, and the dots in the center are vertical connecting posts.

Performance

HIS structures can be viewed as a printed two-dimensional array of resonant elements on a metallic ground plane separated by a dielectric substrate layer. The properties of the whole structure can be explained using an equivalent LC resonant model (shown in Fig. 1.9), where the proximity of the neighboring metal elements provides the capacitance, and the long conducting path between the metal surface and the ground plane provides the inductance.

Figure 1.9: LC equivalent circuit

Around the LC resonance, the HIS structures can effectively prevent the propagation of surface waves and reflect external electromagnetic waves without the phase reversal that occurs on a traditional conductor. As a result, the antenna can radiate without deterioration of its performance as well as retain an in-phase reflection while reducing the overall thickness of the radiating element. Figure 1.10 depicts a dipole antenna lying against a HIS ground plane, which exhibits the merits of using HIS structures.

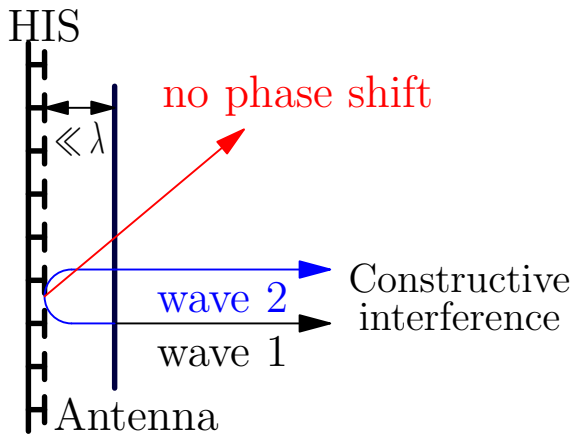

Figure 1.10: Antena with HIS plane

In the frequency range where the surface impedance is extremely high and the tangential magnetic field on the surface is almost null, such a structure can be called a "perfect magnetic conductor". If a simple dipole is located adjacent to a ground plane made of a perfect magnetic conductor, then the direction of image currents will result in a constructive interference rather than a destructive interference. Theoretically, the PMC plane is an ideal material for antenna ground planes.

In [31], the PEC, PMC and HIS/EBG surfaces are each used as the ground plane for the design of low profile antenna. The authors compared the return loss of a dipole antenna over these three ground planes by a numerical simulation. Their results are presented in Fig. 1.11.

As mentioned before, the PEC ground plane can cause a reversed image current which impedes the efficiency of the dipole's radiation, leading to a poor return loss. For the PMC ground plane, although the reflection on the plane is in phase, a strong mutual coupling occurs between the image current and the dipole, due to their close proximity. Thus, the antenna cannot directly match well to a normal 50 ohm transmission line. Under this circumstance, a good return loss can be acquired by using an appropriate impedance transformer, but the design technique is certainly complicated.

Among these three cases, the best return loss is achieved by the case with a HIS ground plane. Over a certain frequency range, the HIS structure behaves like a perfect magnetic conductor with a good impedance match to a normal input. That's why the high impedance structures are also known as "Artificial Magnetic Conductors (AMC)".

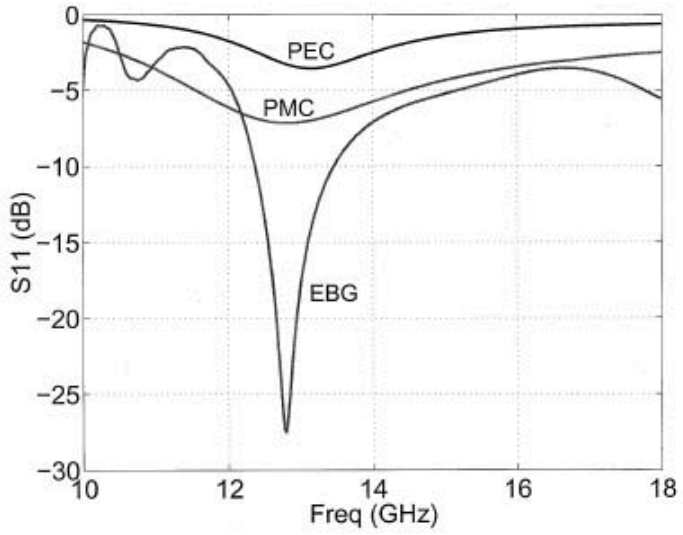

Figure 1.11: FDTD simulated return loss results of a dipole antenna over the PEC, PMC and EBG ground planes

Parameters

HIS structures exhibit a high impedance value around the resonance, so their surface impedance is an appropriate parameter to show their feature. The surface impedance of HIS structures can be obtained analytically or numerically, as will be detailed in later chapters. Here, we give out a general definition for the surface impedance of HIS structures using the equivalent circuit presented in Fig. 1.9. Since the equivalent circuit is a parallel combination of L and C components, the surface impedance can be formulated as:

$$Z_{HIS} = \frac{j\omega L}{1 - \omega^2 LC}, \tag{1.1}$$

where L and C are respectively the effective inductance and the effective capacitance of the HIS structure.

Fig. 1.12 displays the general behavior of the surface impedance in terms of the operating frequency for a given HIS structure. Only the first main resonance of the structure is presented (other resonances appear at higher frequencies). It may be observed that, as compared with the impedance of free space, the surface impedance is extremely high in a narrow region near the resonance. Below the resonance, the surface impedance shows an inductive behavior, which supports the propagation of TE waves; above the resonance, it shows a capacitive behavior, which supports the propagation of TM waves.

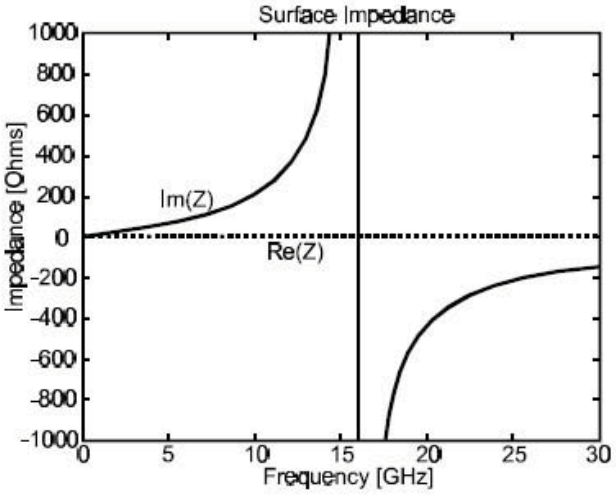

Figure 1.12: An example of the surface impedance curve for a mushroom HIS structure

The resonant frequency of HIS structures can be read from the surface impedance curve, and it serves to engineer the structure's dimensions in the design phase. However, a problem arises: the surface impedance cannot be directly measured in experiments. Therefore, we choose an alternative observation parameter: the reflection coefficient, which will be frequently discussed in future investigation.

The reflection coefficient can be determined for an arbitrary impedance surface by considering the standing wave formed by a forward running wave impinging on the HIS surface and a backward running wave reflected from it. It can also be obtained by considering a transmission line model, as shown in Fig. 1.13, and calculated from the following equations:

$$\Gamma = \frac{Z_L - Z_P}{Z_L + Z_P}, \tag{1.2}$$

where Z_P is the same as the intrinsic impedance of free space ($Z_0 = 377$ ohm) and Z_L is the input impedance seen at a distance from the top surface of HIS structures:

$$Z_L = Z_0 \times \left(\frac{Z_s + Z_0 j \tan(\beta d)}{Z_0 + Z_s j \tan(\beta d)} \right), \tag{1.3}$$

where Z_s is the surface impedance of the HIS structure, d the distance between the excitation port and the surface of the HIS structure and β the propagation constant in free space.

If the incident wave vector is perpendicular to the HIS surface and the observation surface is located on the HIS top surface, then the coefficient of reflection of equation 1.2 can be simplified

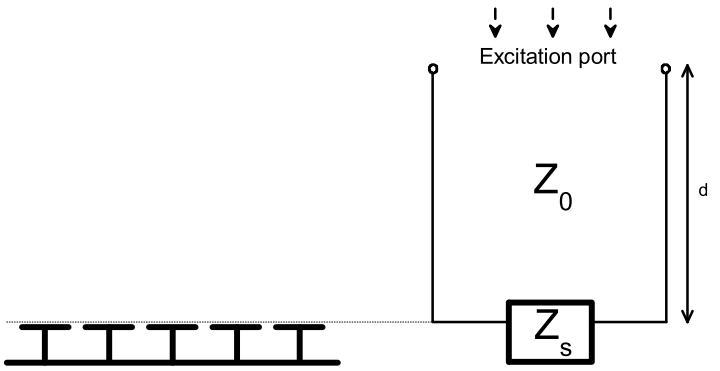

Figure 1.13: Model for calculating the reflection phase

as:

$$\Gamma_{HIS} = \frac{Z_s - Z_0}{Z_s + Z_0}. \tag{1.4}$$

The phase θ_{HIS} can be formulated as

$$\theta_{HIS} = \tan^{-1}\left(\frac{Z_s - Z_0}{Z_s + Z_0}\right). \tag{1.5}$$

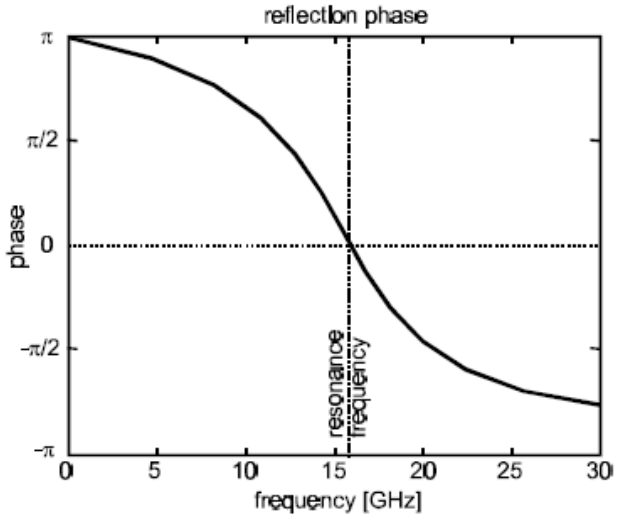

Figure 1.14: An example of the reflection coefficient phase curve for a mushroom HIS structure

Figure 1.14 displays a phase curve for a mushroom HIS structure. Around the resonance, it happens that Z_s is much larger than Z_0 so that the value of Z_0 can be neglected. This means that the wave reflected by the HIS structures, in comparison with the incident wave, may have $\Gamma_{HIS} \approx 1$ and $\theta_{HIS} \approx 0°$ in a certain range.

A structure with a zero-degree reflection phase is an ideal candidate for the ground plane of antenna. However, when the reflection phase is lower than 90°, the antenna can still work efficiently. Generally, the useful bandwidth for a HIS structure is defined as from +90° to −90°. Nevertheless, when identifying the effective frequency band from a reflection phase curve, each application of HIS structures should be individually dealt with. For instance, in [31], it was revealed that the frequency region where the HIS surface has a reflection phase in the range $90° \pm 45°$ is very close to the input-match frequency band. This is not the frequency region where the HIS structure behaves like a PMC surface, but it is a good interval allowing a low profile wire antenna to reach a good return loss.

If the incident wave vector is oblique, the influence of the incidence angle should be taken into account. Moreover, two different polarizations: the TE-incidence and the TM-incidence should be considered. In general, in the case of the TE-incidence, the resonant frequency deviation of HIS structures, $\Delta f/f0$, is relatively small. For the TM-case, the deviation is small only when the incidence angle is close to 0°. For some types of HIS structures, the variation of the incidence angle may cause a dramatic shift on the resonant frequency, which will lead to a very narrow bandwidth in full-wave simulations.

Geometry Configurations

In this section, we introduce various geometry configurations for HIS structures used in the literature, which may offer the readers some helpful ideas in future design.

The periodic square mushroom-like structure can be considered as the classical HIS structures, which has been first and widely studied. This is mainly because of its simplicity, flexibility and a relatively wider bandwidth [32] compared with other simple geometries. As mentioned, the operating mechanism of HIS structures can be explained by an equivalent LC network. The resonance of the structure can be regulated by modifying the effective capacitance and the effective inductance, which depend on geometry parameters. In order to get a lower resonance, a HIS structure with hexagonal patches on the top is proposed in [22], as seen in Fig. 1.15. For the same purpose, more structures, such as fork-like HIS structures and F-like HIS structures (as seen in Fig. 1.16) [36] have been studied.

For a mushroom structure, a lower resonance can be acquired by the configuration of large patches with extremely tiny space between neighboring patches. This is because a long, thin space between the neighboring patches yields a higher capacitance than the short, wide space. However, this kind of HIS structures are not in a good immunity to the variation of the incidence angle. Since the top surface of this structure is almost covered with metal material, the incident

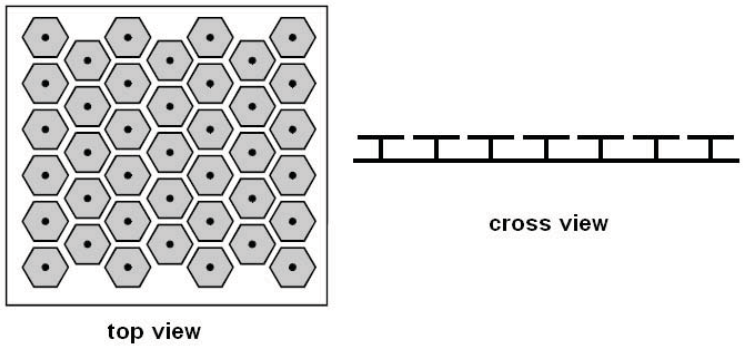

Figure 1.15: Geometry of a hexagonal mushroom-like structure

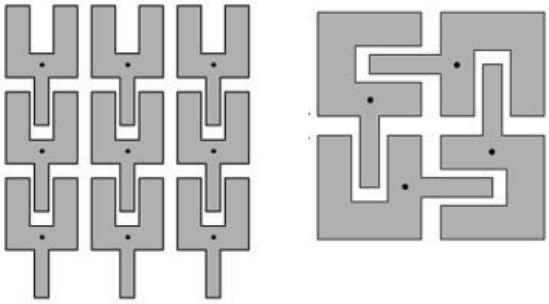

Figure 1.16: Top view of fork-like (left) and F-like structures (right)

wave cannot easily penetrate into the substrate through the slim slots on the top. Hence, a small variation of the angle may cause a big shift in the results.

In order to get a more stable resonance with respect to the incidence angle, self-resonant grid structures have been proposed as substitues for the grid of square patches and thin metal strips, such as "meander-line based high impedance surface" [33]. Several types of self-resonant grid structures are exhibited in Fig. 1.17. Structures of this kind are less metallized on the top surface and appear to be more "transparent" to incidence wave, in comparison with the mushroom structures.

Like the meander line, the Hilbert curve is also a self-resonant grid structure. This curve was imagined by Hilbert in 1891 and is a member of the family of what is known in the mathematics literature as "space-filling curves" [34]. The Hilbert curve has some attractive properties. For instance, the structure of this shape can be made of an electrically long metallic wire compacted within a very small footprint. In [35], this structure is well studied as a compact planar surface for HIS structures. It is proved that the resonance of the Hilbert curve HIS structures is primarily related to the order N of the Hilbert curve. It is also known that the resonance and

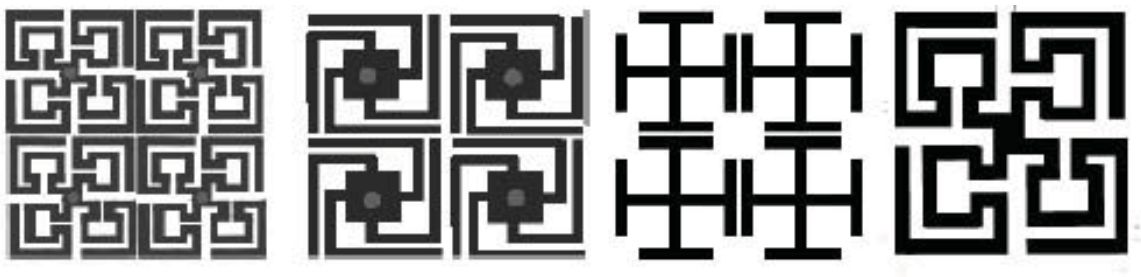

Figure 1.17: Top view of several self resonant grid structures

the bandwidth of this structure are more affected by the height of the surface above the ground rather than the distance between adjacent elements within the array. A family of Hilbert curve HIS structures with order from $N = 1$ to $N = 4$ is presented in Fig. 1.18.

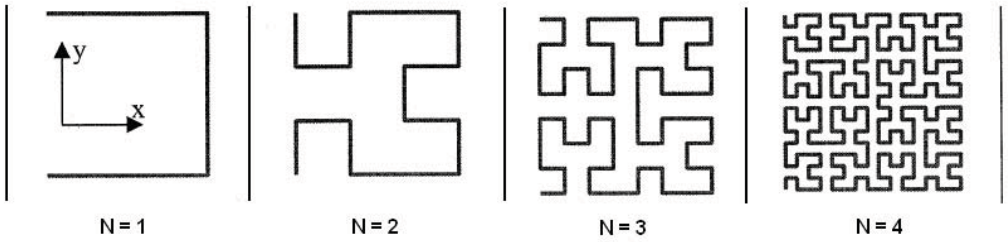

Figure 1.18: Top view of Hilbert curves with various iteration order N

Not only analytical methods and empirical experiences are used in searching for an appropriate HIS geometry configurations. Some numerical algorithms are applied as well. In order to get the most suitable configuration. For instance, a genetic algorithm synthesis methodology was introduced in [37] to evolve optimal multiband fractal HIS structures (Fig. 1.19).

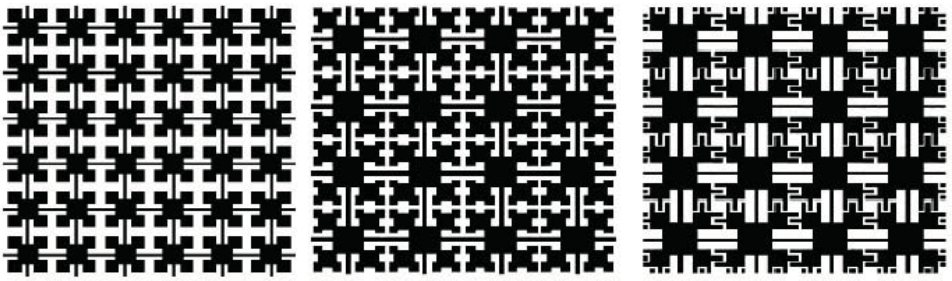

Figure 1.19: Top view of fractal HIS structures

While some efforts are made in designing the top planar surface configuration for HIS structures, the design of vias has also been explored. In [38], the author suggested an array of

densely packed metallic wires properly distributed in a periodic lattice and embedded in a low epsilon dielectric, as shown in Fig. 1.20. This design offers a more compact textured HIS surface and helps making the equivalent surface impedance independent of the angle of incidence. The disadvantage of this structure is that there does not exist a significant electromagnetic band gap for surface waves. It may not be particularly appealing for printed antenna applications, whereas it has the potential of confining or guiding energy with mode sizes below the diffraction limit.

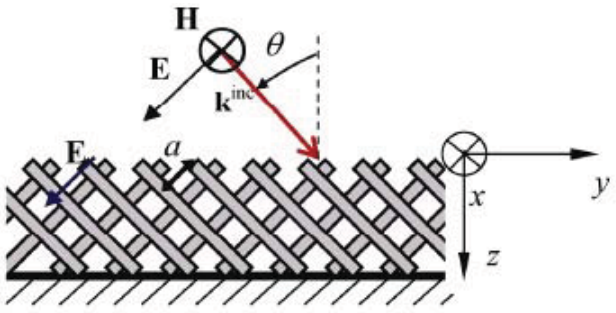

Figure 1.20: Cross view of a HIS structure with densely patched metallic wires

In [39], a mushroom-based structure with slanted vias has been studied. It showed that a further size reduction can be achieved by using slanted vias for a given frequency than with vertical vias. Meanwhile, this structure offers a dual operational frequency band instead of the single band, obtained forthe structures with vertical vias.

In addition, the configuration with vias in different sizes in the same substrate has also been examined in [40], the geometry of which is shown in Fig. 1.21. It is found that this non-homogeneous HIS structure may offer a wider stop band and enhance the performance of restraining surface waves, in comparison with ordinary homogeneous HIS structures.

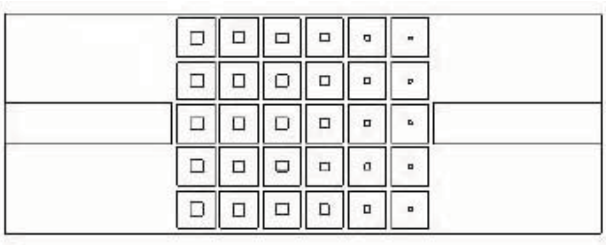

Figure 1.21: Top view of a HIS structure with vias of different sizes

Relatively speaking, the geometry modifications on the top planar surface of the HIS structures weigh more than the changes on the vias. Nevertheless, a subtle change is sometimes very

useful in the optimization of design.

Another helpful technique in geometry configuration is the multi-layer design, one example is seen in [41]. The problem is that more layers may improve some parameters, but at the price of which a thicker structure. Hence, the overall height of the system should be fully considered before using this technique.

Applications

It is known that HIS structures can restrain the propagation of surface currents, while simultaneously behaving as magnetic walls near their resonances. Because of these two noteworthy characteristics, HIS structures are accordingly applied in all kinds of antennas, such as GPS antennas in telecommunication systems [42], in aeronautics [43], and so on. Especially, they have been highly used as ground planes in designing low-profile antennas [44, 45, 46]. Recently, the authors of [48] proposed that the HIS structure itself can perform as an antenna.

In addition, in Electromagnetic Compatibility (EMC), they may serve to suppress the switching noise [49, 50], reduce the mutual coupling between adjacent elements [51], or improve the specific absorption rate for wireless antenna [52].

Apart from the above applications, their potentials have also been discovered for absorbers [53], resonant cavities [54], waveguides and other devices.

1.3 Finite Element Method

In this section, we first review the fundamental theory of electromagnetism in a concise fashion. Then, the FEM is briefly introduced with emphasis on the subjects directly applicable to our work.

1.3.1 Fundamental Electromagnetic Theory

Maxwell's Equations

The classical macroscopic electromagnetic field is described by four vector functions of position and time, denoted as E, B, H, D. The fundamental field vectors E and H are called the electric and magnetic field strengths respectively (we shall refer to them as the electric field and the magnetic field). The vector functions D, B which later will be eliminated from the description of the electromagnetic field via suitable constitutive relations, are called the displacement current and magnetic induction, respectively [55].

In modern notation due to Heinrich Hertz and Oliver Heaviside, Maxwell's equations are written as the following set of partial differential equations [56, 57]:

$$\nabla \times E = -\frac{\partial B}{\partial t}, \tag{1.6}$$

$$\nabla \times H = J + \frac{\partial D}{\partial t}, \tag{1.7}$$

$$\nabla \cdot D = \rho, \tag{1.8}$$

$$\nabla \cdot B = 0. \tag{1.9}$$

Equation 1.6 is based on Faraday's experiment (1825) and gives the effect of a changing magnetic field on the electric field. Equation 1.7 is Ampère's law which is based on Biot-Savart experiment (1826) and Maxwell's great contribution — displacement current (1861). Equations 1.8 and 1.9 are Gauss's laws accounting for Coulomb's type experiments (1785). The former gives the effect of the charge density on the electric displacement and the latter expresses the fact that the magnetic induction B is solenoidal. In terms of electric and magnetic fields, the above four field equations are the complete Maxwell's equations [58].

The empirical law of the conservation of electric charge

$$\nabla \cdot J = -\frac{\partial}{\partial t}\rho \tag{1.10}$$

may be obtained by taking divergence of Eq. 1.7 and substituting Eq. 1.8 into it. This law governs the electric current density J and the electric charge density ρ. Here, J is regarded as the sum of the induced current density J_i and the exciting current density J_e,

$$J = J_i + J_e. \tag{1.11}$$

Constitutive Relations

In order to uniquely determine fields in particular cases, the Maxwell equations should be completed with constitutive equations [59]. The constitutive relations reflect medium polarizations that are related to the case under study, which is an important topic in solid-state physics [60]. Once the responses of bound currents and charges are related to the fields, Maxwell's equations can be fully formulated in terms of the E- and H-fields alone, with only the free charges and currents appearing explicitly in the equations.

The constitutive relations are usually written as:

$$D = \varepsilon E, \tag{1.12}$$

$$B = \mu H, \tag{1.13}$$

$$J_s = \sigma E. \tag{1.14}$$

where ε is the electric permittivity, μ the magnetic permeability and σ the electric conductivity. They are independent of Maxwell's equations. In general, ε and μ are not simple constants, but rather tensors. However, in our work, we consider only the linear and isotropic materials, characterized by the scalar triplet: ε, μ and σ.

In free space, void of any matter, it is known that

$$\mu = \mu_0 = 4\pi \times 10^{-7}\ H/m, \tag{1.15}$$

$$\varepsilon = \varepsilon_0 \backsimeq 8.85 \times 10^{-12}\ F/m. \tag{1.16}$$

The materials with $\sigma = 0$ are considered to be dielectric lossless.

Electromagnetic Wave Equation

According to Maxwell's equations, an oscillating electric field generates an oscillating magnetic field, the magnetic field in turn generates an oscillating electric field, and so on. These oscillating fields together form an electromagnetic wave.

The wave equation can easily be derived by taking the curl of Eq. 1.6 and substituting Eq. 1.7 with the help of the constitutive relation:

$$\nabla \times \frac{1}{\mu}\nabla \times E + \varepsilon\frac{\partial^2 E}{\partial t^2} + \frac{\partial J}{\partial t} = 0. \tag{1.17}$$

We find by using the vector identity $\nabla \times (\nabla \times E) = \nabla(\nabla \cdot E) - \nabla^2 E$ and Eq. 1.8, that Eq. 1.17 can be written as:

$$\nabla^2 E - \mu\varepsilon\frac{\partial^2 E}{\partial t^2} = \mu\frac{\partial J}{\partial t} + \nabla(\frac{\rho}{\varepsilon}). \tag{1.18}$$

Equation 1.18 is the wave equation for a homogeneous medium. The wave equation can also be expressed by eliminating E, rather than H.

In the case of free space, there are no charges or currents, so the E-based wave equation can

be simplified as:

$$\nabla^2 E - \mu\varepsilon\frac{\partial^2 E}{\partial t^2} = 0 \tag{1.19}$$

with the dispersion relation $k^2 = \omega^2\mu\varepsilon$.

In the case of a lossy medium, the conduction current cannot be neglected and the permittivity is no more a real constant value but a complex value, defined as:

$$\varepsilon_\sigma = \varepsilon - j\frac{\sigma}{\omega}. \tag{1.20}$$

The permittivity doesn't vary a lot at low frequency, but may vary a lot more at high frequencies. In our simulation, we assume that the permittivity is always constant within a certain frequency band.

Interface Between Two General Media

The Maxwell equations are not a complete classical description of the electromagnetic field inside the solution region, they should be supplemented with boundary conditions and initial conditions when solving a practical problem.

For a stationary interface separating regions 1 and 2, we let the surface normal n point from region 2 to region 1, as shown in Fig. 1.22.

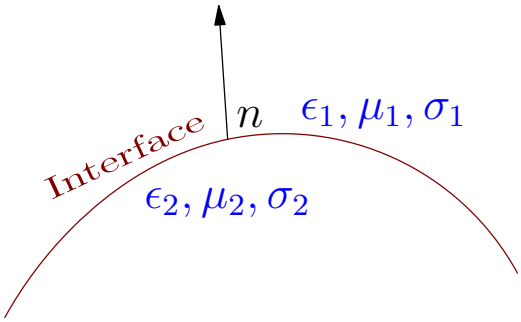

Figure 1.22: Interface between two different media

The boundary conditions between two general media can be derived from the Maxwell equations as follows:

$$n \times (E_1 - E_2) = 0, \tag{1.21}$$

$$n \times (H_1 - H_2) = J_{es}, \tag{1.22}$$

$$n \cdot (D_1 - D_2) = \rho_{es}, \tag{1.23}$$

$$n \cdot (B_1 - B_2) = 0, \tag{1.24}$$

where subscripts 1 and 2 denote fields in regions 1 and 2, respectively. Essentially, the boundary conditions state that the tangential components of E and the normal components of B are continuous across the boundary; the discontinuity of the tangential components of H is equal to the surface current density J_{es} (if J_{es} is imposed there) and the discontinuity of the normal components of D is equal to the surface charge density ρ_{es} (if ρ_{es} is imposed there) [57].

Perfect Electric Conductor

The perfect electric conductor (PEC) is an idealization of a good conductor such as some highly conducting metal or dielectric of very high permittivity [61]. From Ohm's law (Eq. 1.14), we see that if the conductivity σ is infinite and if the current density is to remain bounded, then the E-fields inside this medium vanish. If region 2 in Fig. 1.22 represents a perfect electric conductor, then the necessary and sufficient boundary conditions at the interface between region 1 and region 2 are:

$$n \times E = 0, \tag{1.25}$$

$$n \cdot B = 0. \tag{1.26}$$

while there is no condition on the other two vectors H and D.

Perfect Magnetic Conductor

The perfect magnetic conductor (PMC) is a medium which has no simple physical counterpart. If region 2 in Fig. 1.22 represents a perfect magnetic conductor, at the surface of a PMC body, the boundary conditions are:

$$n \times H = 0, \tag{1.27}$$

$$n \cdot D = 0. \tag{1.28}$$

while there is no directly imposed condition on the other two vectors B and E.

Impedance Boundary Condition

If the material on one side of the boundary is not a perfect conductor, but allows the field to penetrate only a small distance, a more appropriate boundary condition is the impedance or

imperfectly conducting boundary condition. Suppose again that the good conductor is in region 2 and that the normal n points from region 2 into region 1, this boundary condition becomes:

$$n \times H_2 - \lambda(n \times E_2) \times n = 0, \tag{1.29}$$

where the impedance λ is a function of position on the surface of the material.

1.3.2 FEM Theory

The evolution of the Finite Element Method (FEM) [62] has intimately been linked to developments in engineering and computer sciences. The FEM is a good choice for solving problems with complicated domains and it is applied not only in aeronautics, transportation industries, nuclear, but in electromagnetic domain as well.

The FEM is a numerical technique appropriate for a partial differential equation and a set of boundary conditions. The main idea behind the method is the representation of the domain with smaller subdomains called "elements". The distribution of the primary unknown quantity inside an element is interpolated based on, most often, the values at the nodes.

In our work, however, we have to deal with vector-valued elements, hence the unknown quantities are localized at edges. The study domain associated with our problem, here described in a 3D cubic box, is subdivided into N tetrahedral elements, as seen in Fig. 1.23. These elements, constituted the finite element mesh, do not have to be of the same dimensions. Each element has six edges and each edge has two nodes, as seen in Fig. 1.24. An element is allowed to have arbitrary length to provide the ability to generate a denser mesh near regions where the solution is expected to have rapid spatial variations. In addition, the discretization of the domain gives generality and versatility to specify material properties and sources.

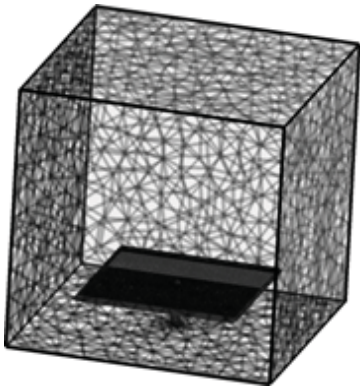

Figure 1.23: A study domain meshed with tetrahedral elements

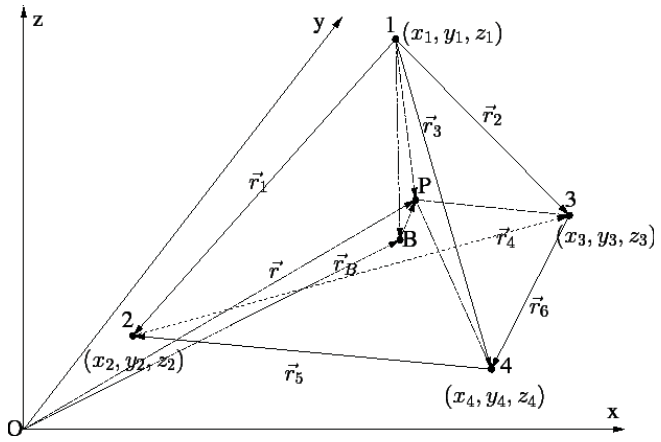

Figure 1.24: Tetrahedral element

The numerical solution yields the values of the primary unknown quantity at the edges of the discretized domain. This solution is obtained by solving a system of linear equations. To form such a linear system of equations, the governing differential equation and associated boundary conditions must first be converted to a weak formulation either by minimizing a functional or using a weighted residual method.

Weak formulations, sometimes referred as variational formulations, are an important tool for the analysis of mathematical equations that permit the transfer of concepts of linear algebra to solve problems in other fields such as partial differential equations. Weak formulations allow us to get the approximation of the solutions easier. The weak formulation can be obtained by multiplying the partial differential equation by an arbitrary test function of (in most cases) the spatial variables, then integrating the result over the domain. One then requires that the result is zero for all choices of such functions. Note that any numerical scheme for approximating Maxwell's equations in the presence of material discontinuities must take into account that tangential components of the field are continuous, while allowing normal components to jump across a material boundary [55].

In our work, we may use the electromagnetic wave equation (1.17) to formulate our real problem. Suppose a domain D, enclosed by the boundary $S = dD$, we must find a field E belonging to the functional space:

$$\mathbb{E} = \mathrm{L}^2_{\mathrm{rot}} = \{E : \ E \in \mathrm{L}^2(D), \ \nabla \times E \in \mathrm{L}^2(D)\}, \tag{1.30}$$

satisfying

$$\nabla \times (\frac{1}{\mu} \nabla \times E) + \varepsilon \cdot \frac{\partial^2 E}{\partial t^2} = -\frac{\partial J}{\partial t}. \tag{1.31}$$

Let us develop the weak formulation corresponding to our real problem by multiplying Eq. 1.31 with a test function v.

$$\int_D \left[\nabla \times (\frac{1}{\mu}\nabla \times E) \cdot v + \varepsilon \frac{\partial^2 E}{\partial t^2} \cdot v\right] = -\int_D \frac{\partial (J_e + J_i)}{\partial t} \cdot v \; \forall v \in \mathbb{E}. \tag{1.32}$$

After applying the first Green identity and Eq. 1.11, the weak formulation can be rewritten as:

$$\int_D \left[\frac{1}{\mu}(\nabla \times E) \cdot (\nabla \times v) + \sigma \frac{\partial E}{\partial t} \cdot v + \varepsilon \frac{\partial^2 E}{\partial t^2} \cdot v\right] + \int_S (n \times \nabla \times E) \cdot v = -\int_D \frac{\partial J_e}{\partial t} \cdot v \forall v \in \mathbb{E} \tag{1.33}$$

where n is the outward normal vector on the boundary S of D.

The approximate solution of the problem over the discretized domain is represented inside an element by a set of interpolation functions also known as shape functions. In our study domain, the approximate E-field vector can be expressed in terms of the values associated with the edges of the elements:

$$E = \sum_{i=1}^{N} e_i W_i, \tag{1.34}$$

where N is the number of edges of the mesh, W_i is the function associated with the edge i and e_i represents the E-field circulation along the edge i: $e_i = \int_{edge\, i} E \cdot dl$. These circulations are the unknowns, called "degrees of freedom" (DOF).

The accuracy of the solution depends, among other factors, on the order of the polynomials of interpolation function, which may be linear, quadratic, or higher order. In our case, we deal with the vector fields in electromagnetism and Whitney forms are chosen as interpolants.

Refer to the tetrahedron from Fig. 1.24. The oriented edge i has two nodes: a and b. The Whitney function [66] is expressed by:

$$W_i = \lambda_a \nabla \lambda_b - \lambda_b \nabla \lambda_a, \tag{1.35}$$

where λ_a and λ_b are the barycentric coordinates associated with nodes a and b.

Here, a subscript index is used for the vector basis functions. For instance, for the edge 1, we have W_1. Since λ_1 vanishes on the facet defined by nodes 2, 3, 4 and $\nabla \lambda_1$ is perpendicular to that facet, W_1 has no tangential component on this facet. Analogously it can be stated that W_1 has no tangential component along the edges different from the edge 1 and its normal components is discontinuous. Hence, we have the following relation:

$$\int_{edge\, i} W_j = \begin{cases} 0 & if\ i \neq j \\ 1 & if\ i = j \end{cases} \tag{1.36}$$

The finite element equations are derived by first constructing the weighted residual of the governing differential equation as applied to a single element. Applying Eq. 1.34 into Eq. 1.33, we obtain

$$\int_D \left[\frac{1}{\mu} (\nabla \times \sum_{i=1}^{N} e_i W_i) (\nabla \times v) + \sigma \frac{\partial (\sum_{i=1}^{N} e_i W_i)}{\partial t} \cdot v + \varepsilon \frac{\partial^2 (\sum_{i=1}^{N} e_i W_i)}{\partial t^2} \cdot v \right] =$$

$$- \int_S (n \times \nabla \times \sum_{i=1}^{N} e_i W_i) \cdot v - \int_D \frac{\partial J_e}{\partial t} \cdot v \; \forall v \in \mathbb{E} \tag{1.37}$$

To be able to solve for the unknowns, it is important to have as many independent test functions as unknowns. In our work, we choose the Galerkin method, which is a particular form of the weighted residuals method. Its particular formulation is simple and practical to implement and moreover, normally provides precise and accurate results. With the Galerkin approach, the test functions v coincide with the shape functions W. Replacing v by W_i in Eq. 1.33, we obtain:

$$\sum_{i=1}^{N} e_i \int_D \frac{1}{\mu} (\nabla \times W_i) \cdot (\nabla \times W_j) + \sum_{i=1}^{N} \frac{de_i}{dt} \int_D \sigma W_i \cdot W_j + \sum_{i=1}^{N} \frac{d^2 e_i}{dt^2} \int \varepsilon W_i \cdot W_j =$$

$$- \int_D \frac{\partial J_e}{\partial t} \cdot W_j - \int_S (\cdot) dS. \; (\forall j,\ j = \ 1, \ \ldots, \ N \ ). \tag{1.38}$$

Eq. 1.38 can be written in matrix form:

$$[S]e + [T_1]\frac{de}{dt} + [T_2]\frac{d^2 e}{dt^2} = [f]\,, \tag{1.39}$$

where e is the unknown vector of edge circulation: $e = [\ e_1, \ e_2, \ \cdots, \ e_N\ ]^t$; the f is a combination of all kinds of boundary conditions.

Matrices $[S]$, $[T_1]$and$[T_2]$ are independent of time:

$$[S]_{ij} = \int_\Omega \frac{1}{\mu} (\nabla \times W_i) \cdot (\nabla \times W_j) d\Omega, \tag{1.40}$$

$$[T_1]_{ij} = \int_\Omega \sigma W_i \cdot W_j, \tag{1.41}$$

$$[T_2]_{ij} = \int_\Omega \varepsilon W_i \cdot W_j, \tag{1.42}$$

and $[F]$ is computed by

$$[F]_i = -\int \frac{\partial J_e}{\partial t} \cdot W_i. \tag{1.43}$$

Either by using the Fourier transform in time or because we wish to analyze electromagnetic propagation at a single frequency, the time-dependent problem can be reduced to the time-harmonic Maxwell system. So, equation 1.39 can be written in frequency domain as

$$[S]e + j\omega[T_1]e + (j\omega)^2[T_2]e = [F], \tag{1.44}$$

where $F_i = -j\omega \int J_e \cdot W_i$.

The numerical solution yields the values of the primary unknown quantity at the edges of the discretized domain. The assembly of all elements results in a global matrix system representing the entire domain [64]. The weak formulation results in a system of N linear equations with N unknowns. The resulting matrix system of linear equations is:

$$\begin{bmatrix} K_{11} & K_{12} & K_{13} & \cdots & K_{1N} \\ K_{21} & K_{22} & K_{23} & \cdots & K_{2N} \\ K_{31} & K_{32} & K_{33} & \cdots & K_{3N} \\ \vdots & \vdots & \vdots & \vdots & \vdots \\ K_{N1} & K_{N2} & K_{N3} & \cdots & K_{NN} \end{bmatrix} \begin{bmatrix} e_1 \\ e_2 \\ e_3 \\ \vdots \\ e_N \end{bmatrix} = \begin{bmatrix} F_1 \\ F_2 \\ F_3 \\ \vdots \\ F_N \end{bmatrix}, \tag{1.45}$$

where the matrix $[e]$ corresponds to the unknown quantities of electric circulations along every edge in the finite element mesh, the matrix $[K]$ is the system matrix equal to $[S]+j\omega\,[T_1]-\omega^2\,[T_2]$ and the matrix $[F]$ is the source.

1.3.3 Boundary Conditions in FEM

This subsection outlines the procedure used to impose boundary conditions on the set of linear equations obtained from the weak formulation of the governing differential equation. A non-singular matrix system (except in case of resonance) is obtained after imposing the boundary conditions associated with a given boundary value problem.

Dirichlet Conditions

In the case of Dirichlet conditions, the E-field circulations on some edges are known in advance. Let's index the edges in such a manner that DOF e_i ($i = \ 1, \ \ldots, \ M$, with $M < N$) are the unknowns, while

$$e_i = e_i^g \ (\forall i = \ M+1, \ \ldots, \ N \ ), \tag{1.46}$$

where the e_i^g are the given edge values for all edges on the excited part of the boundary.

Eq. 1.45 can be rewritten as:

$$\sum_{j=1}^{M} K_{ij} e_j + \sum_{j=M+1}^{N} K_{ij} e_j^g = F_i \ (\forall i = \ 1, \ \ldots, \ N \ ). \tag{1.47}$$

Combine Eq. 1.45 with Eq. 1.46, we obtain:

$$\sum_{j=1}^{M} K_{ij} e_j = F_i - \sum_{j=M+1}^{N} K_{ij} e_j^g, \tag{1.48}$$

which is an $M \times M$ linear system.

From Eq. 1.48, it is seen that after imposing the Dirichlet boundary condition on the edges: $M+1, \ \ldots, \ N$, only M unknowns will be left to be determined.

In case $e_i^g = 0$, the Dirichlet boundary condition is precisely called "homogeneous Dirichlet condition". In programming, this case can be easily realized by several linear operations of elimination.

In the case of $e_i^g \neq 0$, the Dirichlet boundary condition is called "non-homogeneous Dirichlet condition". This case may be computed by using a "penalty method" [67]. Suppose the edge n is associated with the "non-homogeneous Dirichlet condition", imposing this condition on edge i can be realised by adding a large value α to the term K_{nn} and replacing F_n with $F_n + \alpha e_i^g$ in 1.45:

$$\begin{bmatrix} K_{11} & \cdots & K_{1i} & \cdots & K_{1N} \\ \vdots & & \vdots & & \vdots \\ K_{n1} & \cdots & K_{nn} + \alpha & \cdots & K_{nN} \\ \vdots & & \vdots & & \vdots \\ K_{N1} & \cdots & K_{Ni} & \cdots & K_{NN} \end{bmatrix} \begin{bmatrix} e_1 \\ \vdots \\ e_i \\ \vdots \\ e_N \end{bmatrix} = \begin{bmatrix} F_1 \\ \vdots \\ F_n + \alpha e_n^g \\ \vdots \\ F_N \end{bmatrix}. \tag{1.49}$$

The equation corresponding to the n-th line is:

$$\left(\sum_{j=1}^{N} K_{nj} e_j\right) + \alpha e_i = F_n + \alpha e_n^g. \tag{1.50}$$

In programming, we choose $\alpha = 10^7 \cdot \max(K_{ij})$. If the matrix $[K]$ is ill-conditioned or some components of $[e]$ are extremely large, this method will be less effective.

Neumann Boundary Condition

The Neumann boundary condition, also called "natural boundary condition", is a special case of mixed boundary condition. When the primary unknown is the electric field, as here, Neumann conditions correspond to perfect magnetic conducting surfaces

Periodic Boundary Condition

The periodic boundary condition (PBC) is widely employed in simulating arrays of periodically repeated structures, such as three-dimensional lattice structures for crystals, artificial dielectrics consisting of periodically placed conducting pieces, etc. If the solution is itself, as will be the case here, spatially periodic, this can largely simplify the computation of what would be otherwise a large system by working on a single cell.

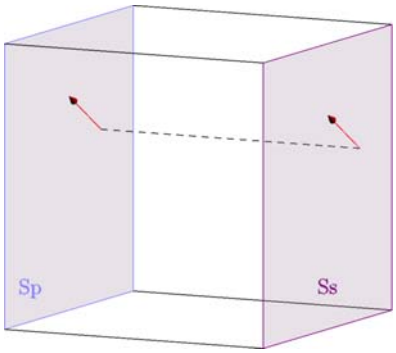

Figure 1.25: A cubic domain with periodic boundary conditions on two opposite faces

We suppose that the study domain is a cubic box, discretized by tetrahedra elements, and that the periodic boundary conditions are assigned to its two opposite surfaces S_p and S_s, which are discretized by edge elements (as seen in Fig. 1.25). If l is an edge of the mesh on the left wall (S_p), its translate k should be an edge of the mesh on the right wall (S_s). To solve an electromagnetic problem by FEM, we calculate the E-field circulations on every edge element.

When applying the PBC on two faces, the E-field circulations on such a couple of edges should be same. Therefore, taking the circulations along edges l and k, we have

$$e_l = e_k, \tag{1.51}$$

Eq.1.51 is enforced by imposing the PBC constraint to one couple of edges. For all the DOFs, it is possible to build a rectangular matrix B expressing all such PBC relations in one stroke as:

$$Be = 0. \tag{1.52}$$

Suppose for a moment that matrix $[K]$ is positive definite. If there were no constraints on e such as those of type (1.51), one would solve the linear system

$$[K][e] = [F], \tag{1.53}$$

which is equivalent to

$$e = \arg\inf\{(Ke', e') - 2(F, e') : \ e' \in \textit{space of all possible vectors}\}, \tag{1.54}$$

where (X, Y) means $\sum X_i Y_i$ and $\arg\inf\{f(x) : \ x \in X\}$ means the value (or the set of values) of variable x in X such that $f(x) <= f(y)$ for all y in X. In presence of the constraints (1.52), we must instead solve

$$e = \arg\inf\{(Ke', e') - 2(F, e') : \ \textit{with } Be' = 0\}. \tag{1.55}$$

Since our problem is associated with the Maxwell equations, which do not correspond to a minimization problem, $[K]$ is not positive-definite, so instead of (1.55), the correct formulation is

$$\underline{E} = \arg\mathrm{stat}\{(Ke', e') - 2(F, e') : \ \textit{with } Be' = 0\}. \tag{1.56}$$

where $\mathrm{stat}\{f(x) : \ x \in X\}$ means the stationary value of the function $f(x)$ for all x in X.

There are two ways to deal with such constrained linear systems:

1) Use Lagrange multipliers λ, which increases the number of unknowns, but gives an unconstrained system formulated as:

$$\begin{bmatrix} K & B^t \\ B & 0 \end{bmatrix} \begin{bmatrix} e' \\ \lambda \end{bmatrix} = \begin{bmatrix} F \\ 0 \end{bmatrix}. \tag{1.57}$$

2) Express the DOF in terms of an independent subset of them, which decreases the number of unknowns, but requires to find matrix C that maps a subvector $\underline{X}'$ of the vector of degrees of freedom e' to a full vector e' of degrees of freedom, and such that (1) the kernel of C reduces to 0, (2) the range of C coincides with the kernel of B. In that case,

$$e' = C\underline{X}' \tag{1.58}$$

will automatically satisfy $Be' = 0$ for all possible values of the vector $\underline{X}'$. Therefore, (1.56) becomes

$$\underline{X}' = \arg\operatorname{stat}\{(KC\underline{X}', C\underline{X}') - 2(F, C\underline{X}')\}. \tag{1.59}$$

A natural choice for $\underline{X}'$ in our case, where (1.52) expresses periodic boundary conditions, is the subvector of DOFs associated with all edges inside the box plus those on the "master" surface S_p. Then C must be built so as to yield appropriate values (satisfying Eq. 1.51) on the "slave" surface S_s. A convenient choice for B and C is then

$$B = [\ \overset{i=1}{0},\ \cdots,\ 0,\ \overset{i=l}{1},\ 0,\ \cdots,\ 0,\ \overset{i=k}{-1},\ 0,\ \cdots,\ \overset{i=N}{0}\ ]. \tag{1.60}$$

With same hypothesis for edge l and edge k, the matrix C can be chosen as:

$$C = \begin{bmatrix} & & & \overset{j=l}{} & & & \overset{j=k}{} & & & \overset{j=N-1}{} \\ & 1 & 0 & \cdots & \cdots & \cdots & \cdots & \cdots & \cdots & 0 \\ & 0 & \ddots & & & & & & & \vdots \\ i=l & \vdots & & 1 & & & & & & \vdots \\ & \vdots & & & \ddots & & & & & \vdots \\ & \vdots & & & & 1 & & & & \vdots \\ i=k & \vdots & & 1 & & & 0 & & & \vdots \\ & \vdots & & & & & & 1 & & \vdots \\ & \vdots & & & & & & & \ddots & 0 \\ i=N & 0 & \cdots & \cdots & \cdots & \cdots & \cdots & \cdots & 0 & 1 \end{bmatrix}_{N\times(N-1)}, \tag{1.61}$$

which is a matrix with diagonal values equal to 1, an exception happens at k-th row, where $C_{kl} = 1$ and $C_{kk} = 0$.

The algorithm that builds the reduced stiffness matrix of the final unconstrained system from the original stiffness matrix of the constrained system in Eq. 1.56 is explained as follows:

1) add l -th line to k-th line in matrix $[K]$, delete the l -th line and move downside lines one position up;

2) add l -th row to k-th row in matrix $[K]$, delete the l -th row and move rightside rows one position left;

3) delete the l -th line term in matrix $[e]$ and move downside terms with one line up;

4) add l -th line term on k-th line term in matrix $[F]$, delete the l -th line term and move downside terms one-line up.

These linear operations can easily be implemented in Matlab.

1.4 Motivation and Organization of the Thesis

In the past decade, the artificial structures called "High Impedance Surface (HIS)" have drawn intensive interest. Such structures have been widely investigated for the improvements of antenna performances, which are featured by numerous parameters such as gain, quality factor, shapes and dimensions. To fulfill the requirements in antenna applications, we need a technique to contrive the appropriate dimensions and geometries of HIS structures. Thus, the objective of this thesis is to model these structures and to characterize their performances in the design of antennas.

The thesis is organized as follows:

In Chapter 1, we give a general knowledge of metamaterials and particularly introduce the background, performances, geometry configurations and applications of HIS structures. We also briefly review the electromagnetic fundamental theory and the finite element method. All the formalizations presented in this part are relevant to our real problem. In addition, the programming techniques relevant to the numerical method are also addressed. This chapter lays the foundation for the numerical modeling of HIS structures in later chapters.

In Chapter 2, we present several analytical modelings for HIS structures, as available in the literature. Concerning the geometry, two most-widely investigated structures (the Mushroom structure and the Jerusalem structure) are considered. Furthermore, several parametric studies are performed to understand the HIS properties from a physical perspective.

In Chapter 3, numerical models are developed to characterize HIS structures, in which dif-

ferent modeling schemes and different boundary condition schemes are investigated. In order to validate these models, we compare the results of surface impedance calculated by analytical methods and numerical simulations with rotationally symmetric HIS structures. Then two new numerical methods are proposed in calculating the 2D surface impedance for general HIS structures, which include both the symmetric structures and the asymmetric structures. These two methods are validated through comparing the analytical, numerical and experimental results. The limitations and the trade-offs of these two methods are also discussed.

In Chapter 4, we concentrate on experimental measurements. Many samples have been fabricated and characterized to fully verify the validity of our numerical methods.

In Chapter 5, we propose an equivalent model, in which all the heterogeneous HIS elements are represented by a homogeneous surface, characterized by its surface impedance. It is demonstrated that by adopting this equivalent model, the computing time and the core memory can be saved to a high extent. Models of this kind could be integrated into emulation packages so as to provide initial insights in the process of the antenna design.

The last chapter develops conclusions and sketches perspectives for future work.

Chapter 2

Analytical Modeling

2.1 Mushroom Structures

2.1.1 Resonant LC Circuit Model by Sievenpiper

The mushroom-like HIS structure (simplified as "mushroom structure" here) is composed of a thin surface with periodic metal patches on the top, a dielectric substrate and a ground plane. Figure 2.1 depicts the geometry of a unit cell of a square mushroom structure, in which a via connects the middle of the patch to the ground plane.

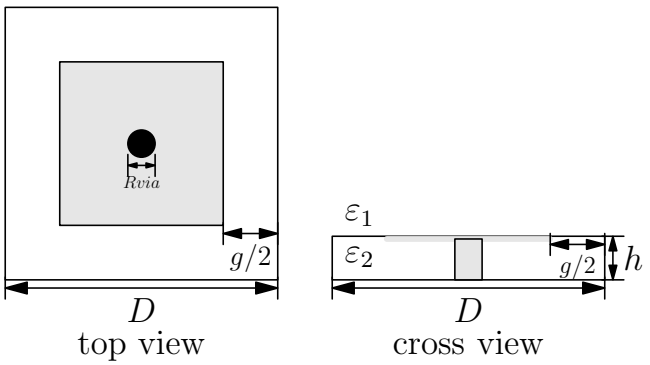

Figure 2.1: Geometry of a unit cell for a mushroom structure

When this HIS structure was first proposed by Sievenpiper, an effective circuit model was used to describe it. When the protrusions of the HIS elements are small in comparison to the wavelength, their electromagnetic properties can be described using lumped circuit elements – capacitors and inductors [22]. As far as the surface impedance is concerned, this structure has an equivalent LC circuit (see Fig. 2.2), represented with impedance:

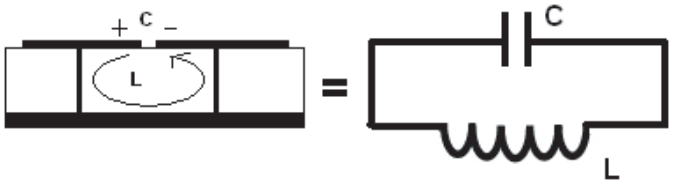

Figure 2.2: Equivalent model of one unit cell for the mushroom structure

$$Z_s(\omega) = \frac{j\omega L}{1 - \omega^2 LC}, \tag{2.1}$$

where the ω is the angular frequency of operation.

With the help of Eq. 2.1, the resonant frequency of the mushroom structure can be defined as:

$$f_{resonant} = \frac{1}{2\pi\sqrt{LC}}. \tag{2.2}$$

The capacitance C comes from the fringing electric field between adjacent metal plates. It can be derived by using the technique of conformal mapping for a pair of semi-infinite plates separated by a gap [22] and expressed as:

$$C = \frac{(D-g)(\varepsilon_1 + \varepsilon_2)}{\pi} \cosh^{-1}\left(\frac{D}{g}\right), \tag{2.3}$$

where D is the spatial period of the array (i.e, the width of the unit cell); g is the distance between the neighboring patches; ε_1 and ε_2 represent the permittivity of media on two sides of the patch, as seen in Fig. 2.1. Usually, ε_1 is the permittivity of free space ($\varepsilon_1 = \varepsilon_0$) and ε_2 is the permittivity of the substrate ($\varepsilon_2 = \varepsilon_0\varepsilon_r$).

The inductance L results from the current flowing around a path through via and the bottom plate. In the case of a square patch, where the length and the width of the patch are same, the inductance only depends on the thickness of the structure h and the permeability of substrate μ:

$$L = \mu h. \tag{2.4}$$

Adopting the LC equivalent model given by Sievenpiper, we perform parametric studies to investigate the relationship between the geometrical dimensions and the surface impedance of

the mushroom structures. The analytical calculations may not only help us to understand the physical mechanism of this kind of structures, but also get some guidelines in designing an antenna system combined with these structures.

Note that in this chapter, we consider only the cases with a non-lossy substrate, so the real part of the surface impedance is always zero and will not be observed here.

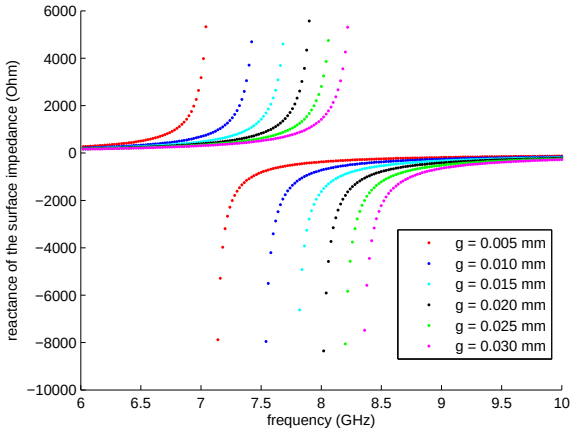

Figure 2.3: Mushroom structures: D = 2.4 mm, h = 1.6 mm, $\varepsilon_r = 4.4$, g varies from 0.005 mm to 0.3 mm.

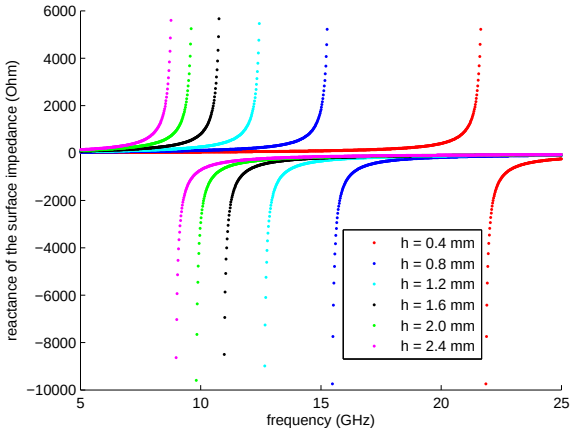

Figure 2.4: Mushroom structures: D = 2.4 mm, g = 0.2 mm, $\varepsilon_r = 4.4$, h varies from 0.4 mm to 2.4 mm.

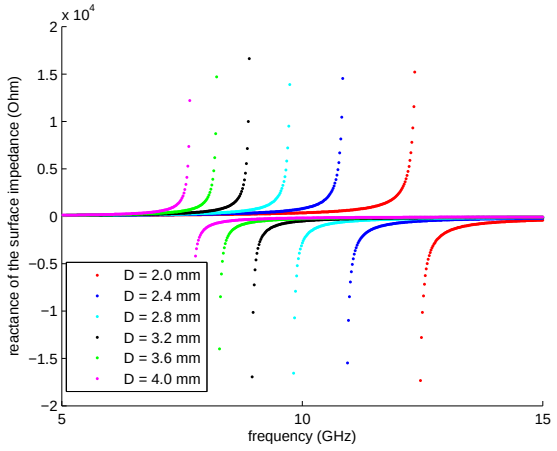

Figure 2.5: Mushroom structures: h = 1.6 mm, g = 0.2 mm, $\varepsilon_r = 4.4$, D varies from 2.0 mm to 4.0 mm.

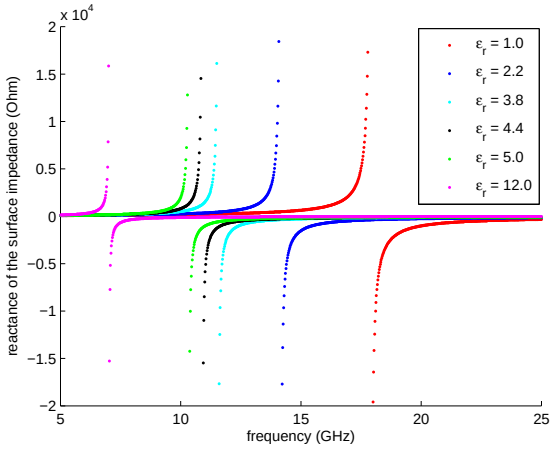

Figure 2.6: Mushroom Structures: D = 2.4 mm, g = 0.2 mm, h = 1.6, ε_r varies from 1.0 to 12.0.

Figure 2.3 and Figure 2.4 reveal that a smaller gap g and a thicker substrate h yield a lower

resonant frequency. Figure 2.5 and Figure 2.6 reveal that an increase in the period D or in the permittivity of the substrate ε_r also cause a lower resonant frequency.

This parallel resonant LC model is not very rigorous, because the formula above cannot accurately describe the behavior of the capacitance and the inductance at high frequencies. In addition, another drawback of the model is that the influence of the incidence angle is neglected.

2.1.2 Transmission-line Model by Simovski

Generally, HIS structures can be divided into two layers: a grounded substrate with periodic vias and a top surface with periodic metal elements. These two layers have been separately investigated for a long time and their history goes back to the end of the nineteenth century.

The first quantitative study on wire grids was done by Lamb in 1898 [88]. In 1946, Mac Farlane [74] solved the scattering problem of a parallel wire grid by using a simple Transmission-line (TL) model. Then several TL models for the case of wire grids in homogeneous media were developed by MacFarlane, Wait [75], and Trentini [76]. Afterward, many contributions have been made in improving the models with various new conditions.

In 1982, Lee et al. [77] obtained an expression for the grid impedance of a surface with inductive or capacitive grid mesh, in a homogeneous medium and at normal incidence, by matching its analytical calculations to numerical data [102].

All the previous work paved the way for investigating the HIS structures by using a TL model. In short, the first layer of HIS structures, such a substrate with periodic vias can be understood by the wire grid model; the second layer, the surface with periodic metal elements can be described by an artificial homogeneous impedance surface behaving like a a capacitive or an inductive grid in certain frequency bands.

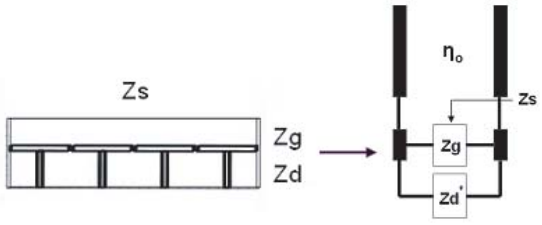

Figure 2.7: Equivalent transmission-line model for the mushroom structure

The TL model is based on the homogenization theory in a quasi-static or low-frequency environment, which suggests that the dimensions of a unit cell of HIS structures should be

much smaller than the wavelength at the operating frequency. In terms of the TL model, the surface impedance Z_s of the mushroom structure can be considered as a parallel connection of the averaged grid impedance (Z_g) and the impedance of the grounded substrate, as seen from the plane of mushroom structure (Z_d) [83]. The description of the TL model for a mushroom structure is illustrated in Fig. 2.7, where the surface impedance of the whole HIS structures can be expressed as an input surface impedance at the top plane of HIS:

$$Z_{s\,(input)} = \left(Z_g^{-1} + Z_d^{-1}\right)^{-1}. \tag{2.5}$$

The surface impedance is concerned with the angle of incidence, thus the cases with TE and TM-polarization wave are respectively considered. Suppose the patch surfaces are parallel to the $x - y$ plane and the vias are set along the direction of the z-axis, a side view of mushroom structure is presented together with different polarized waves in Fig. 2.8.

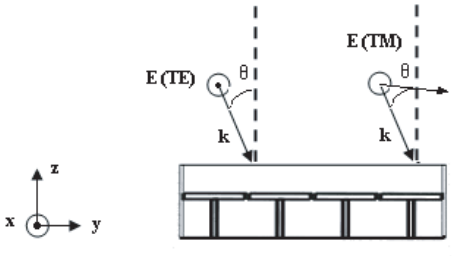

Figure 2.8: TE and TM polarization incident wave

In the case of a TE incident wave, the electric field is always orthogonal to the via, so that no current will be induced on the via and Z_d is not affected. In this case, Z_d is simply regarded as the surface impedance of the dielectric substrate backed with a grounded plane [82]:

$$Z_d^{TE} = \frac{j\eta_0}{\sqrt{\varepsilon_r - sin^2\theta}} \tan(k_{zd}h), \tag{2.6}$$

where $k_{zd} = \omega\sqrt{\varepsilon_0\mu_0(\varepsilon_r - \cos^2\theta)}$ is the vertical component of the wave vector in the refracted wave, ε_r and h is the relative permittivity and the thickness of the substrate, and η_0 is the impedance of free space.

In the case of a TM incident wave, the influence of the vias cannot be neglected and Z_d is regarded as the surface impedance of a wire grid substrate. At low frequency, this layer exhibits like a TEM transmission-line with energy propagating strictly along z [79] and shortened by a ground plane. In this case, Z_d is independent of the incidence angle [82]:

$$Z_d^{TM} = \frac{j\eta_0}{\sqrt{\varepsilon_r}} \tan(k_{zd}h), \tag{2.7}$$

Based on the Babinet's principle, the impedance Z_g is obtained by using an equivalent circuit model for a capacitive screen derived from its complementary structure, an inductive screen [84]. With respect to the TE and TM-incidence, Z_g can be written as:

$$Z_g^{TE} = \frac{1}{j\omega C_g \cos^2\theta}, \tag{2.8}$$

$$Z_g^{TM} = \frac{1}{j\omega C_g}, \tag{2.9}$$

where $C_g = \frac{(\varepsilon_1+\varepsilon_2)D}{\pi} \log(\frac{2D}{\pi g})$.

The TL model presented here is of the first order, and the accuracy can be increased by considering higher orders and dynamic correction [85].

2.1.3 Transmission-line Model by Olli

In comparison with the LC-circuit model given by Sievenpiper, the advantage of the TL model given by Simovski is that the influence of the incidence angle is taken into consideration. However, Olli argued that the accuracy of the analytical models in [79, 86] was not high enough at oblique incidences because the periodicity in one of the tangential directions was not properly taken into account.

Based on the equivalent TL approach, averaged boundary conditions, and the approximate Babinet principle, Olli proposed an advanced TL model and demonstrated the excellent accuracy in [87]. We reproduce his analytical solutions for Z_s of a mushroom structure as follows:

$$Z_S^{TE} = \frac{j\omega\mu \frac{\tan(\beta h)}{\beta}}{1 - 2k_{eff}\alpha \frac{\tan(\beta h)}{\beta}\left(1 - \frac{1}{\varepsilon_r+1}\sin^2\theta\right)} \tag{2.10}$$

$$Z_S^{TM} = \frac{j\omega\mu \frac{\tan(\beta h)}{\beta}\cos^2\theta_2}{1 - 2k_{eff}\alpha \frac{\tan(\beta h)}{\beta}\cos^2\theta_2} \tag{2.11}$$

where $\beta = \omega\sqrt{\varepsilon_0\mu_0(\varepsilon_r - \sin^2\theta)}$, θ is the incidence angle, $\theta_2 = \arcsin\left(\sin\theta/\sqrt{\varepsilon_r}\right)$ and $\alpha = 0.51kD\left(\frac{D-g}{D}\right)^3/(1 - 0.367(\frac{D-g}{D})^3)$ (k is the wave number of the incident wave vector in the effective host medium).

In Fig. 2.9, we compare the two TL models by a parametric study of the incidence angle θ.

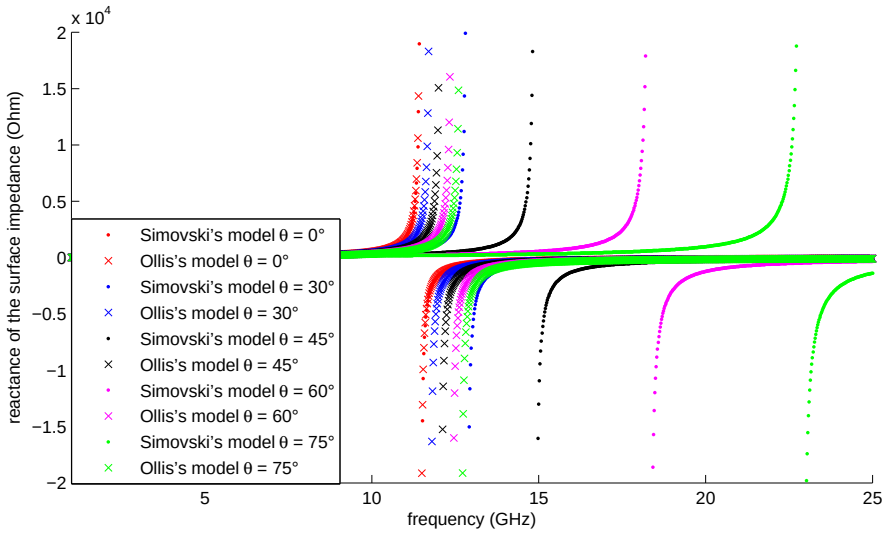

Figure 2.9: Mushroom structure: D = 2.4 mm, g = 0.2 mm, h = 1.6 mm, $\varepsilon_r = 4.4$, θ varies from 0° to 75°, TE case.

The results reveal that the two models are almost in perfect accordance at a normal incidence. When the angle θ increases, the difference between the models becomes more evident. When θ varies from 0° to 45°, the Simovski model detects a resonance shift of about 4 GHz (36.3% of the resonant frequency) and the Olli model detects a resonance shift of about 1 GHz (9% of the resonant frequency). According to [87], a variation of θ won't cause such a big shift of the resonance as predicted by the TL model given by Simovski.

2.2 Jerusalem-Cross Structures

The resonance of the mushroom structures strongly depends on the incidence angle θ. When θ varies from 0° to 60°, the resonance may shift ouside than the resonant band of the structure itself, which will surely affect the performance of HIS structures. This gave birth to the concept of the self-resonant grid HIS structures, whose elements are made from thin metal strips. In comparison with the mushroom structures, these structures may effectively reduce the deviation of the resonance [73].

A well-known example of such a structure is the grid of Jerusalem crosses (JC). Instead of square patches as in mushroom structures, its top surface is composed of Jerusalem crosses. The geometry of a unit cell of such HIS structures is presented in Fig. 2.10.

The analytical models based on the transmission-line theory have been developed [78] and

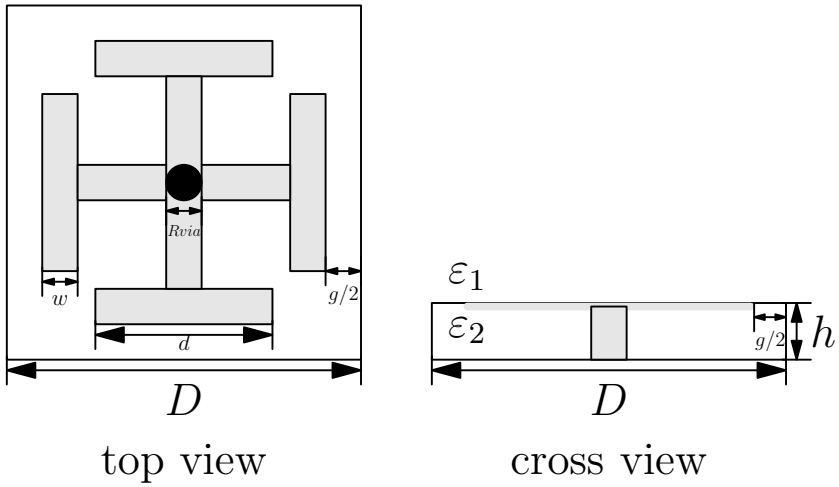

Figure 2.10: Geometry of a unit cell for a Jerusalem-cross structure

applied to investigate the JC structures [79, 80].

2.2.1 Transmission-line Model by Simovski

In terms of the TL model, the JC structures are considered as a parallel connection of a grounded dielectric layer with vias, characterized by Z_d, and a self-resonant grid surface, characterized by Z_g, on the top. Its surface impedance can be expressed exactly the same way as in Eq. 2.5.

The grounded substrate of JC structures has the same grounded substrate as the mushroom structures. So, the impedance Z_d can be formulated just as in Eq. 2.6 and in Eq. 2.7.

The grid impedance Z_g of JC structures is determined by an effective capacitance C_g^{JC} and an inductance L_g^{JC}. The capacitance is caused by the capacitive coupling of adjacent crosses and the inductance is due to the straight arms of the crosses. The grid of metal Jerusalem crosses was first studied as a modified version of a wire mesh model (for the case of the normal incidence only) [89]. Then, the authors of [79] apply it to describe a grid surface for JC structures.

The formula for C_g^{JC} is [89]:

$$C_g^{JC} = \frac{2}{\pi}\varepsilon_r\varepsilon_0 d\left[\log\csc(\frac{\pi g}{2D}) + F\right], \tag{2.12}$$

with $F = \frac{Qu^2}{1+Q(1-u)} + \left(\frac{du(3u-2)}{4\lambda'}\right)^2$, $Q = \sqrt{1-\left(\frac{d}{\lambda'}\right)^2}$, $u = cos^2\left(\frac{\pi g}{2d}\right)$, $\lambda' = \frac{2\pi}{k'}$. These formulas are valid when $h < d$.

The effective inductance L_g^{JC} is [79]:

$$L_g^{JC} = \frac{\eta'}{2\omega} \cdot \frac{k'D}{\pi} \log \frac{2D}{\pi\omega}, \tag{2.13}$$

with $\eta' = \eta_{0/\sqrt{\varepsilon_r}}$, η_0 is the wave impedance of free space.

With respect to different polarizations, the impedance Z_g of JC structures is written as:

$$Z_g^{TE} = (j\omega L_g^{JC} + \frac{1}{j\omega C_g^{JC}}), \tag{2.14}$$

$$Z_g^{TM} = cos^2\theta((j\omega L_g^{JC} + \frac{1}{j\omega C_g^{JC}}). \tag{2.15}$$

We carry out parametric studies to investigate the relationship between the geometrical dimensions and the surface impedance of the JC structures. The study on the parameters of h, g, D are not repeated, because the influence of these geometrical parameters can be referred to the cases with a mushroom structure.

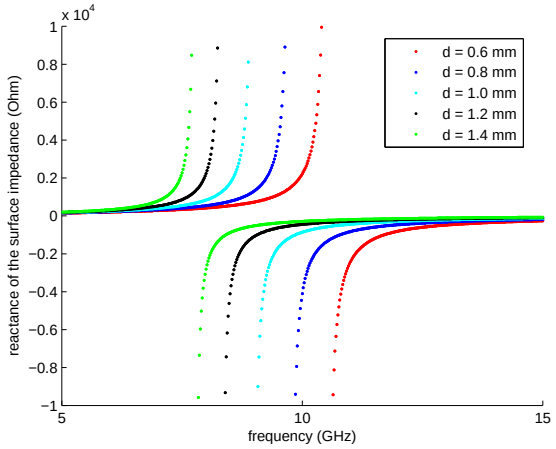

Figure 2.11: JC structures: D = 2.4 mm, g = 0.4 mm, h = 3 mm, w = 0.2, $\varepsilon_r = 4$, d varies from 0.6 mm to 1.4 mm.

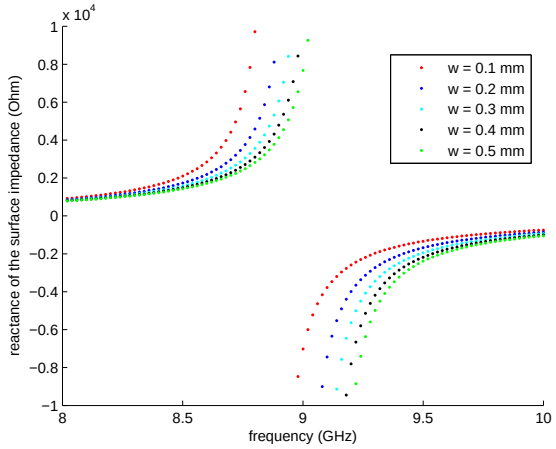

Figure 2.12: JC structures: D = 2.4 mm, g = 0.4 mm, h = 3 mm, d = 1.0, $\varepsilon_r = 4$, w varies from 0.1 mm to 0.5 mm.

Figure 2.11 and Figure 2.12 reveal that the resonance of a JC structure is strongly affected by the variation of the metal strip length d, but less affected by the variation of the metal strip width w, when the array period D is fixed.

In addition to the geometrical parameter, we also check the shift of the resonant frequency versus the incidence angle, as seen in Fig. 2.13. When θ varies from 0° to 75°, the resonance of

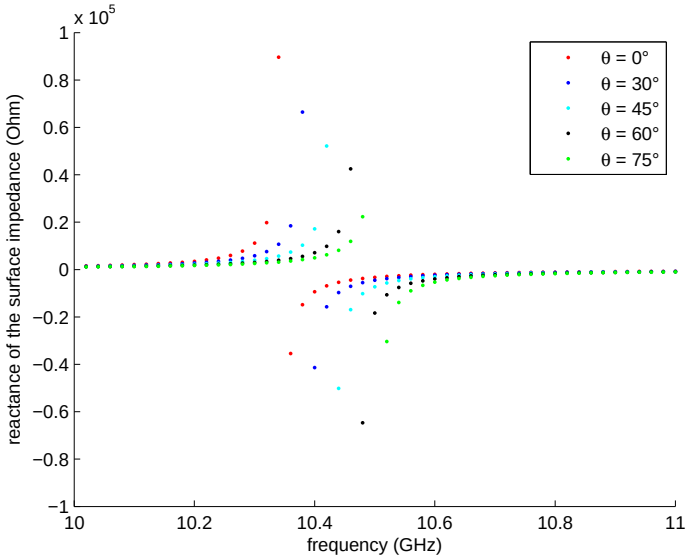

Figure 2.13: JC structure: D = 2.4 mm, g = 0.4 mm, h = 1.6 mm, d = 1.4, $\varepsilon_r = 4.4$, θ varies from 0° to 75°.

the JC structure shifts around 0.2 GHz (2% of the resonant frequency). As compared with the mushroom structures, the JC structures exhibit a good stabilization of resonance with respect to θ.

2.2.2 Transmission-line Model by Hosseini

In [81], Hosseini proposed a similar TL model for JC structures which took the effect of the ground plane spacing on Z_g into account. This model combines the theory of the coupled microstrip lines with the theory of the transmission lines and its equivalent circuit model is illustrated in Fig. 2.14 (from [81]).

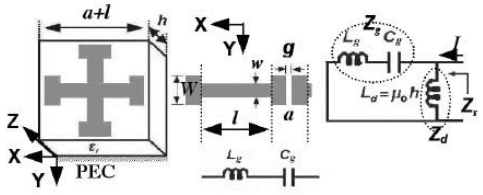

Figure 2.14: JC structue and the circuit model)

Similar to the TL model proposed by Simovski, the grid impedance Z_g of JC structures has the effective inductance $L_g^{JC'}$ and the effective capacitance $C_g^{JC'}$like this:

$$Z_g^{JC'} = j\omega L_g^{JC'} + \frac{1}{j\omega C_g^{JC'}}. \tag{2.16}$$

In the TL model given by Hosseini, $L_g^{JC'}$ is assimilated a T-line section:

$$L_g^{JC'} = \frac{2Z_0 \tan(\frac{kl}{2})}{\omega}, \tag{2.17}$$

and $C_g^{JC'}$ includes the effect of the substrate's thickness, this way:

$$C_g^{JC'} = \frac{2W}{\pi}\varepsilon_0\varepsilon_{reff} \cosh\left(\frac{a}{g}\right), \tag{2.18}$$

where $k = \omega\sqrt{\mu_0\varepsilon_0\varepsilon_r}$, and Z_0 is the characteristic impedance, expressed as:

$$Z_0 = \frac{\eta_0}{\sqrt{\varepsilon_{reff}}} \cdot \begin{cases} \frac{1}{2\pi}\ln(\frac{8h}{w} + \frac{w}{4h}) & when\ \frac{w}{h} \leq 1 \\ \left[\frac{w}{h} + 2.42 - 0.44\frac{h}{w} + (1 - \frac{h}{w})^6\right]^{-1} & when\ \frac{w}{h} > 1 \end{cases}, \tag{2.19}$$

with $\varepsilon_{reff} = \frac{\varepsilon_r+1}{2} + \frac{(\varepsilon_r-1)}{2\sqrt{1+10\frac{h}{W}}}$.

The work of Hosseini pointed out that the model is valid when the ratio (d/h) of strip width over substrate thickness is less than two.

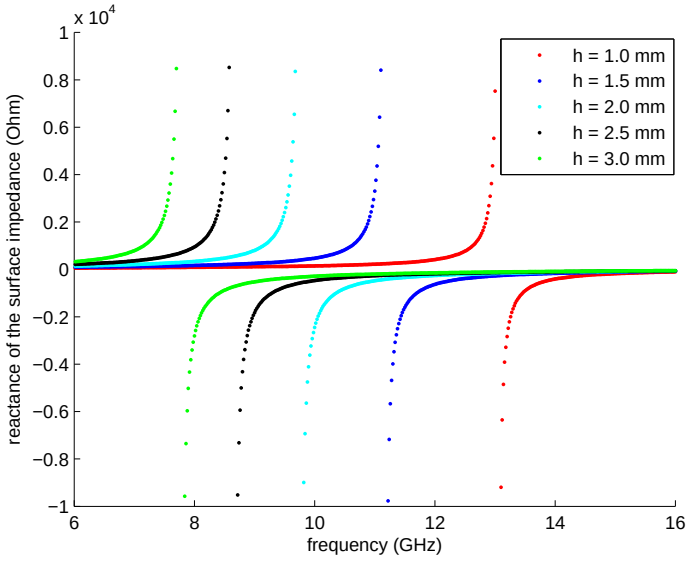

Figure 2.15: JC structures: D = 2.4 mm, g = 0.4 mm, d = 1.4 mm, w = 0.2, $\varepsilon_r = 4$, h varies from 1.0 mm to 3.0 mm.

In Fig. 2.15, we present a parametric study in terms of the substrate thickness using the TL

model given by Hosseini. It is observed that a small variation of the substrate thickness may cause a dramatic shift of the resonance. In comparison with the TL model given by Simovski, this one is more sensitive to the thickness of the substrate.

2.3 Conclusion

In the foregoing sections, we introduced three analytical models for mushroom structures (the LC circuit model proposed by Sievenpiper, the TL model proposed by Simovski and the TL model proposed by Olli) and two analytical models for Jerusalem-cross structures (one is proposed by Simovski and the other one is proposed by Hosseini). Then we did a parametic study on these two types of HIS structures. This study helped us to understand the relationship between the geometry and the physical mechanism. Some results may also offer some guidelines in HIS-geometry design.

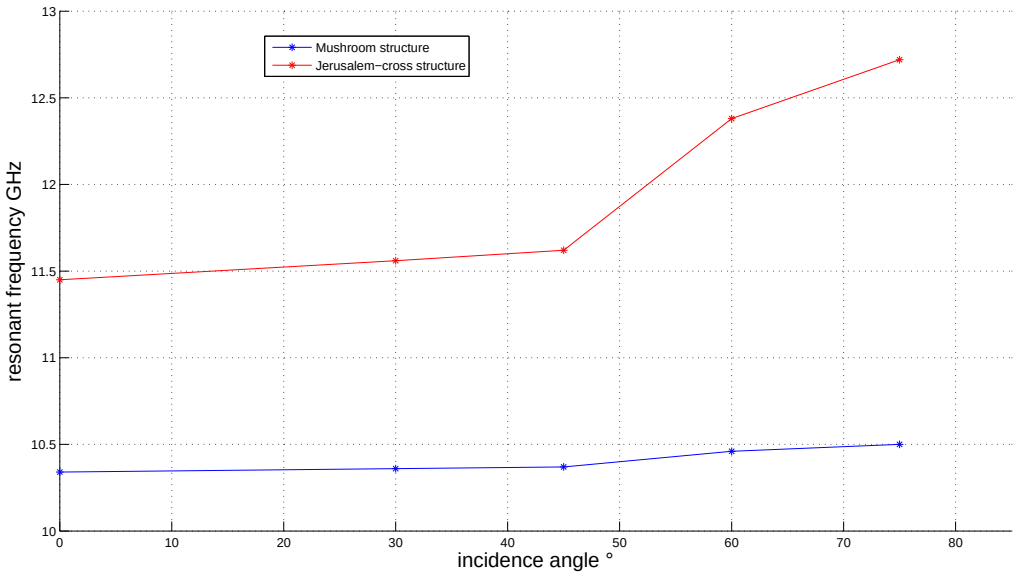

Figure 2.16: Influence of the angle of incident wave on the resonance for two types of HIS structures

Meanwhile, from the tests, we also verified that if the dimension of the unit cells are comparable, the Mushroom structures are less immune to the variation of the angle of incident wave than the Jerusalem-cross structures. Here, we reprocess the data obtained in Fig. 2.9 and in Fig. 2.13 and plot their results on the same figure (Fig. 2.16). From this figure, we observe that the variation of the resonance for the mushroom structures is around 1.3 GHz and the resonance

for the Jerusalem-cross structure is rather stable when varying the incidence angle from 0° to 75°.

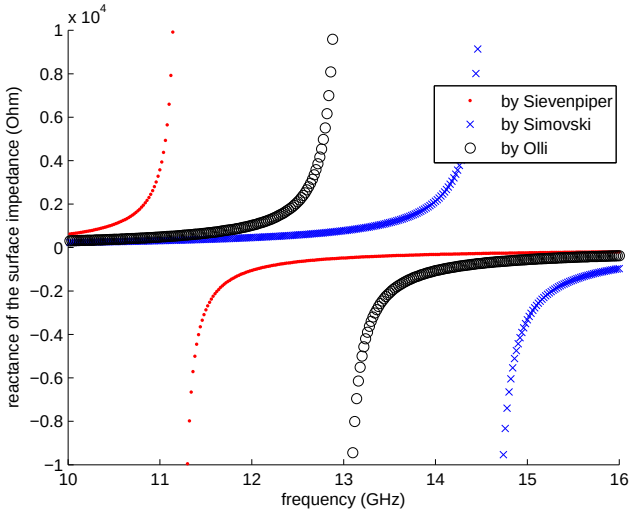

Figure 2.17: Comparison of surface impedances as calculated by different analytical methods for a Mushroom structure (D = 10 mm, g = 5 mm, h = 2 mm, $\varepsilon_r = 4.4$)

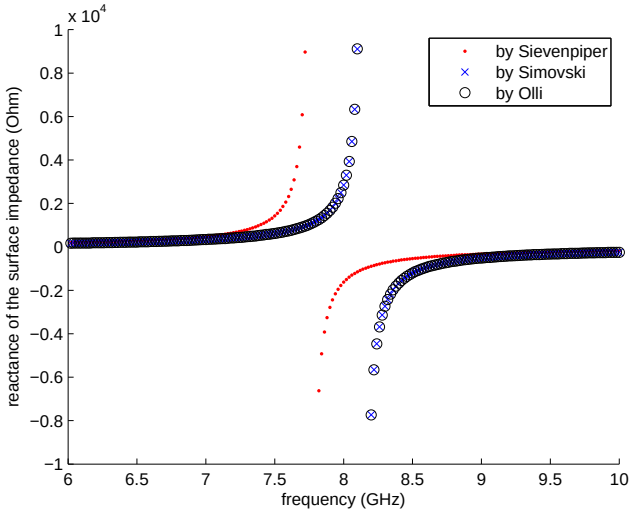

Figure 2.18: Comparison of surface impedances as calculated by different analytical methods for a Mushroom structure (D = 2.4 mm, g = 0.015 mm, h = 1.6 mm, $\varepsilon_r = 4.4$)

Furthermore, we also make a comparison of the surface impedance graphs (over the frequency) produced by different analytical models for different types of structures. A series of

tests have been made and here we first present two representative cases (Case 1 and Case 2) with two mushroom structures of different dimensions.

In Case 1, the resonances predicted by these three models are different from each other, as seen in Fig. 2.17. There are 2 GHz difference between them. In Case 2, the Simovski's model coincides with the Olli's model, while the resonance achieved by Sievenpiper's model is a little different from the others, as seen in Fig. 2.18. Compared with Case 1, the dimension of the unit cell in Case 2 is much smaller (the wavelength is around 15 times larger than the period of the unit cell), which is closer to the requirements of theory of homogenization. Thus, it is understandable that the analytical results from different models are closer to each other in Case 2.

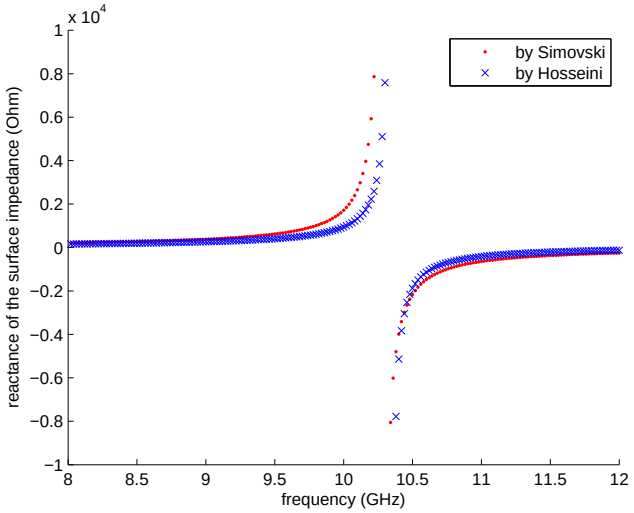

Figure 2.19: Comparison of surface impedances calculated by different analytical methods for a Jerusalem-cross structure (D = 4.8 mm, g = 1 mm, d = 2 mm, w = 0.9 mm, h = 1.6 mm, ε_r = 4.4)

After the comparison on mushroom structures, we also present two representative cases (Case 3 and Case 4) with two Jerusalem-cross structures of different dimensions. In Case 3, the two methods are in good agreement, as seen in Fig. 2.19. In Case 4, the resonance obtained by Hosseini's model is around 4 GHz higher than the one obtained by Simovski's model, as seen in Fig. 2.20. This time, the extent of difference among different methods mainly depend on the chosen geometry dimensions, which can not be easily interpreted by the theory of homogenization.

Generally speaking, the analytical models are not rigorous and each model has its own constraints associated with its geometrical parameters. Without a reference, such as a measurement

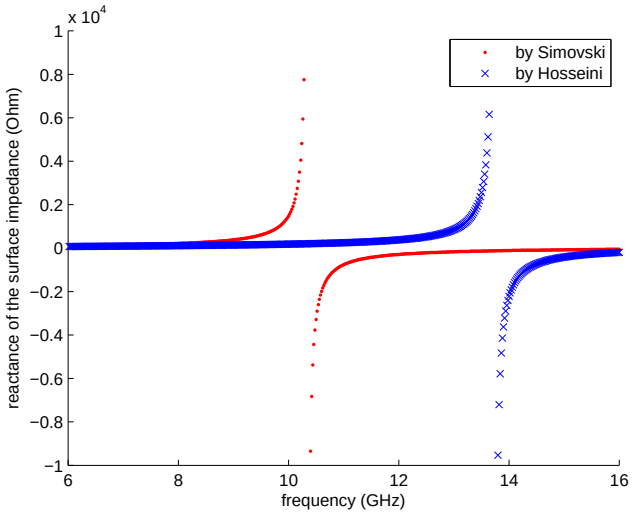

Figure 2.20: Comparison of surface impedances calculated by different analytical methods for a Jerusalem-cross structure (D = 2.4 mm, g = 0.4 mm, d = 1.4 mm, w = 0.2 mm, h = 3 mm, $\varepsilon_r = 4.4$)

result, these analytical calculations are only useful as heuristic approaches.

Chapter 3

Numerical Modeling

In the previous chapter, we presented several analytical models for HIS structures. These models provide us with an idea of the properties of HIS structures, but, in face of the complex HIS geometries, they are rather limited and weak. The fact is that it is not easy to find empirical formulas to describe the behavior of such structures appropriately. In some cases, it's impossible to find analytical solutions for a complicated problem.

Nevertheless, with the development of computing capabilities and numerical algorithms, handling the HIS structures with complicated geometries becomes easy. Several numerical methods have been proposed in resolving electromagnetic problems [90], such as the finite-difference time domain method (FDTD) [91], the Method of Moments (MoM)[92], etc. These numerical methods have also been applied to compute the characteristics of HIS structures [31].

Among all kinds of numerical methods, the "3D Finite Element Method (FEM)" using edge elements [93, 94, 95] is chosen in this work. One advantage of this method is that it allows a characterization of arbitrary shaped structures without having parasitic solutions [97, 96].

In this chapter, we'll present the numerical modeling of HIS structures, validate their results and discuss their limitations.

3.1 Symmetric HIS Structures

3.1.1 Introduction to Numerical Modeling

In Chapter 2, two rotationally symmetric HIS structures: the mushroom structure and the Jerusalem-Cross (JC) structure were investigated using analytical models. In this section, we'll begin our work by numerically modeling the same structures. One advantage of using them is

that the numerical model can be validated by comparing their analytical results and numerical results. Another advantage is that the calculations for symmetric structures can be simplified, as compared with those for the asymmetric ones.

Let us take the mushroom structure as an example to explain how to build the numerical model. The mushroom structure is spatially periodic in two dimensions, so it suffices to model one unit cell instead of the whole HIS structures, by applying appropriate boundary conditions. Figure 3.1 depicts a cubic study domain composed of one unit cell of the mushroom structure.

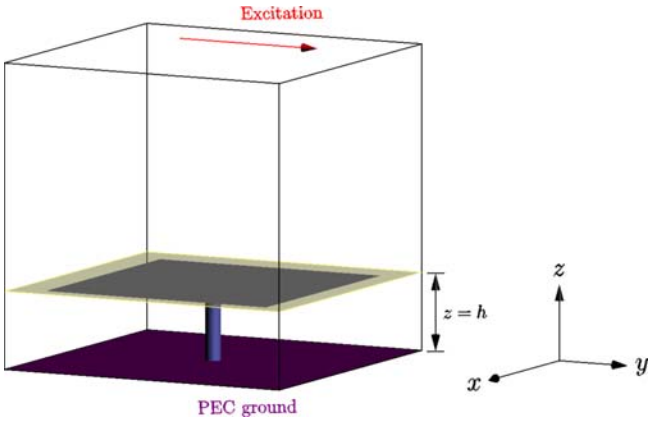

Figure 3.1: Numerical modelling of a HIS unit cell with the mushroom structure

1) The plane xoy is the base plane (and the bottom surface, $z = 0$) of the study domain. This plane will be modeled as a ground plane by using the perfect electrical conductor (PEC) condition .

2) The unit cell of mushroom structure includes the region $0 \leqslant z \leqslant h$. The intermediate region ($0 < z < h$) represents the substrate, which supports the metal patch of the HIS structure. It has permeability μ and permittivity ε, both possibly complex and frequency-dependent. The metal patch on the top surface of HIS structures is supposed to be contained in the plane $z = h$. The via is represented by a thin wire in the region $0 < z < h$, which connects the ground plane to the top HIS surface. Metallic elements of HIS structures are all modeled to a PEC condition.

3) The region $z > h$ is considered as free space.

4) The study domain is illuminated by an electromagnetic wave on the top surface, so this surface will be numerically treated by imposing a Dirichlet condition.

5) The boundary conditions on the lateral walls depend on the mode of excitation and on the geometry of the HIS structures.

Assuming the excitation is a constant electric field along the x-axis, this excitation is symmetric with respect to all planes that are parallel to the $x - z$ plane and antisymmetric with

respect to all planes that are parallel to the $y-z$ plane. Since the components of the HIS structure are symmetric with respect to the plane $y = D/2$ and to the plane $x = D/2$, the E-field in the study domain will have the same symmetry properties as the excitation, in accord with the Curie principle: the symmetry elements of the causes must be found in their effects [98]. In this case, the two opposite side walls parallel to the x-axis are modeled by a perfect magnetic conductor (PMC) condition. The other two opposite side walls parallel to the y-axis are assigned with a PEC condition. This way, the symmetry of E-field in the study domain is not disturbed by the choice of these boundary conditions on the side walls.

3.1.2 Numerical Calculations

After an introduction to the numerical model for HIS structures, we will adopt this model to calculate the grid impedance, the surface impedance and the phase of the reflection coefficient in a numerical way.

Grid Impedance

When the dimension of the unit cell is relatively small compared to the wavelength in the medium, the tangential component of the average electric field on the grid surface is proportional to the average current induced in the grid. The grid impedance can be defined as the ratio of this averaged E-field over the averaged current, as seen in eq. 3.1. The average current is equal to the jump of the tangential component of the average magnetic field across this grid surface. In the numerical model, we calculate the average tangential magnetic field on two surfaces located at two sides of the grid surface, a very small distance δh apart. The average current is defined as the difference of the two average magnetic fields, $\langle H_{t+}\rangle - \langle H_{t-}\rangle$.

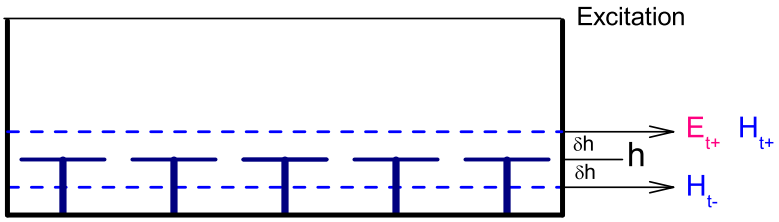

Figure 3.2: Description of the grid impedance

The grid impedance Z_g is thus defined as:

$$\langle Z_g\rangle = \frac{\langle E_{t+}\rangle}{\langle H_{t+}\rangle - \langle H_{t-}\rangle}, \tag{3.1}$$

where: $t+$ means the tangential values at the surface just above the HIS planar surface, $z = h + \delta h$ and $t-$ means the tangential values at the surface just below the HIS planar surface, $z = h - \delta h$. The symbol $\langle\rangle$ denotes the average values.

The average tangential E-field is also calculated on the surface $z = h + \delta h$, instead of $z = h$, because of the dramatic irregularities of the tangential E-field there.

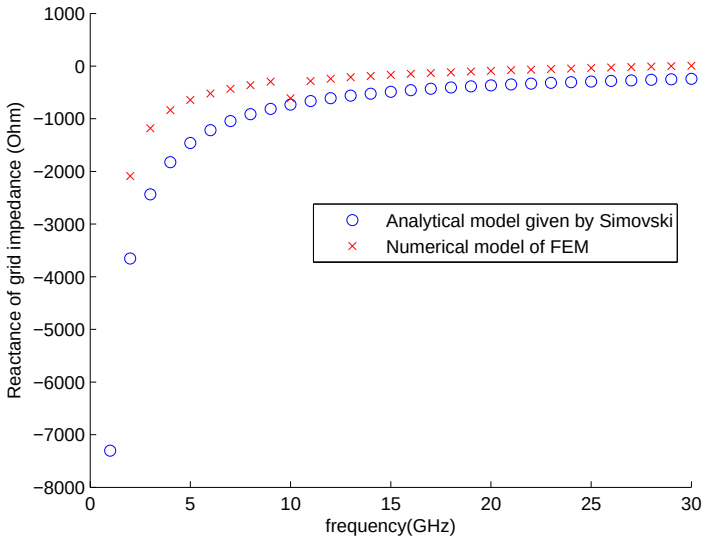

Figure 3.3: Grid impedance for the mushroom structure

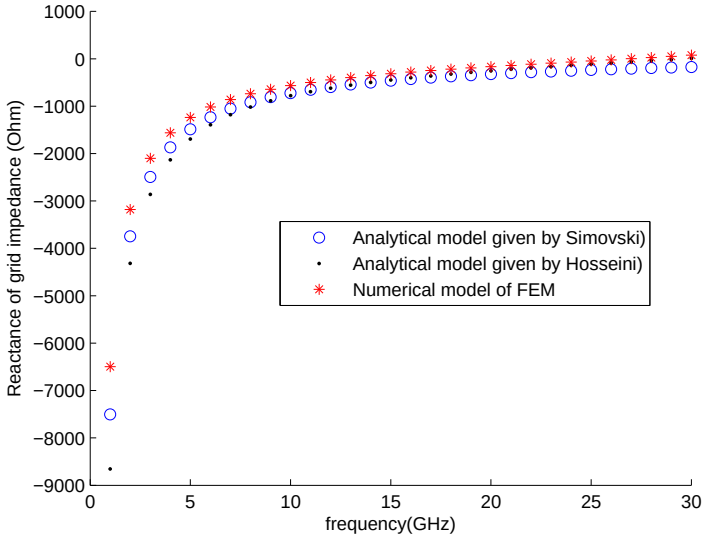

Figure 3.4: Grid impedance for the Jerusalem structure

We calculate the grid impedance respectively for a mushroom structure (as seen in Fig. 3.3) and for a JC structure (as seen in Fig. 3.4) by using this numerical definitions and compare them with the analytical calculations presented in the previous chapter. Both of these figures show that the numerical results and the analytical results are in good accordance, which means that our numerical definition is workable.

Surface Impedance

HIS structures can be characterized by their surface impedance Z_s, which is generally presented in the form of a 2×2 matrix:

$$Z_s = \begin{bmatrix} Z_{11} & Z_{12} \\ Z_{21} & Z_{22} \end{bmatrix}. \tag{3.2}$$

If the mushroom structures and the JC structures are rotated by 90° (The Z_s matrix commutes with matrix $\begin{bmatrix} 0 & -1 \\ 1 & 0 \end{bmatrix}$, which represents a 90° rotation), their geometries stay the same. Hence, the surface impedance of such structures can be simplified as follows:

$$Z_s = \begin{bmatrix} Z_{11} & Z_{12} \\ Z_{21} & Z_{22} \end{bmatrix} \Longrightarrow Z_s = \begin{bmatrix} Z_s & 0 \\ 0 & Z_s \end{bmatrix}. \tag{3.3}$$

Because of the rotational symmetry, the calculation of a matrix with four unknown entries turns into a calculation of a matrix with only one unknown entry. In the former case, computing the surface impedance requires two different oriented excitations. In the latter case, one excitation suffices.

In modeling the surface impedance Z_s, two different approaches (here referred to as "scheme 1" and "scheme 2") are investigated, as seen in Fig. 3.5.

In scheme 1, the surface impedance $Z_s(scheme\,1)$ is considered as a parallel combination of the grid impedance Z_g and the dielectric impedance Z_d:

$$Z_s(scheme\,1) = \frac{Z_g(numerical) \cdot Z_d(analytical)}{Z_g(numerical) + Z_d(analytical)}, \tag{3.4}$$

where Z_g is numerically calculated as in eq. 3.1, but Z_d is obtained through the analytical model of the previous chapter. This scheme can be regarded as a transition from the analytical model to the numerical model.

In scheme 2, the surface impedance Z_s is globally defined as the ratio of the average tangential E-field over the average tangential H-field on some observation surface. It is assumed that such

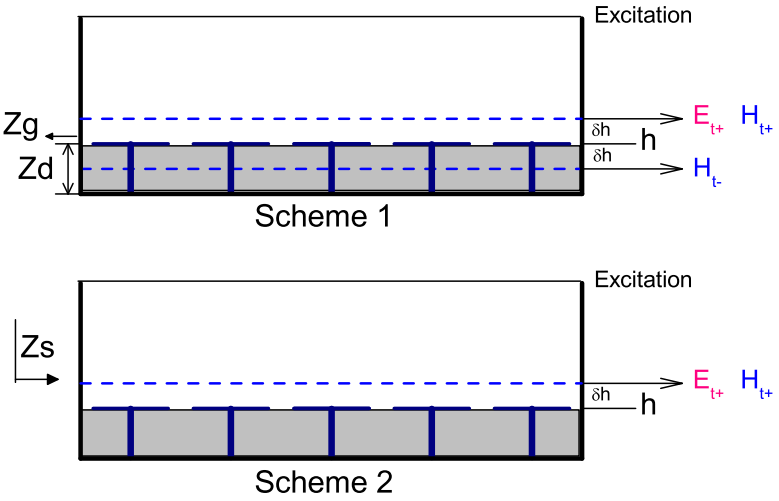

Figure 3.5: Two schemes for calculating the surface impedance in numerical model

an impedance reflects all the characteristics of HIS structures that lie below this observation surface. In theory, we could select $z = h$ (the top surface of the mushroom structures) as observation surface. But, in order to avoid the bad effect of the large variation of the tangential E-field on the grid surface, the observation surface is chosen at $z = h + \delta h$ instead. After calculating the average tangential electric field and the average tangential magnetic field on the observation plane, the surface impedance $Zs(Scheme\ 2)$ is defined as:

$$Z_s(scheme\ 2) = \frac{\langle E_{t+} \rangle}{\langle H_{t+} \rangle}. \tag{3.5}$$

As mentioned before, all the structures are 90° rotationally symmetric, so the calculation does not require two different excitations. In our simulation, only one excitation of the E-field with non zero component either along the x-axis or along the y-axis is needed.

Figure 3.6 exhibits four results about the surface impedance for a Mushroom structure, two of which are obtained by analytical methods [22, 79]; the other two are calculated by the two schemes proposed in this section. The dimension of the Mushroom structure is taken from [70], whose experimental results show that the model with scheme 2 is more effective than the one with scheme 1.

Figure 3.7 exhibits also four results about the surface impedance, but for a JC structure. Two analytical results are obtained by using the model proposed by Simovski [79] and the model proposed by Hosseini [81]; the two numerical results are obtained by using our two different schemes. It is observed that the numerical model with scheme 2 agrees with Simovski's analytical model. Among the four results, the numerical model with scheme 1 predicts the lowest resonant

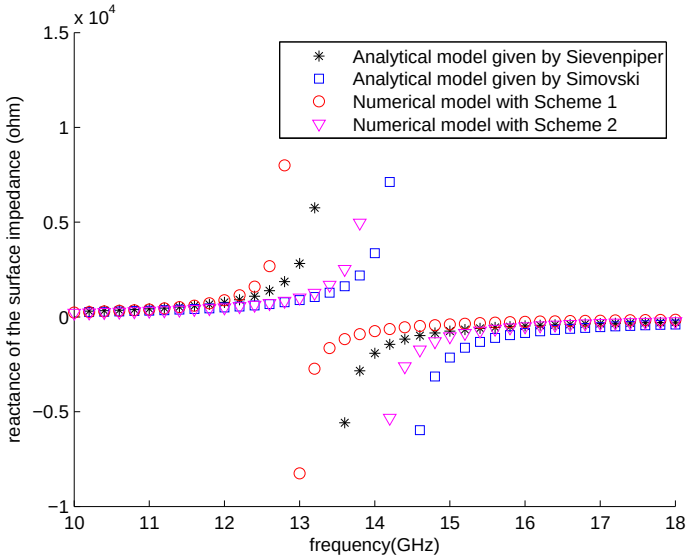

Figure 3.6: Analytical and numerical results of the surface impedance for a Mushroom structure (D = 2.4 mm, g = 0.015 mm, h = 1.6 mm, $\varepsilon_r = 2.2$)

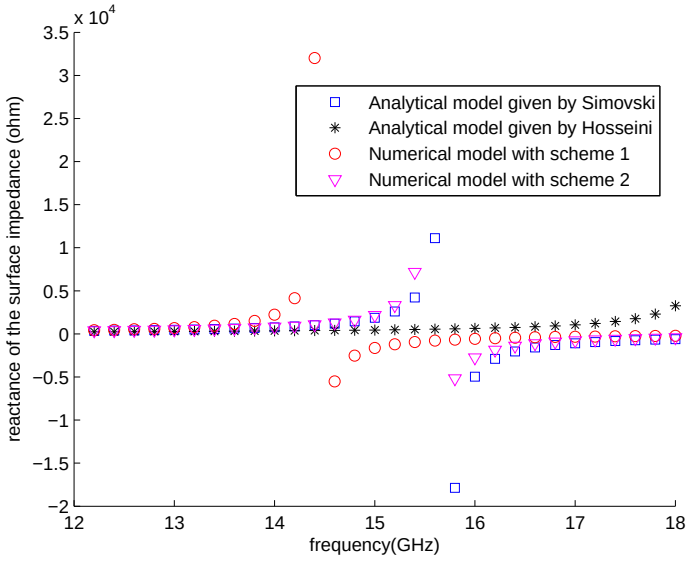

Figure 3.7: Analytical and numerical results of the surface impedance for a JC structure (D = 2.4 mm, g = 0.4 mm, h = 1.6 mm, d = 1.4, $\varepsilon_r = 2.2$)

frequency at about 14.2 GHz and Hosseini's model predicts the highest resonance, which lies beyond the range of this figure, and is at about 18.2 GHz. The effectiveness of these models will be checked by a numerical calculation with the CST in the next subsection.

In addition, we investigate our model with two cases: with or without a via in the HIS

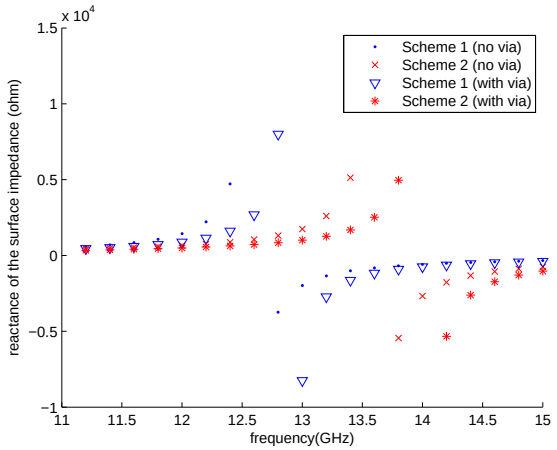

Figure 3.8: The influence of the via for the mushroom structure

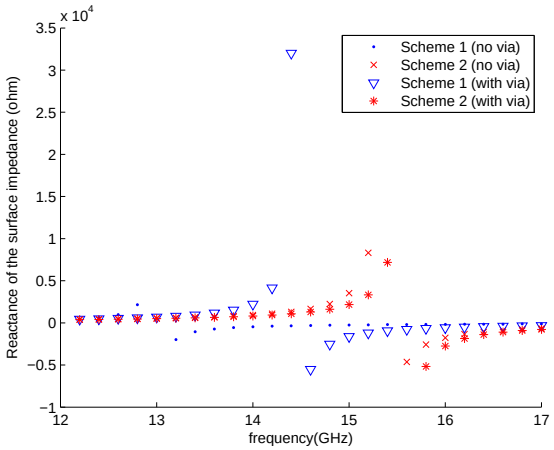

Figure 3.9: The influence of the via for the Jerusalem structure

structure at normal incidence. In our simulations, the E-field of the excitation is always parallel to the top planar surface of the HIS structures, so no electric field will propagate across the vertical vias. At low frequency, the existence of the thin vias can be totally neglected. However, at high frequency, there may exist a small difference between the two cases.

Two simulations are carried out as shown in Fig. 3.8 and Fig. 3.9. The former figure corresponds to a Mushroom structure and the latter represents a JC structure, which both show that the presence of the via may create a resonance shift to a higher frequency.

Phase of the Reflection Coefficient

Compared with the surface impedance Z_s, the phase of the reflection coefficient ϕ is a more readable parameter. This is because the range of ϕ is bounded between 180° and −180°, so no extremely high values will appear on the figure, contrary to what happens with Z_s.

If the HIS structure is designed as a ground plane for an antenna system, the effective frequency band of the HIS structure should cover the working band of the antenna. Following the reference [70], we shall set the effective frequency band of HIS structures as $-90° \leq \phi \leq 90°$.

Figure 3.10 presents the phase of reflection coefficient for a mushroom structure and the numerical results show that the analytical model proposed by Simovski, the numerical model with scheme 2 are in good agreement with the numerical results from the CST below 13 GHz. At higher frequency, the numerical model with scheme 2 are a bit different from the others and predict a narrower bandwidth.

Figure 3.11 presents the phase of reflection coefficient for a JC structure. In this case, the

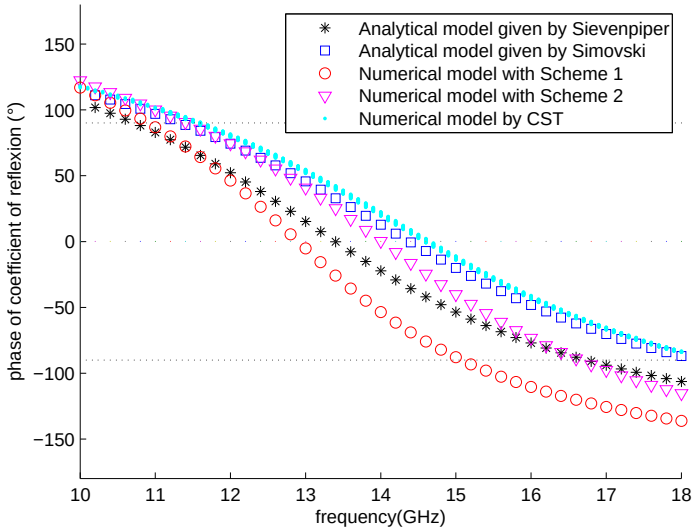

Figure 3.10: Analytical and numerical results for the phase of reflection coefficient for a Mushroom structure (D = 2.4 mm, g = 0.015 mm, h = 1.6 mm, ε_r = 2.2)

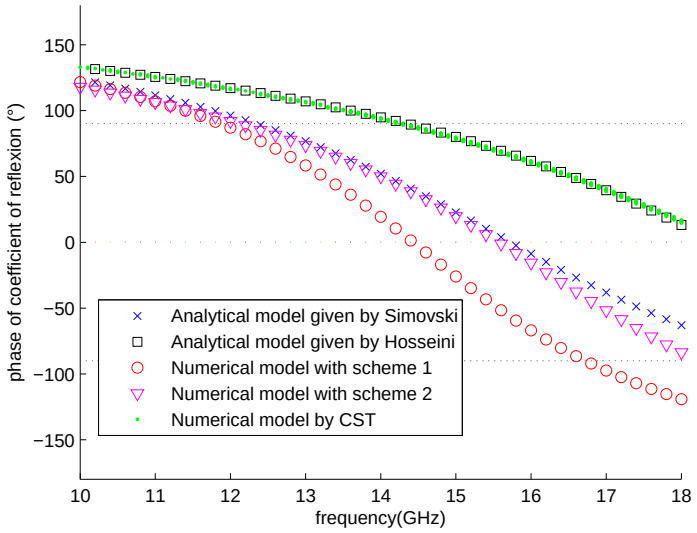

Figure 3.11: Analytical and numerical results for the phase of reflection coefficient for a JC structure (D = 2.4 mm, g = 0.4 mm, h = 1.6 mm, d = 1.4, ε_r = 2.2)

results obtained by Hosseini's analytical model match the ones got from the CST. The results calculated by the numerical model with scheme 2 is close to those obtained by Simovski's model, but a little different from the others.

Both figures show that scheme 1 is less effective than the other models, especially at high

frequency. As a matter of fact, this model is a combination of a semi-numerical computation and a semi-analytical computation. At high frequency, the analytical methods are less effective, which results in a less accurate prediction. Thus, we shall not use this scheme any longer in this work.

Scheme 2 is now validated through the calculations of symmetric HIS structures. Its effectiveness will be further checked against experimental measurements.

3.1.3 Different Combinations of Boundary Conditions

In building numerical models, boundary conditions should be appropriately chosen and discretized. For a fourfold rotationally symmetric HIS structure, the four lateral boundary surfaces of the study domain may be equipped with two different combinations of boundary conditions. In this subsection, we will discuss and analyze these two possible combinations in the example case of the Mushroom structure.

Combination 1: Two pairs of periodic boundary conditions (PBC)

According to Curie's principle (that symmetries of effects reflect the symmetries of causes), if the excitation is uniform and the structures are periodic, the resulting E-fields will be periodic. Therefore, one possible combination of boundary conditions is: equip the four lateral boundary surfaces of the study domain with two pairs of PBC, one for each pair of walls facing each other.

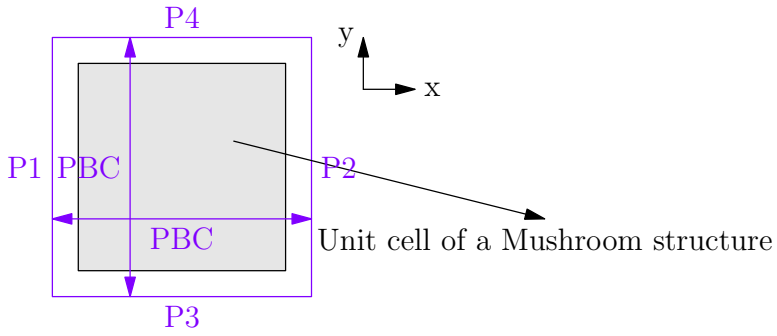

Figure 3.12: Two pairs of periodic boundary conditions applying on a unit cell of Mushroom structure

Assume that the top planar surface of the Mushroom structure is contained in a plane parallel to the $x-y$ plane, and that the whole structure is periodic in the direction of the x-axis and of the y-axis. One pair of PBC is applied to the two boundary surfaces parallel to the plane, marked as P1 and P2 in Fig. 3.12. Another pair of PBC is applied to the two boundary

surfaces parallel to the $x - z$ plane, marked as P3 and P4 in Fig. 3.12. It is to be noted that the two faces concerned by a PBC should be meshed identically: each edge on one surface must find its translate counterpart on the opposite surface.

Combination 2: One group of PEC conditions + one group of PMC Conditions

Before discussing the second combination of boundary conditions, we should explain the concept of "even" field and "odd" field with respect to a "mirror plane", that is to say, a plane with respect to which the whole structure has reflection symmetry. The mirror image of a point x (with respect to the plane π) we shall denote sx. The mirror image of a vector v, which one can conceive as joining point x to point y, is by definition the vector joining point sx to sy, and we denote this vector by sv.

Now, suppose the E-field is equal to $E(x)$ at a given point x, and to $E(sx)$ at the mirror image sx of point x. For a general field, the vector $E(sx)$ has no relation with the mirror image $s(E(x))$ of the vector $E(x)$. By definition, *odd* fields E, also called *antisymmetric* fields (with respect to plane π), are those for which $E(sx) = -s(E(x))$, as illustrated by Fig. 3.14. *Even* fields, also called *symmetric* fields, are those for which $E(sx) = s(E(x))$, as seen on Fig. 3.13. For shortness, we shall say that π is an *odd mirror*, or an *even mirror* relative to the field E.

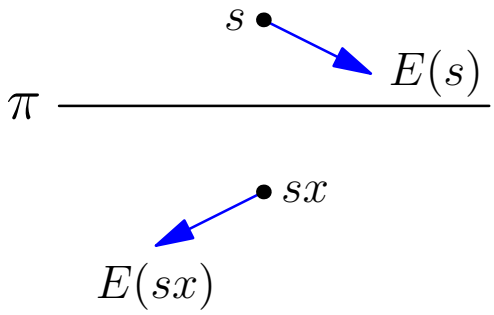

Figure 3.13: Odd E-field mirror plane

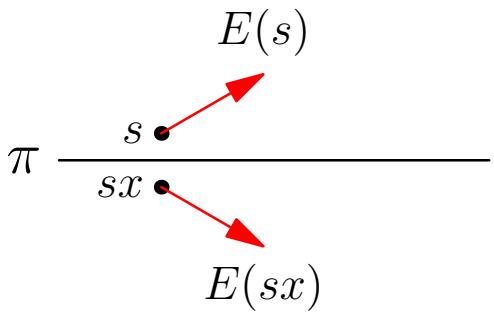

Figure 3.14: Even E-field mirror plane

We may now describe the behavior of the curl operator with respect to mirror symmetries as follows: If a field E is even with respect to a plane, its $\nabla \times E$ will be odd, and if E is odd, $\nabla \times E$ will be even. From the Maxwell's equations, it results that if E is even with respect to π, then B is odd, and hence (when permeability is a scalar), H is odd too. We shall say, again for shortness, that π is an *electric mirror* when E is odd and H even, and a *magnetic mirror* when E is even and H odd. By letting x and its mirror image sx coincide on Fig. 3.13, we see that $n \times E = 0$, as if the plane was coated with a perfect electric conductor, in the case of an

electic mirror. For a magnetic mirror, $n \times H = 0$, as if the plane was coated with a “perfect magnetic conductor”, that is to say, a body with infinte permeability.

It may happen that the electromagnetic fields are symmetric or antisymmetric with respect to a particular plane. Because of the Curie principle, it happens for a mirror-plane of the whole structure when the source of the field (a given current density, or a given excitation field) is itself odd or even with respect to this same plane. In that case, the resulting field has the same mirror symmetries as the excitation field, so the computation can be reduced to one half-space, above or below the mirror plane.

This is done as follows. Suppose we know that, for some reason, π is an electric mirror (odd E, even H). We shall be able to solve the Maxwell equations on one side of π only, instead of in the whole space, by imposing to the field E the artificial boundary condition $n \times E = 0$ on π . This is called a "perfect electric boundary condition" (PEC for short). If π is a magnetic mirror (even E, odd H), the boundary condition $n \times H = 0$ on π will achieve the same reduction to a half-space. This one is called a "perfect magnetic boundary condition" (PMC for short).

In HIS structures, there can be many possible mirror planes. Suppose such a structure is periodic both in the direction of the x-axis and in the direction of the y-axis. Moreover, this structure is geometrically symmetric with respect to some reference plane π_r, which is parallel to the x-axis and to the z-axis. Instead of modeling the whole structure by a unit cell equipped with two pairs of PBC on its four lateral boundary surfaces, we may assign a PMC condition to the two boundary surfaces parallel to the x-axis, provided the excitation E-field (a uniform field, in our studies) is along the x-axis (as seen in Fig. 3.15). This is because such an excitation field is even with respect to π_r, so the two opposite boundary surfaces parallel to the plane π_r, behave like magnetic mirrors. When the excitation E-field is along the y-axis, and thus odd with respect to π_r, one may use a pair of PBC on the faces parallel to the y-axis together with PEC conditions on the faces parallel to the x-axis (as seen in Fig. 3.16).

The Mushroom structure is simultaneously symmetric on the direction of the x-axis and of the y-axis. So another possible combination of boundary conditions is, when the excitation E-field is along the x-axis (see in Fig. 3.17): PEC conditions on the two boundary faces parallel to the x-axis and PMC conditions on the two boundary faces parallel to the y-axis. The setup of these two groups of boundary conditions will be exchanged when the excitation E-field is along the y-axis (seen in Fig. 3.18).

To conclude: for a doubly symmetric HIS structure, such as the Mushroom structure, the two combinations of boundary conditions are equivalent and workable.

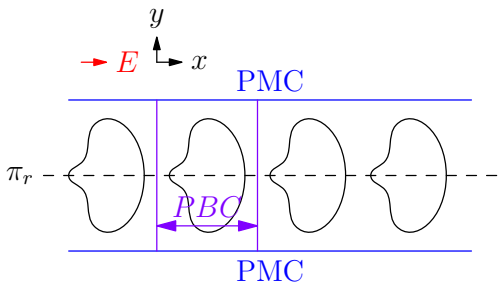

Figure 3.15: A certain structure equipped with PBC and PMC condtions for a x-axis oriented E-field excitation

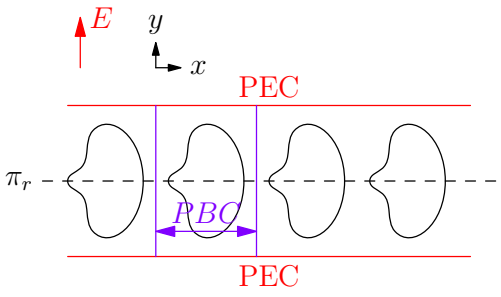

Figure 3.16: A certain structure equipped with PBC and PEC condtions for a y-axis oriented E-field excitation

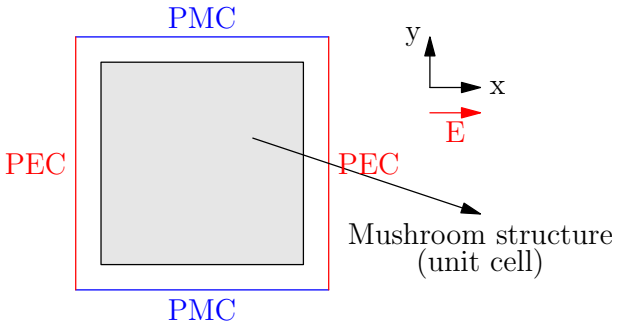

Figure 3.17: PEC-PMC conditions applying on a unit cell of Mushroom structure, with excitation of E-field along the x-axis

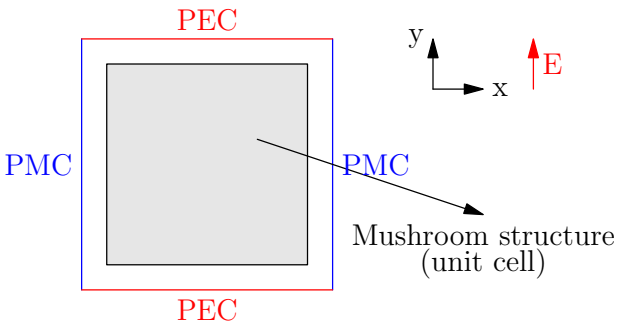

Figure 3.18: PEC-PMC conditions applying on a unit cell of Mushroom structure, with excitation of E-field along the y-axis

Verification

The equivalence of these two combinations of different boundary conditions has already been theoretically proved. Now we will check it from numerical calculations.

Suppose we have an empty cubic study box with a ground plane on the bottom surface and illuminated by an E-field excitation on the top surface. We compare the E-field in the study domain by using these two combinations of boundary conditions. Analytical results will be calculated and be taken as references to judge them. Since the excitation is a constant E-field oriented along the y-axis, we observe only the y-axis component of the E-field.

We carried out two simulations at respectively 10 GHz (as seen in Fig. 3.19) and 20 GHz (as seen in Fig. 3.20) and we compare the E-field along an observation line, orthogonal to the bottom surface. It is observed that the results with the PEC/PMC conditions coincide with the ones with the PBC.

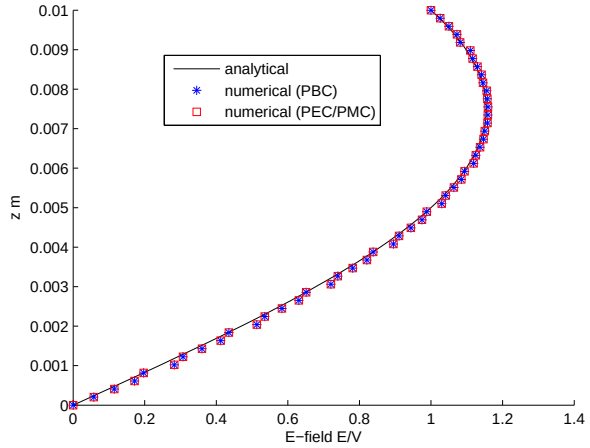

Figure 3.19: frequency = 10GHz

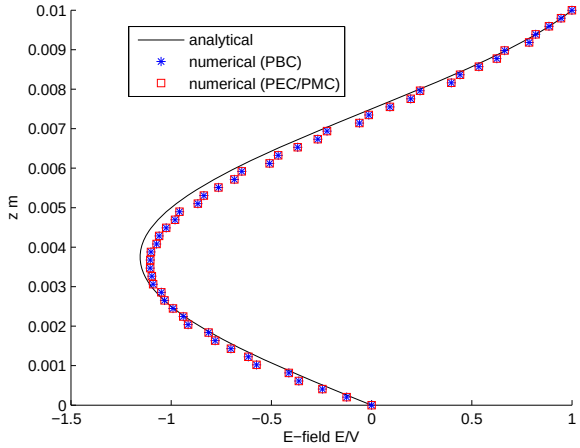

Figure 3.20: frequency = 20GHz

Analysis

In the previous part, we demonstrated that these two boundary combinations are valid and equivalent when modeling symmetric HIS structures. But discretization introduces a finite-element mesh that should also respect the same symmetries. Otherwise, this equivalence might be broken.

Reconsider the empty box model again, and mesh the domain in two ways: symmetric and asymmetric with respect to two middle planes, (Fig. 3.21).

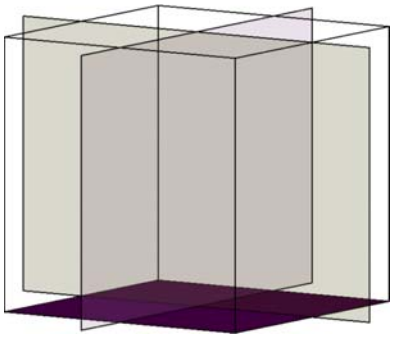

Figure 3.21: The reference planes for symmetric meshing

Just as before, we calculate the E-field on an observation line orthogonal to the bottom surface by using two different combinations of boundary conditions. The results obtained with a symmetric mesh are shown in Fig. 3.22 and the ones with a non-symmetric mesh are shown in Fig. 3.23. The analytical results are still taken as reference and it is observed that the lack of symmetry does have an impact on the accuracy in case of using PEC/PMC conditions.

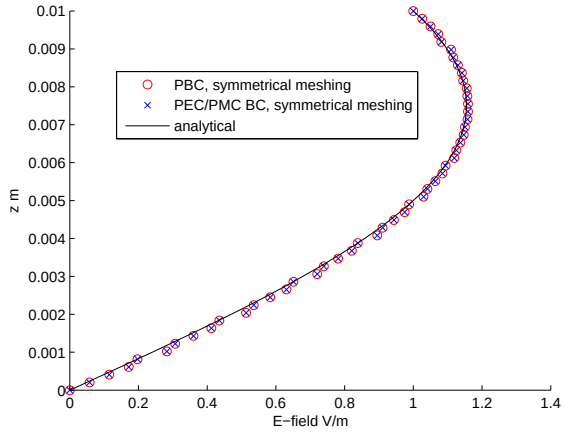

Figure 3.22: Comparison of E-fields with symmetric meshing

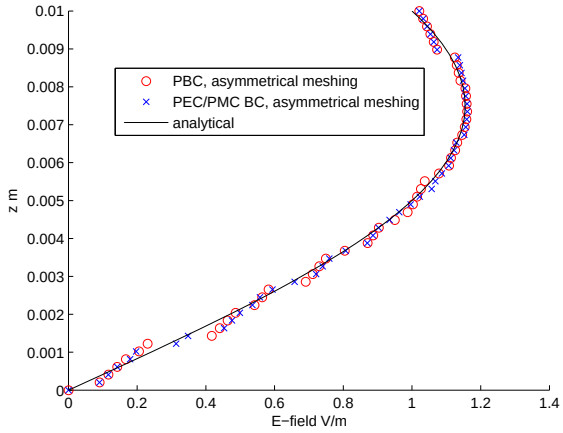

Figure 3.23: Comparison of E-field with asymmetric meshing

We also carried out another numerical simulation by adding a big patch into the study domain, which is closer to the modeling with a real HIS structures. Since we choose tetrahedral elements, it is more difficult to get a totally symmetric mesh in presence of a patch. This time the study domain is meshed in two ways: one almost symmetric and the other one asymmetric.

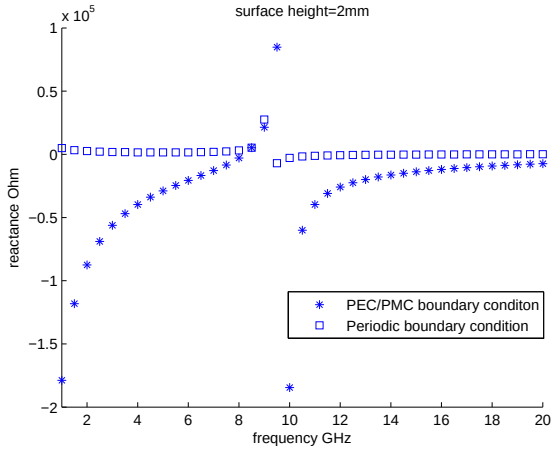

Figure 3.24: One model of a box with big patch inside and an almost symmetric meshing

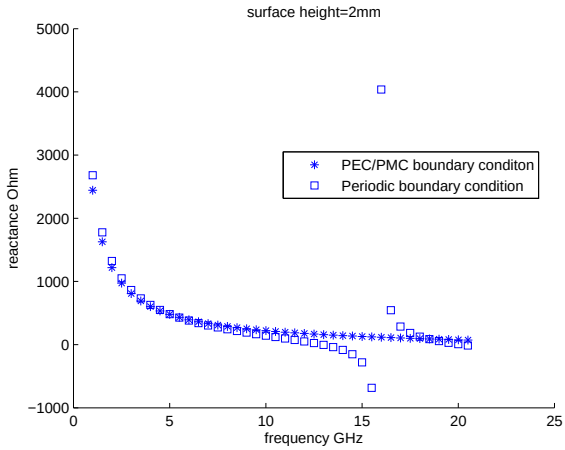

Figure 3.25: One model of a box with big patch inside and a meshing less symmetric

In the case of a symmetric mesh, the model with PEC/PMC conditions predicts a resonance a little bit higher than the one obtained from the model with PBC. This phenomenon of a small resonance shift can be understood through a theoretical analysis, as follows.

The PEC condition imposes all edge circulations of the tangential electrical field on the boundary surface to be zero, which is not necessarily the case for a PBC. This means the PEC condition imposes more constraints on the discrete solution than PBC. The PMC condition, regarded as a "Neumann" condition, is naturally satisfied, which means the PBC condition imposes more constraints on the boundary surface than the PMC condition. In our simulations, the E-field excitation always has a non-zero component parallel to the PMC surface, and a zero component parallel to the PEC surface. Thus, the influence of the PMC condition can be neglected and we may only compare the PBC and the PEC condition.

When applying the PEC condition to the model, its lowest nonzero eigenvalue λ_{PEC} (that is to say, the square of the first resonance frequency), is given by the Rayleigh quotient:

$$\lambda_{PEC} = \min\left\{\frac{Ax \cdot x}{|x|^2},\ x \in X_{PEC}\, x \neq 0\right\}, \tag{3.6}$$

where A is the system's stiffness matrix and X_{PEC} the set of all possible DOF arrays satisfying the discrete form of the PEC condition.

When applying the PBC to the model, its eigenvalues λ_{PBC} are:

$$\lambda_{PBC} = \min\left\{\frac{Ax \cdot x}{|x|^2},\ x \in X_{PBC}\, x \neq 0\right\}. \tag{3.7}$$

where X_{PBC} is the set of all possible DOF arrays satisfying the discrete form of the PBC condition.

Fewer constraints means a wider choice for the eigenvalues,

$$X_{PEC} \subset X_{PBC}, \tag{3.8}$$

hence a smaller eigenvalue will be obtained:

$$\lambda_{PEC} > \lambda_{PBC}. \tag{3.9}$$

In our modeling, we calculate the first principal resonance corresponding to the HIS structures and we just see that the eigenvalue calculated with PEC conditions should be higher than the one with PBC. So, it is normal to observe a higher resonance with PEC-PMC combination than the one with PBC in Fig. 3.24.

In the condition with an asymmetric meshing, the results obtained from the model with PEC-PMC conditions are totally different from the model with PBC conditions, as seen in Fig. 3.25. Thus, the impact of the asymmetric meshing is so big that the difference cannot be totally

explained by what precedes.

To conclude: For a symmetric HIS structure, one can apply the PEC-PMC conditions with the benefit of a simpler coding and a reduced computing time. However, this choice of boundary conditions is not recommended unless a totally symmetric mesh can be guaranteed.

3.2 Asymmetric HIS structures

The general aim of our study is to use HIS as ground planes for antennas. They should act as good reflectors, hence the search for a high impedance. When looking for the radiation pattern of such a device, we need the surface admittance to set up an impedance boundary condition on the ground plane. This calculation can be performed by solving the Maxwell equations in the basic box, with suitable boundary conditions, with a uniform horizontal E-field applied at the top.

Let's first define admittance with enough generality for our purpose. Let D be a domain of space enclosed by a surface S and suppose all sources for the field lie outside D. We define the admittance of the surface S (or more rigorously, the "admittance of region D as seen from its surface S") as the boundary operator Y_S such that

$$n \times H \mid_S = Y_S E_S, \tag{3.10}$$

where E_S and H_S are the tangential components of E and H on S. One may find Y_S by solving Maxwell's equations inside D, with E_S given on S.

Then, knowing Y_S allows one to solve Maxwell's equation outside D by using the so-called impedance boundary condition:

$$(n \times H)_S + Y_S E_S = 0 \, on \, S. \tag{3.11}$$

The change of sign is due to the convention about the direction of the normal, always outwards with respect to the computational domain, which is D in (3.10) and the complement of D in (3.11).

When the components of HIS stuctures are much smaller than the wavelength of the operating frequency, the E-field on the surface S is considered as quasi-uniform. Under this circumstance, one can take as admittance of the observation surface an average value Y_S defined by the relation between the average E-field and the average H-field on the surface. Then Y_S takes the form of a 2×2 matrix. The impedance Z_S is then the inverse of Y_S, easily calculated.

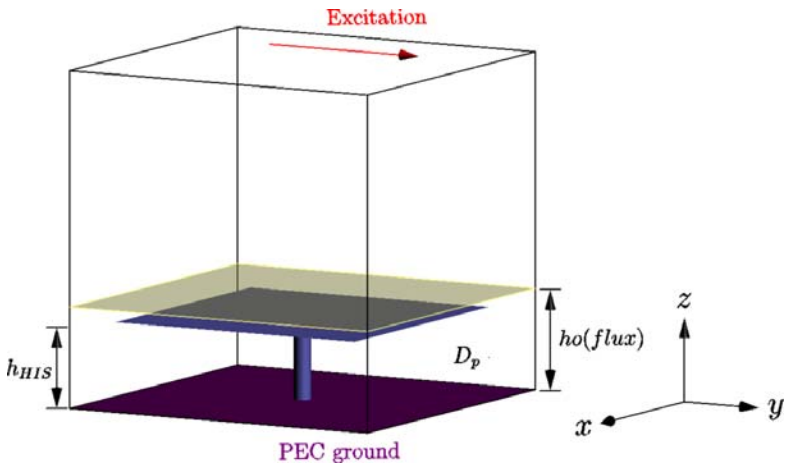

Figure 3.26: Illustration of the study domain for the Poynting flux method

In previous section, we computed the surface impedance Z_S for rotationally symmetric HIS structures. For these particular structures, the surface impedance matrix is diagonal and its two diagonal entries are identical. Because of this symmetry, the calculation of a matrix with four unknown entries is reduced to one with a single unknown matrix entry. This unknown value can be obtained by resolving one equation with one excitation. However, for an asymmetric HIS structure, the surface impedance matrix is no longer symmetric. The characteristics of HIS structures should be retrieved from all the four unknown matrix entries, which means more equations are required and more excitations are needed.

In this section, we will first introduce two new numerical methods to calculate the 2D surface impedance Z_S for HIS structures. Then, these two methods will be validated by two symmetric HIS structures. Finally, these methods will be applied to those asymmetric HIS structures as well.

3.2.1 Numerical Methods for 2D Surface Impedances

Poynting Flux Method

The study domain is a cubic box, composed of one unit cell of the HIS structure, as shown in Fig. 3.26. What we call here the "Poynting Flux method" is a post data-processing method based on FEM using edge elements. The first step when putting this method into use consists in calculating the circulations of the E-field on all mesh edges of the study domain, in presence of an excitation E-field imposed on the top surface.

We aim at calculating the surface impedance on the observation surface at $ho(flux)$, which

is higher than the height h_{HIS} of the HIS elements. When using the Poynting Flux Method, the real study domain is reduced to the domain below the observation surface. Since there is no source in this domain, it is considered as a passive domain, denoted as D_p. Now, S denotes the whole boundary of D_p, composed of six sub-surfaces, as shown in Fig. 3.27. The S in can be symbolically written as $S = S_1 + \cdots + S_6$.

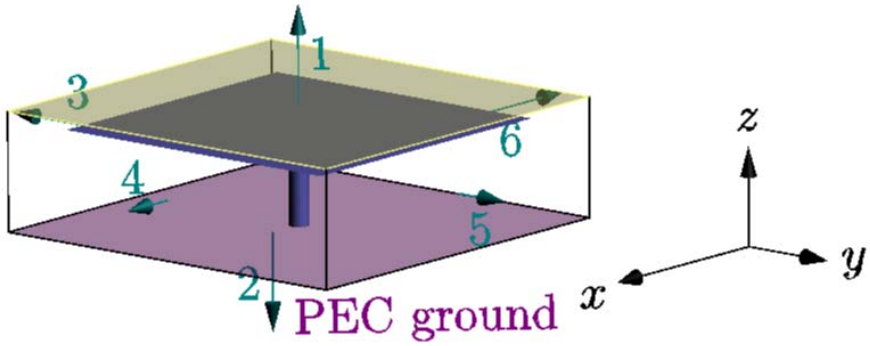

Figure 3.27: Subsurfaces covering the passive domain

After several standard mathematical manipulations of the Maxwell equations, and by using the divergence theorem, one finds that the following equation holds in domain D_p:

$$\int_{D_p} (i\omega\varepsilon E \cdot E + i\omega\mu H \cdot H) = \int_S (n \times H_S) \cdot E_S. \tag{3.12}$$

Since the bottom surface S_2 bears a PEC condition, the surface integral on S_2 in Eq. 3.12 is null. Next, no matter which combination of boundary conditions we choose (the PBC combination or the PEC-PMC combination), the surface integral in Eq. 3.12 on the set-union of surface 3 to 6 will be null too. Therefore, S_1 is the only effective part of surface S. In what follows, S will stand for S_1.

Substituting the impedance boundary condition (Eq. 3.11) into the surface integral of Eq. 3.12, we obtain:

$$i\omega \int_{D_p} (\varepsilon E \cdot E + \mu H \cdot H) = \int_S (Y_S E_S) \cdot E_S, \tag{3.13}$$

where Y_S is a general operator representing the surface admittance at $ho(flux)$.

The surface admittance Y_S is a 2×2 matrix with four unknown entries, which requires four different equations to be determined. Let us consider two different excitation vectors, E^1_{ex} (parallel to the x-axis) and E^2_{ex} (parallel to the y-axis). In each case, we get the corresponding fields E^1, H^1 and E^2, H^2 in the whole domain. Then, a combination of these two cases allows us to derive the equation 3.13 in four different cases as:

$$i\omega \int_{D_p} (\varepsilon E^i \cdot E^j + \mu H^j H^i) + \int_S (Y_0 E_S^i) \cdot E_S^i = 0 \, (i, j = 1, 2). \tag{3.14}$$

The first term of 3.14 has the physical dimension of a power in the study domain, and the second term interpreted as a flux of energy out of the covering surface. Calculating surface impedance this way amounts to computing the flux travelling through the observation surface, and that's why it is called the Poynting flux method.

Resolving Eq. 3.14 is the crucial issue for this method and we get a further look at this equation. Under the hypothesis that the fields E and H on the surface at $ho(flux)$ are approximately uniform, Y_S and E_S can be expressed as matrices with average values. For this case, the equation 3.14 can be written as

$$\int_D (i\omega\varepsilon E^i \cdot E^j + i\omega\mu H^j \cdot H^i) = Area(S) \left\langle E_S^j \right\rangle^t Y_{ij} \left\langle E_S^i \right\rangle \, (i, j = 1, 2). \tag{3.15}$$

The symbol $\langle\rangle$ means the average values and the symbol t denotes the transpose of a matrix.

We denote the left-hand side of the equation 3.15 as P_{ij} and rewrite 3.15 as

$$P_{11} = \int_D (i\omega\varepsilon E^1 \cdot E^1 + i\omega\mu H^1 \cdot H^1) = -Area(S) \left\langle E_S^1 \right\rangle^t Y \left\langle E_S^1 \right\rangle. \tag{3.16}$$

$$P_{12} = \int_D (i\omega\varepsilon E^1 \cdot E^2 + i\omega\mu H^2 \cdot H^1) = -Area(S) \left\langle E_S^2 \right\rangle^t Y \left\langle E_S^1 \right\rangle. \tag{3.17}$$

$$P_{21} = \int_D (i\omega\varepsilon E^2 \cdot E^1 + i\omega\mu H^1 \cdot H^2) = -Area(S) \left\langle E_S^1 \right\rangle^t Y \left\langle E_S^2 \right\rangle. \tag{3.18}$$

$$P_{22} = \int_D (i\omega\varepsilon E^2 \cdot E^2 + i\omega\mu H^2 \cdot H^2) = -Area(S) \left\langle E_S^2 \right\rangle^t Y \left\langle E_S^2 \right\rangle. \tag{3.19}$$

Now, let us look at the right hand side of equation 3.15. In our case, the E-field is represented by a column vector with two complex components, one for the x-coordinate and one for the y-coordinate, so this can be written as follows in the case of $i, j = 1$:

$$\left\langle E_S^1 \right\rangle^t Y \left\langle E_S^1 \right\rangle = \begin{bmatrix} E_{Sx}^1 & E_{sy}^1 \end{bmatrix} \begin{bmatrix} Y_{11} & Y_{12} \\ Y_{21} & Y_{22} \end{bmatrix} \begin{bmatrix} E_{Sx}^1 \\ E_{sy}^1 \end{bmatrix}. \tag{3.20}$$

Expanding the right-hand side of 3.20 and proceeding the same way with the other three cases, we have 3.15 in matrix form as:

$$-\frac{1}{Area(S)}\begin{bmatrix} P_{11} \\ P_{12} \\ P_{21} \\ P_{22} \end{bmatrix} = \begin{bmatrix} (E^1_{Sx}\cdot E^1_{Sx}) & (E^1_{Sy}\cdot E^1_{Sx}) & (E^1_{Sx}\cdot E^1_{Sy}) & (E^1_{Sy}\cdot E^1_{Sy}) \\ (E^2_{Sx}\cdot E^1_{Sx}) & (E^2_{Sy}\cdot E^1_{Sx}) & (E^2_{Sx}\cdot E^1_{Sy}) & (E^2_{Sy}\cdot E^1_{Sy}) \\ (E^1_{Sx}\cdot E^2_{Sx}) & (E^1_{Sy}\cdot E^2_{Sx}) & (E^1_{Sx}\cdot E^2_{Sy}) & (E^1_{Sy}\cdot E^2_{Sy}) \\ (E^2_{Sx}\cdot E^2_{Sx}) & (E^2_{Sy}\cdot E^2_{Sx}) & (E^2_{Sx}\cdot E^2_{Sy}) & (E^2_{Sy}\cdot E^2_{Sy}) \end{bmatrix} \cdot \begin{bmatrix} Y_{11} \\ Y_{12} \\ Y_{21} \\ Y_{22} \end{bmatrix} \quad (3.21)$$

Once the admittance matrix Y is obtained, the desired surface impedance matrix Z_S comes easily by inverting Y.

$\langle E\rangle$ / $\langle H\rangle$ method

Different from the Poynting flux method, this method requires results about the average tangential electromagnetic fields on the observation surface only, hence we call it the <E>/<H> method.

Consider again the cubic study domain corresponding to a unit cell of HIS structures, as seen in Fig. 3.28. Before calculating the surface impedance by the $\langle E\rangle$ / $\langle H\rangle$ method, the circulations of the E-field along all edges of the mesh should be calculated and stored.

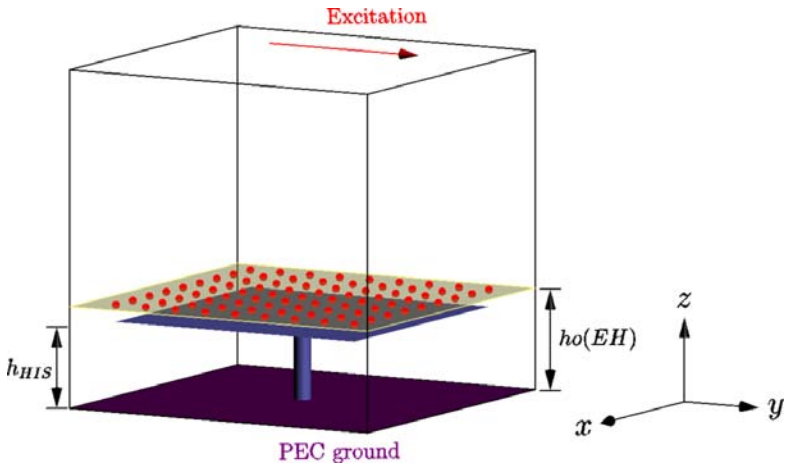

Figure 3.28: Illustration of the study domain with the <E>/<H> method

The surface impedance Z_S is directly defined as the ratio of the average tangential electric field over the tangential magnetic field on the observation surface:

$$Z_S = \frac{\langle E_t\rangle}{\langle H_t\rangle}, \quad (3.22)$$

where the symbol t means the tangential component on the observation surface at $z = ho(EH)$,

superior to h_{HIS}. In order to calculate these average values, we'll first calculate the E-field and H-field at $N \times N$ grid points on the observation surface (as seen in Fig. 3.28) and then get the average value of them all.

Suppose the observation surface is contained in the $x - y$ plane, the general admittance matrix of this surface can be written as:

$$Y_S = \begin{bmatrix} Y_{xx} & Y_{xy} \\ Y_{yx} & Y_{yy} \end{bmatrix}, \tag{3.23}$$

where x and y refer to the coordinates and all the entries of the matrix are average values. For instance, we have $Y_{Sxx} = \frac{\langle n \times H \rangle |_x}{\langle E_x \rangle}$.

The impedance boundary condition of this observation surface can be presented in matrix form as:

$$\begin{bmatrix} \langle n \times H \rangle |_x \\ \langle n \times H \rangle |_y \end{bmatrix} + \begin{bmatrix} Y_{xx} & Y_{xy} \\ Y_{yx} & Y_{yy} \end{bmatrix} \begin{bmatrix} \langle E_x \rangle \\ \langle E_y \rangle \end{bmatrix} = 0. \tag{3.24}$$

We have the precondition that the field on the observation surface is quasi-uniform. Same as before, two orthogonal incident fields are respectively taken as excitation fields, so as to resolve a 2×2 matrix. After obtaining the average tangential electromagnetic fields on the surfaces, the surface admittance matrix can be obtained by:

$$\begin{bmatrix} -H_y^1 & -H_y^2 \\ H_x^1 & H_x^2 \end{bmatrix} = - \begin{bmatrix} Y_{xx} & Y_{xy} \\ Y_{yx} & Y_{yy} \end{bmatrix} \cdot \begin{bmatrix} E_x^1 & E_x^2 \\ E_y^1 & E_y^2 \end{bmatrix}. \tag{3.25}$$

3.2.2 Simulations

In Section 3.1, we proposed a numerical model to calculate the surface impedance of two symmetric HIS structures: the Mushroom structure and the Jerusalem-cross structure. Because of their rotational symmetry (in addition to their spatial periodicity), the calculation of the 2×2 surface impedance matrix Z for these structures reduces to the calculation of a single term of Z, namely, Z_{11}. We shall refer to this approach as "the 1D calculation".

In this subsection, we begin by calculating the surface impedance matrix for the symmetric structures by using the two newly proposed numerical methods (the Poynting flux method and the $\langle E \rangle / \langle H \rangle$ method). We refer to these as "the 2D calculations", because they directly calculate the impedance matrix in two dimensions. The recalculation of the same symmetric structures will help us validate these methods by comparing the 2D results with the 1D results. Later, we will apply these methods to the calculation of the surface impedance for asymmetric

HIS structures.

Mushroom Structures

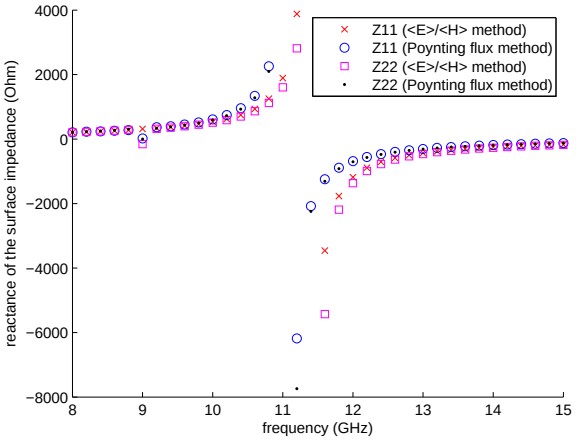

Figure 3.29: 2D calculations of Z_{11} and Z_{22} for a mushroom structure

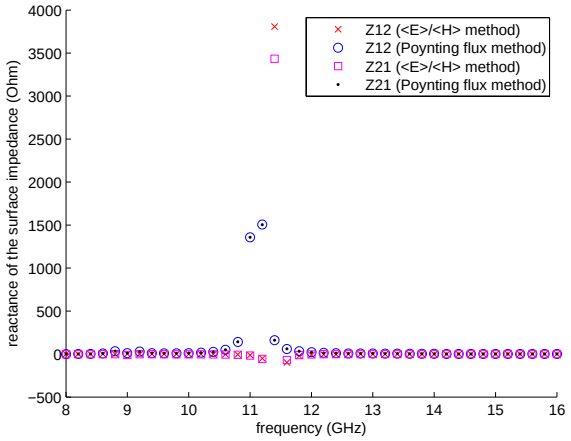

Figure 3.30: 2D calculations of Z_{12} and Z_{21} for a mushroom structure

The Mushroom structure is a fourfold rotationally invariant structure, so the four entries of its surface impedance matrix are: $Z_{11} = Z_{22}$ and $Z_{12} = Z_{21} = 0$. Besides that, when the substrate is lossless, the real part of the surface impedance is null. Hence, we only analyze the imaginary part of the surface impedance.

Figure 3.29 presents the 2D calculations of Z_{11} and Z_{22}. It is observed that Z_{11} is almost equal to Z_{22} for both numerical methods. In the vicinity of the resonance, the results are in less good accordance. Figure 3.30 presents the calculations of Z_{12} and Z_{21}. It can be observed that Z_{12} and Z_{21} are null, except around the resonance.

In comparison to the theoretical prediction, the numerical values are less effective around the region of the resonance. One may blame this on the poor condition number of the system matrix near the resonance, and this will be addressed in detail in the next section. Additionally, it is found that the Poynting flux method predicts a resonant frequency a little lower than the one predicted by the $\langle E \rangle / \langle H \rangle$ method.

In previous work, the 1D calculations for the Mushroom structure have already been validated, here we recalculate the surface impedance of the same structure by using the two proposed numerical methods. Figure 3.31 presents a comparison of Z_{11} among one 1D calculation and two 2D calculations. It is shown that the 2D calculations are in good agreement with the

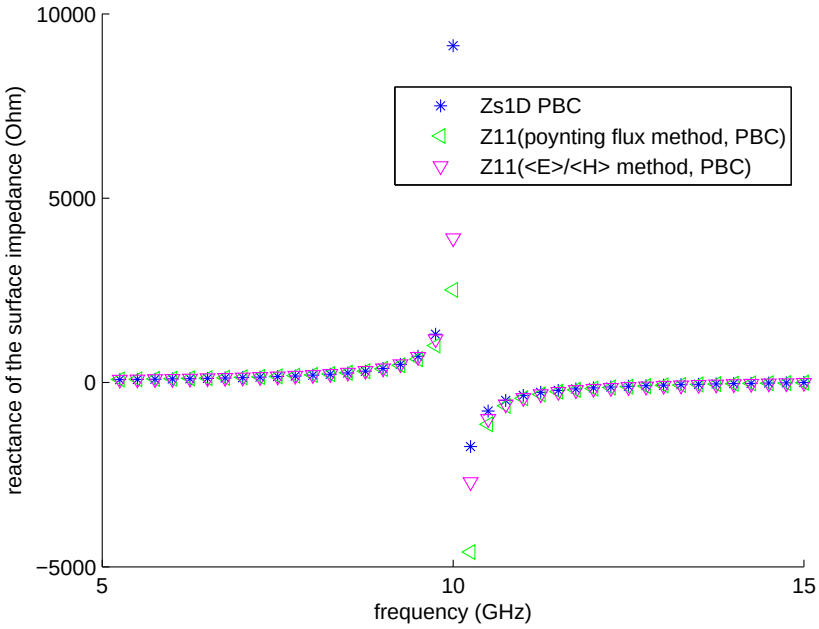

Figure 3.31: Comparison of Z_{11} between the 1D calculations and the 2D calculations

1D calculations, which demonstrates that both of the new proposed numerical methods are workable.

Jerusalem-cross Structures

Jerusalem-cross structure is another symmetric structure intensively investigated in this thesis. We also operate simulations to calculate the surface impedance of this structure.

Figure 3.32 represents the results for Z_{11} and Z_{22} for a JC structure and Figure 3.33 represents the ones for Z_{12} and Z_{21}. These results verify the announced properties for rotationally symmetric HIS structures: $Z_{11} = Z_{22}$ and $Z_{12} = Z_{21} = 0$, which confirm again the effectiveness of our two numerical methods.

In all cases above, the substrates are lossless. Next, we consider the case with a JC structure and a lossy substrate ($\varepsilon_r = 2.2 - j0.001$). Figure 3.34 and Figure 3.35 present the comparison of the surface impedance for a JC structure with and without a lossy substrate. Figure 3.34 clearly shows that the real part of Z_{11} is no more null when the substrate is lossy. Additionally, it is observed that the lossy substrate displaces a little the resonance to higher frequencies, compared to the lossless substrate.

Up to now, we tested our two numerical methods on the Mushroom structure and the JC

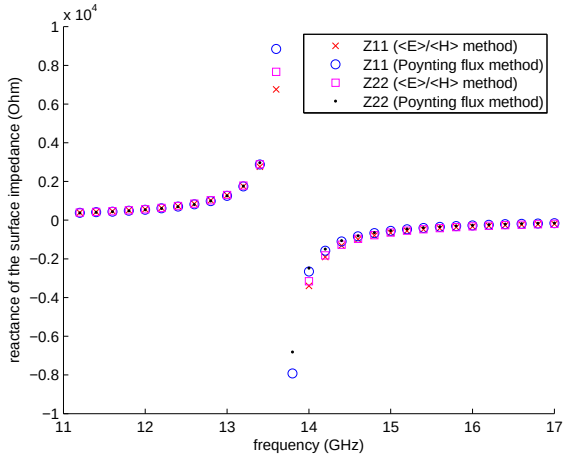

Figure 3.32: 2D calculations of Z_{11} and Z_{22} for a JC structure

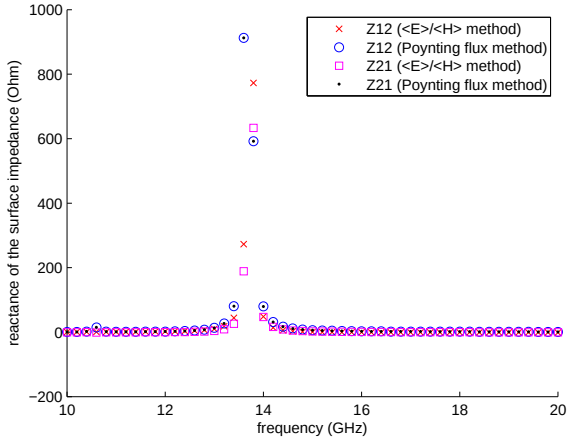

Figure 3.33: 2D calculations of Z_{12} and Z_{21} for a JC structure

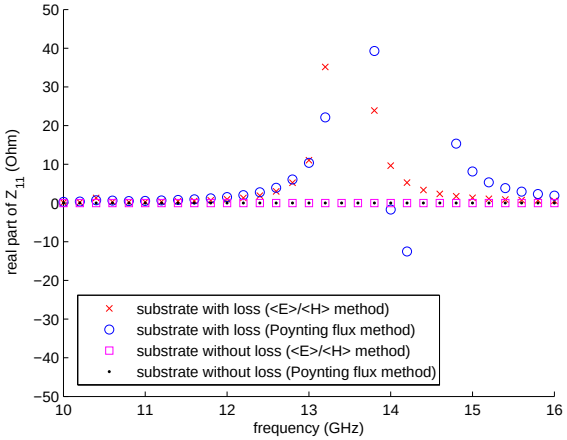

Figure 3.34: real part of Z_{11} for JC structure with or without a lossy substrate

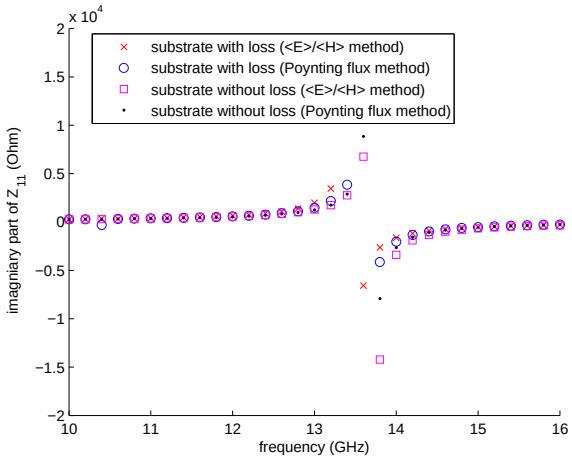

Figure 3.35: imaginary part of Z_{11} for JC structure with or without a lossy substrate

structure. The results show that both methods are able to calculate the surface impedance for symmetric HIS structures. In the following part, we will apply them to asymmetric HIS structures.

Rectangle HIS Structure

For the fourfold rotationally symmetric HIS structures, the surface impedance is independent of the polarization of the incident wave. (Horizontal polarization means that the E-field excitation is oriented along the x-axis; vertical polarization means that it is oriented along the y-axis.) Take

the Mushroom structure as an example and suppose its geometry has a symmetric expansion along the x-axis and along the y-axis. The term Z_{11} of the surface impedance, which corresponds to the impedance reaction of the HIS structure along the x-axis, should be equal to the term Z_{22}, which corresponds to the impedance reaction along the y-axis. For such symmetric HIS structures, we won't care about the polarization of the excitation, since in both cases, they offer the same results. But if this symmetry doesn't hold, the polarization of the excitation should be specified.

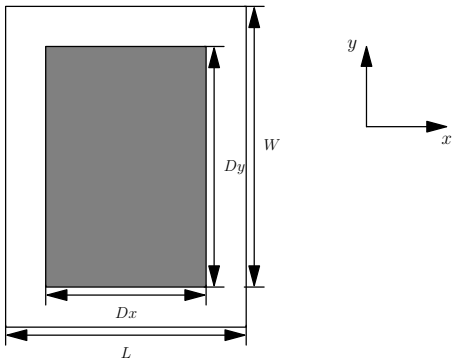

Figure 3.36: unit cell of rectangle HIS structure (top view)

The first asymmetric HIS structure to be investigated is similar to the mushroom structure, but with a rectangle patch on its top surface. Figure 3.36 illustrates the geometry of a unit cell of the rectangular HIS structures with a top view. Its period along the x-axis and the one along the y-axis are respectively denoted as W and L. The patch has a length Dx along the x-axis and a length Dy along the y-axis.

The geometric dimensions of this structure in the simulation are taken as: $Dx = 4$ mm, $Dy = 6$ mm, $W = 7$ mm, $L = 9$mm, $h = 1.6$ mm. Results calculated by the CST software are also added on these two figures, to serve as references. Figure 3.37 and Figure 3.38 plot the phase of the reflection coefficient corresponding respectively to an horizontally-polarized E-field excitation and a vertically-polarized E-field excitation.

When the incident plane wave is horizontally polarized, the patch length Dx has a dominant effect. In this case, one observes a resonant frequency at about 12 GHz. When the incident plane wave is vertically polarized, the patch width Dy plays an important role. The resonant frequency for such an excitation is observed at about 10 GHz. This resonance shift to a lower frequency results from the wider width. So the rectangle HIS structure can work at two different operating frequencies, corresponding to two differently polarized plane waves. Because of this property, a potential application of this kind of HIS structures is to be applied in an antenna

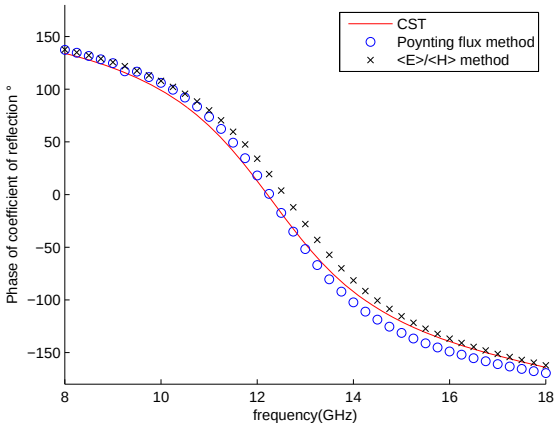

Figure 3.37: Phase of the reflection coefficient for the rectangle HIS structure with a horizonally-polarized

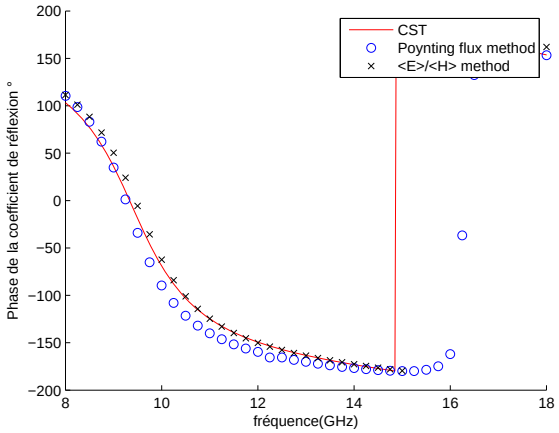

Figure 3.38: Phase of the reflection coefficient for the rectangle HIS structure with a vertically-polarized

system with two different polarization.

Fork-like HIS Structure

In [36], the authors proposed a fork-like HIS structure, the top view of which is illustrated in detail in Fig. 3.39. In the same paper, the authors carried out a comparison between the fork-like structure and the conventional mushroom-like structure. Both simulations and experimental results have verified that an about 40% size reduction could be achieved by using the former structures rather than the latter one, for a similar frequency bandgap. Here, we examine this structure by using our numerical methods so as to investigate the effectiveness of these methods.

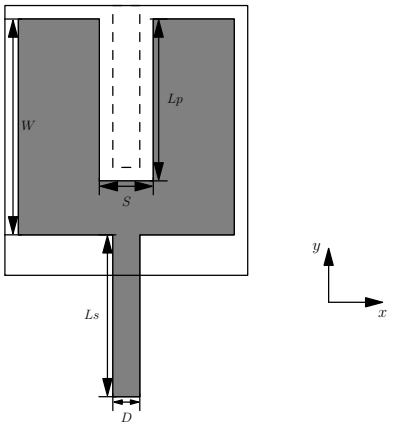

Figure 3.39: Unit cell of fork-like HIS structure (top view)

The geometric dimensions of this structure in the following simulation are taken as: $W = 4$ mm, $S = 1$ mm, $D = 1$ mm, $L_P = 3$ mm, $L_S = 3$ mm, $g = 0.5$ mm, $h = 1.6$ mm. The structure is build on a 1.6-mm-thick substrate with $\varepsilon_r = 2.7$.

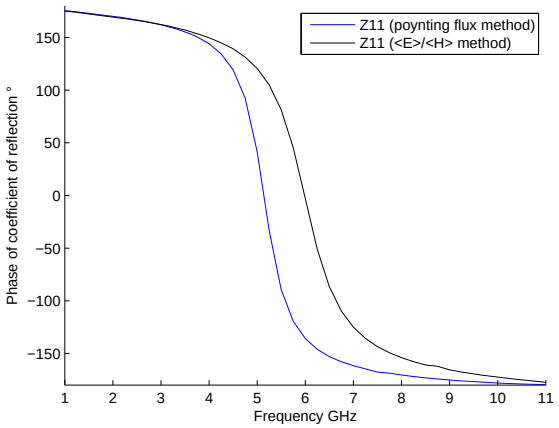

Figure 3.40: Reflection phase of 1-fork HIS structure with a horizonally-polarized

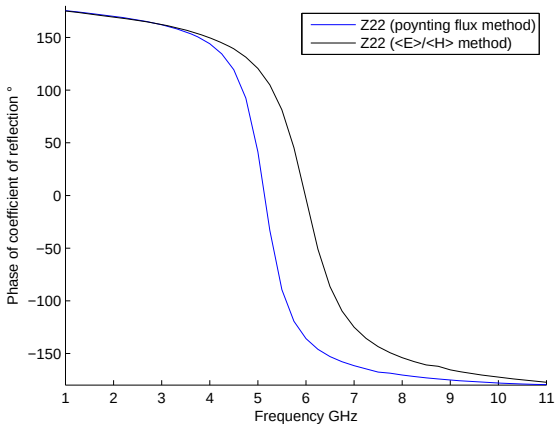

Figure 3.41: Reflection phase of 1-fork HIS structure with a vertically-polarized

Figure 3.40 plots the reflection phase when the incident wave is horizontally polarized. In our simulation, results for this case are calculated by using Z_{11} of the surface matrix. Figure 3.41 plots the reflection phase when the incident wave is vertically polarized. These results are calculated from Z_{22} of the surface matrix.

The measurement results in [36] showed that the resonant frequency is detected at around 4.8 GHz with respect to both polarized excitations. In our simulations, the resonant frequency is identified around 5 GHz with the Poynting flux method and around 6 GHz with the $\langle E \rangle$ / $\langle H \rangle$ method and their frequency band is detcted around 1 GHz. The discrepancy between our numerical results and the experimental results may be related to the presence in the measurement of a microstrip which is not accounted for in the simulations.

4F-like HIS Structure

In [36], the authors also proposed an F-like HIS structure, the top view of which is illustrated in details, as shown in Fig. 3.42. With this structure, an additional capacitance forms between the neighboring edges of the slot and the stretched strip from an adjacent patch. It has been found that the design with this HIS structures could achieve a high size reduction in comparison to the conventional mushroom-like structure, while obtaining a similar frequency bandgap. Moreover,

another interesting observation of this F-like structures was that a second frequency bandgap was noted without tuning the stretched strip length.

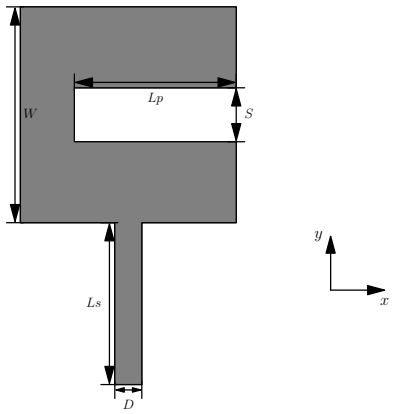

Figure 3.42: Unit cell of F-like HIS structure (top view)

In order to reduce the asymmetric effects, a more isotropic configuration with four F-like structures have been designed. In our simulations, we take the same dimension of the structure as mentioned in this article: $W = 4$ mm, $S = 1$ mm, $D = 1$ mm, $L_P = 3$ mm, $L_S = 3$ mm, $g = 0.5$ mm. The four F-like metal array is build on a 2-mm-thick substrate with $\varepsilon_r = 4.6$.

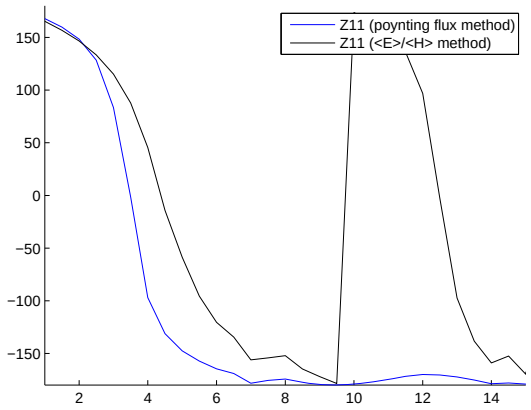

Figure 3.43: Reflection phase of 4F HIS structure

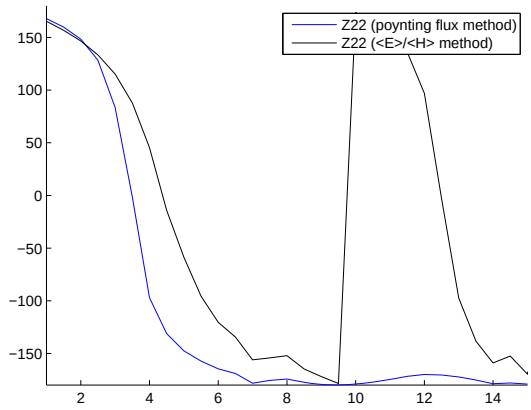

Figure 3.44: Reflection phase of 4F HIS structure

Figure 3.43 and Figure 3.44 plot the reflection coefficient calculated by our numerical methods. One sees that only one resonant frequency is identified, at about 4 GHz, when using the Poynting flux method; two resonant frequencies are identified respectively at around 4.8 GHz and 12.5 GHz. Numerical results presented in [36] showed a first resonance around 3.5 GHz

and a second one around 6.7 GHz, for higher modes. They use the method of moments and we use the finite element method. We find it is difficult to explain these large discrepancies, even though the numerical methods are different.

Spiral-Arm HIS Structure

The results above show that our numerical methods are able to characterize HIS structures, be they symmetrical (by mirror reflection or by rotation) or not. Here, we will apply these methods to one type of HIS structure, based on the inclusion of Hilbert-curve shaped elements. This aims at making the high impedance surface more compact. Hilbert curves are characterized by the "number of iterations" parameter. As this number increases, the equivalent inductance increases, resulting in a lower resonant frequency. Spiral arm HIS structures are designed with this property in mind.

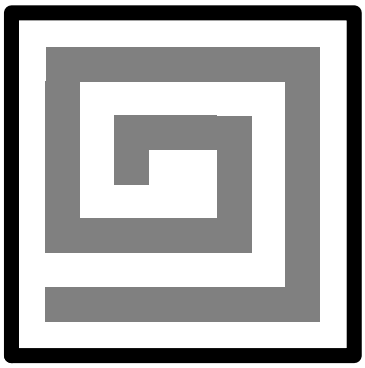

Figure 3.45: HIS planar surface using one spiral arm HIS structure (top view)

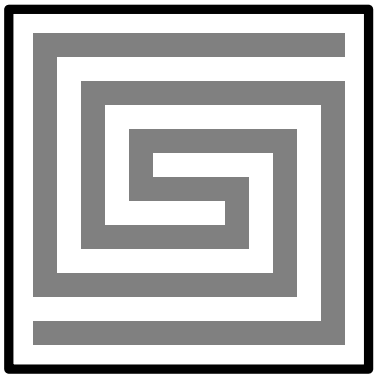

Figure 3.46: HIS planar surface using two spiral arms HIS structure (top view)

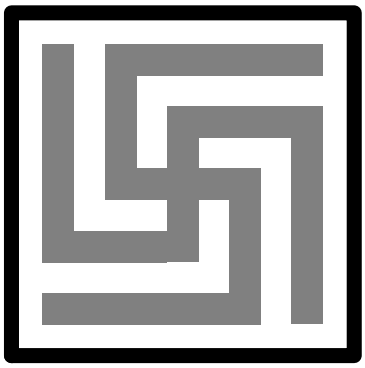

Figure 3.47: HIS planar surface using four spiral arms HIS structure (top view)

We begin the work by a one-single spiral arm HIS, as shown in Fig. 3.45. We calculate the reflection coefficient phases corresponding respectively to a horizontally polarized excitation (as seen in Fig. 3.48) and a vertically polarized excitation (as seen in Fig. 3.49). These two figures show that the design with one spiral-arm structure behaves differently with respect to the horizontal polarization and the vertical polarization. Instead of a big enough bandgap, many narrow bandgaps are found.

The book [110] asserts that if the one-arm spiral HIS structure is too asymmetric, this structure may generate a high level of cross-polarization. From the point of view of an antenna, a cross-polarization means that the radiation is orthogonal to the desired polarization. On the contrary, a co-polarization represents the polarization in which the antenna is intended

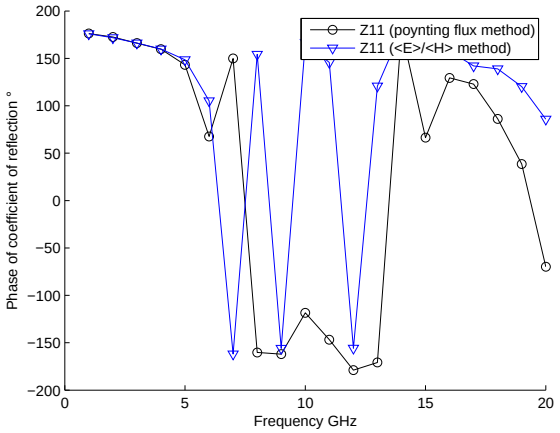

Figure 3.48: Reflection phase of one single spiral arm HIS structure

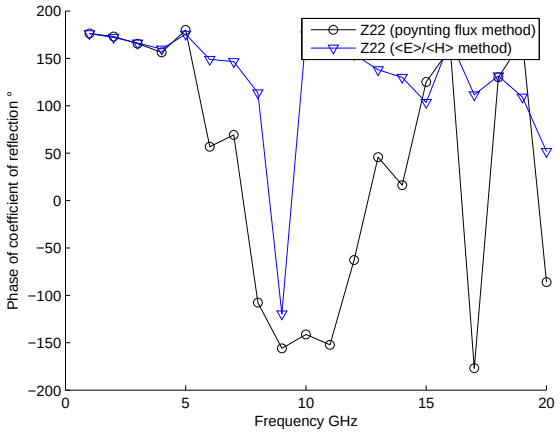

Figure 3.49: Reflection phase of one single spiral arm HIS structure

to radiate. When the antenna is aligned, the goal is to achieve minimum cross-polarization and maximum co-polarization. Using one-arm spiral HIS structures, the horizontal signals will interfere with the vertical signals. Thus, this structure is less recommended for an antenna design.

The same book mentions that the influence of the cross polarization may be reduced by designing a more symmetrical structure. So, we also investigated the performance of a double spiral-arm structure (as seen in Fig. 3.46).

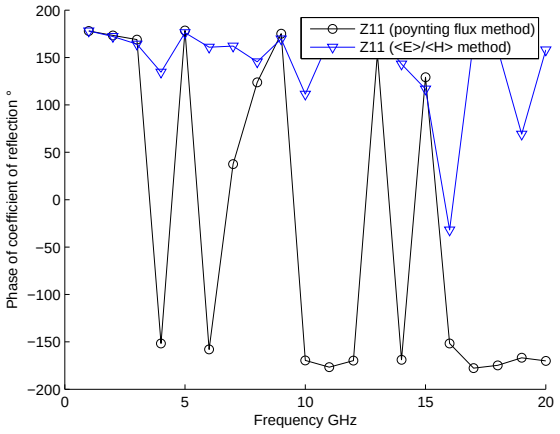

Figure 3.50: Reflection phase of two spiral-arm HIS structure

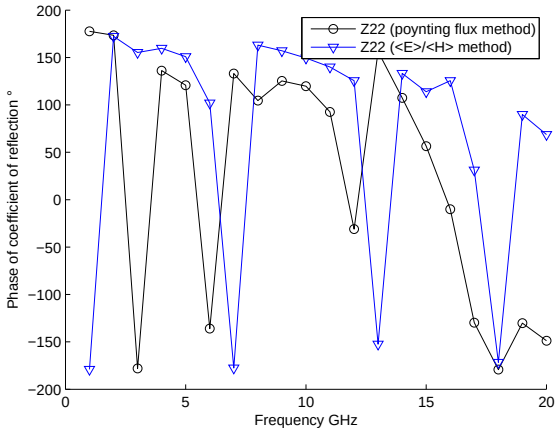

Figure 3.51: Reflection phase of two spiral-arm HIS structure

The phases of the reflection coefficient corresponding to this structure are reported in Fig.

3.50 and Fig. 3.51. It is observed that with a more symmetric structure, the phase of the reflection coefficient still varies dramatically and the influence of the cross-polarization largely exists. In addition, the identified bandgaps are not large enough for an antenna application.

A more symmetric structure can further reduce the cross polarization, so a four-spiral-arm structure is also simulated (seen in Fig. 3.47).

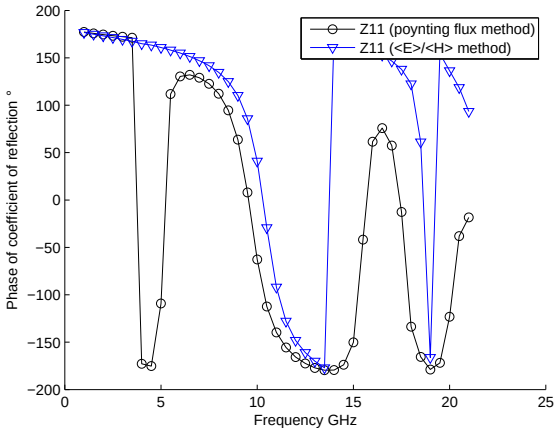

Figure 3.52: Reflection phase of four spiral-arm HIS structure

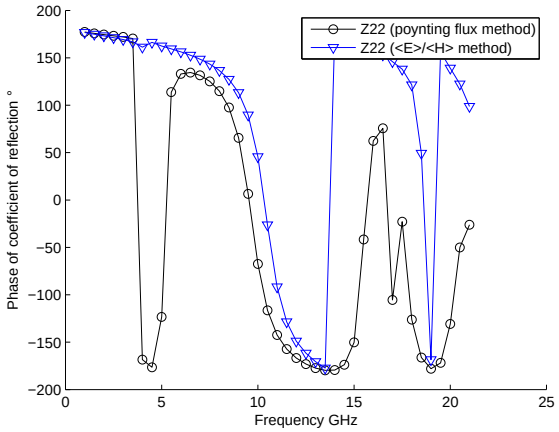

Figure 3.53: Reflection phase of four spiral-arm HIS structure

Since the structure is invariant with respect to a 90° rotation, the values of Z_{11} and Z_{22} should theoretically be the same. Then, it's not astonishing to see that the results in Fig. 3.52 resemble those in Fig. 3.53. From both figures, the first main resonance is identified around 10 GHz, with a bandwidth of about 1 GHz. Another resonance is observed near 17 GHz, with a narrower bandwidth. Moreover, the phase corresponding to the case of a horizontally polarized excitation has the same tendency as the one for a vertically polarized excitation. It seems the bad influence of the cross-polarization has been eliminated. Compared with the one spiral-arm structure and the two spiral-arm structure, this four spiral-arm structure is more promising in antenna designing.

In this part, we carried out a series of simulations studying the spiral-arm HIS structures. The results showed that a more symmetric design, such as four spiral-arm structure, might effectively reduce the bad effects caused by the cross-polarization. We also operated the simulations by adding more spiral arms into the structures. The simulation results show that the structure with more spiral arms may generate more resonances. However, the second, third or higher bandgap were generally narrow, unsuitable for a real application.

3.3 Limitations and trade-offs

Each numerical method has its limits. In this subsection, we examine the limitations and trade-offs of our numerical methods. Some limitations will be related to the properties of FEM itself and the others are associated with the properties of our two methods.

Condition Number

A system of equations is considered to be well-conditioned if a small change in the coefficient matrix or a small change in the right hand side results in a small change of the solution vector. On the contrary, a system of equations is considered to be ill-conditioned if a small change in the coefficient matrix or a small change in the right hand side can result in a large change of the solution vector.

In our HIS studies, the numerical modeling is handled by resolving a linear equation of the form:

$$[A]\,[E] = [b]\,, \tag{3.26}$$

where the matrix $[A]$ represents the stiffness matrix of the whole system, $[E]$ represents the electrical field to be calculated and the column matrix $[b]$ represents the source terms. The condition number associated with this equation gives a bound on how inaccurate the solution $[E]$ can be, in addition to inaccuracies inherent in the discretization. Note that conditioning is a property of the matrix, not of the algorithm or floating point accuracy of the computer used to solve the corresponding system [99].

To simplify the discussion, suppose the values of $[b]$ are exact. The unknown errors in matrix $[A]$ will cause an error in $[E]$. Let δA and δE be the error in $[A]$ and $[E]$. Considering the existing error, the equation 3.26 is modified as:

$$[A + \delta A]\,[E + \delta E] = [b]\,. \tag{3.27}$$

Expanding the equation 3.27,

$$A \cdot E + \delta A \cdot E + A \cdot \delta E + \delta A \cdot \delta E = b. \tag{3.28}$$

Applying the property of norms, that the norm of a product of matrices is bounded by the product of their norms, we have

$\delta A \cdot \delta E$ is negligible and with the help of equation 3.28, we have

$$A \cdot \delta E + \delta A(E + \delta E) \backsimeq 0. \tag{3.29}$$

$$\delta E \simeq -A^{-1} \cdot \delta A \cdot (E + \delta E). \tag{3.30}$$

Applying the property of norms, that the norm of a product of matrices is bounded by the product of their norms, we have

$$\|\delta E\| \leq \left\|A^{-1}\right\| \|\delta A\| \|E + \delta E\|. \tag{3.31}$$

Multiplying both sides by $\|A\|$, we obtain

$$\|A\| \|\delta E\| \leq \|A\| \left\|A^{-1}\right\| \|\delta A\| \|E + \delta E\|. \tag{3.32}$$

$$\frac{\|\delta E\|}{\|E + \delta E\|} \leq \|A\| \left\|A^{-1}\right\| \frac{\|\delta A\|}{\|A\|}. \tag{3.33}$$

This number is named "condition number" of a matrix, where $\lambda_{max}(A)$ and $\lambda_{min}(A)$ are the maximal and minimal eigenvalues of A respectively. The maximum value (for nonzero A and E) is easily seen to be the product of the two operator norms:

$$\kappa(A) = \|A\| \left\|A^{-1}\right\| = \left|\frac{\lambda_{max}(A)}{\lambda_{min}(A)}\right|. \tag{3.34}$$

Our model is designed under the time-harmonic assumption. From the wave equation, we can find a relation between the eigenvalues of A and the operating angular frequency as:

$$\lambda = \mu - \omega^2. \tag{3.35}$$

where, μ represents the eigenvalue for the real solution. When the operating frequency approaches the eigenvalue, a very small λ yields an extremely large condition number. Thus, the ill-conditioning of the matrix will largely influence the accuracy in the region near the resonance.

Preconditioned consists in, instead of solving a system of the form $Ax = b$, solving a system of the form $M^{-1}Ax = M^{-1}b$, where M is the preconditioner. When using an iterative method to solve a linear system of equations, a good choice of preconditioner can have dramatic impact on run-time and robustness. One of the properties of a good preconditioner is that $M^{-1}Ax$ have a small condition number. Therefore, as it is widely recognized, "preconditioning" [100] is a critical ingredient in the development of efficient solvers for challenging problems in computation

science. This method can be used to improve our numerical method too.

Influence of the Mesh

Our simulations are done with the Finite Element Method, with tetrahedral elements. The accuracy of the results depends on the quality and the fineness of the mesh.

These tetrahedra can have very different shapes and dimensions: The region with small variations of the field is meshed with a relatively coarse mesh; the region with stronger variations demands a finer mesh. Some shapes of tetrahedra (too flat ones for instance [103]) may result in a low accuracy and a slow calculation speed. So, these low-quality elements should be avoided when constructing the mesh.

To some extent, the fineness may increase the accuracy of the results. However, pursuing a high accuracy with an extremely fine mesh is not always effective. Therefore, before applying the numerical methods to resolve a real problem, a series of preliminary simulations should be done to decide the mesh type and find a good compromise between accuracy and computing time.

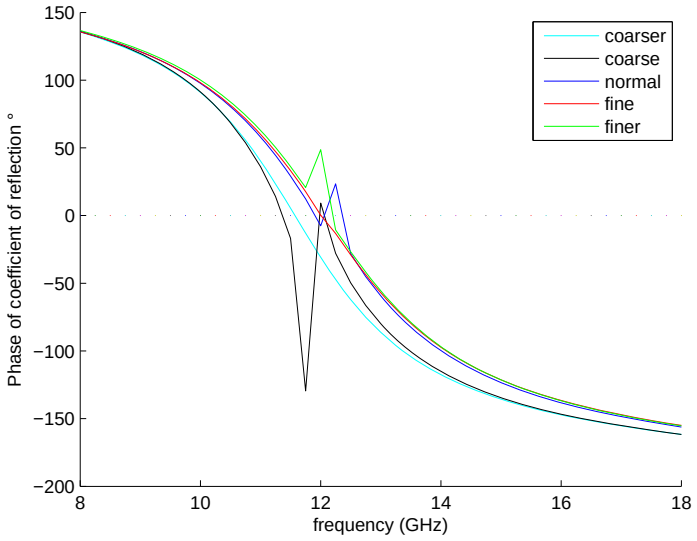

Figure 3.54: Phase of the reflection coefficient for different mesh fitness

Here, we'll give an example of the Mushroom structure to explain the study on mesh fineness. The mesh fineness of the study domain is varied from a relatively coarse case to a relatively fine case as: coarser (4377 elements), coarse (8219 elements), normal (17570 elements), fine (29133) and finer (59617). Their results are shown in Fig. 3.54, in which it can be seen that the finer

the mesh, the higher the resonance will be. The result of a "normal" mesh is close to the one of a "fine" mesh and of a "finer" mesh, which shows a convergence tendency. Hence we adopt this relatively coarse mesh type as "normal", with respect to computing time and accuracy, for later calculation . It is pointed out that several discontinuous points are observed on the figure, which is related to the meshing and the position of observation surface. These abnormal points can be avoided by an appropriate modification of the observation surface.

Influence of other parameters

Operating Frequency

Our numerical method is based on the quasi-static theory where the HIS unit cell's period D should be far smaller than the effective wavelength λ_{eff}. Generally, it is considered that λ_{eff} should be at least 10 times larger than D. However, there is no clear criteria to define the boundary of this ratio. In view of the results, the numerical calculations can be effective even when $\lambda_{eff}/D \approx 7$.

The two new methods proposed for asymmetric HIS structures are based on the same numerical model for symmetric HIS structures. In the numerical simulations for symmetric HIS structures, it was found that the surface impedance values were less effective when the operating frequency was close to the resonance. Here, the two new methods both have this trade-off too, which is mainly due to the poor condition number near the resonance.

Height of Observation Surface

We talked about the calculation of the average surface impedance on an observation surface. We can read the information of the resonance from this impedance value, which largely depends on the height of the observation surface and less depends on the height of the homogeneous E-field excitation.

Both methods proposed in this chapter are based on the premise that the electromagnetic field on the observation surface is quasi-uniform. Generally speaking, the less homogeneous these fields, the less effective the methods will be. This quasi static situation will be broken in two cases: 1) At high frequency, when the dimension of the HIS structures cannot be ignored. This point has already been addressed in the "operating frequency" part. 2) The height of observation surface has not appropriately been chosen. In other words, the effectiveness of this premise depends on the observation's height.

In simulations, the excitation is a constant E-field on the top surface of the study domain,

so on this surface the electric field is totally uniform. At the lower region in the study domain, the electromagnetic fields are no longer uniform, because of the presence of HIS structures. Therefore, if the observation surface is not far away from the source, the electromagnetic fields are quasi-uniform. On the contrary, if the observation surface lies near the HIS structure and far from the source, the hypotheses of "uniform fields" will be less effective. This is not only caused by the attenuation of the distance, but also by the strong near-field reaction from the HIS components.

The height of the observation depends on the purpose of the calculation. Our objective is to create an equivalent model with an homogeneous surface characterized by the surface impedance in an antenna system. The equivalent surface is positioned at the same height as the observation surface h_o. So, the observation surface height h_o cannot be positioned higher than the antenna. Meanwhile, we intend to integrate the HIS structure into a low-profile antenna system. If the equivalent surface is too high, it won't be any help for a compact antenna's design. Therefore, the height of observation surface should be set simultaneously as high as possible to allow the recourse to homogenization theory and as low as possible to be useful as equivalent model for an antenna system.

Moreover, it should be noted that: the higher the observation's height, the more computing time will be sacrificed for the post processing while using the Poynting flux method.

Comparing the Two Methods

In Section 3.2, we introduced two numerical methods to calculate the surface impedance for symmetric or asymmetric HIS structures. Both methods consist in a post-processing of the same data, those provided by the computation of the electric degrees of freedom. Yet, they are not equivalent in terms of computational effort, because the Poynting flux method involves two integrations (one in the volume and one on the surface), whereas the <E>/<H> method requires only one average calculation on the grid of the observation surface.

Which method works better is always a debatable issue in our work. We made a lot of efforts to compare the accuracy of these two methods through different simulations. In what follows, we will explain the accuracy of the two methods associated with a "predfined" observation surface.

In our work, the study domain is meshed in tetrahedra elements via the meshing tool, COMSOL [101]. In this software, when the observation surface is geometrically created in the study domain, the subdomains on two sides of this surface may be separately meshed, but with a common trianglar mesh on this surface. Such a surface we shall call "predefined observation surface" (as shown in Fig. 3.55) in what follows. The alternative would consist in meshing

the whole box without this geometrically defined observation surface. In this case, we have an observation surface cutting through the tetrahedral of the mesh, and we call it as an "artifical observation surface" (as shown in Fig. 3.56).

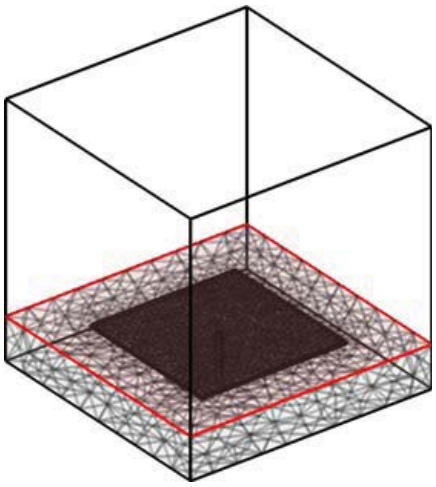

Figure 3.55: A predefined observation surface

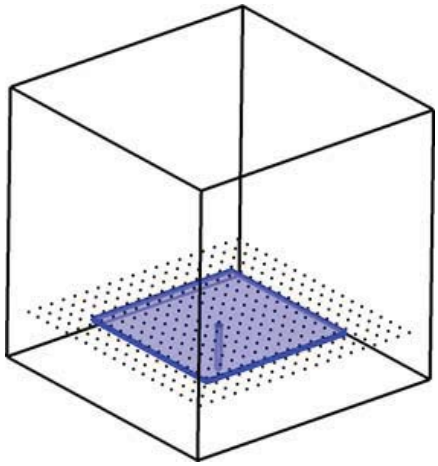

Figure 3.56: An artificial observation surface

When using the Poynting flux method, it is found that a pre-defined observation surface may increase the accuracy of the method. To create this observation surface, the whole study domain is decomposed into two subdomains sharing a common boundary, which is the predefined observation surface. While using the Poynting flux method to calculate the surface impedance for the HIS structures, it concerns a volume integration beneath the observation surface and a surface integration on the observation surface. The former integration requires a precise count of every tetrahedra elements beneath this surface. With the predefined observation surface, the tetrahedra elements belonging to the downside subdomain can be perfectly separated from the ones of the upside subdomain in a numerical processing. The latter integration is associated with the edge elements on the observation surfafce. The predefined observation surface is useful in counting the contribution of all the edge elements on the surface.

While using the $\langle E \rangle / \langle H \rangle$ method to calculate the surface impedance, we firstly calculate the E-field at the observation points, grilled distributed on the observation surface. Then we calculate the H-field from the E-field and get the tangential E- or H-field by their projection on the observation surface. With this method, the observation points should be better chosen at the positions cutting the tetradedra elements. This is because when the observation point lies on the face or an edge of a tetrahedron, only the tangential part of the E-field at this point may be well calculated and the accuracy of the tangential H-field may be influenced. Therefore, the artifical observation surface is preferred in using this method.

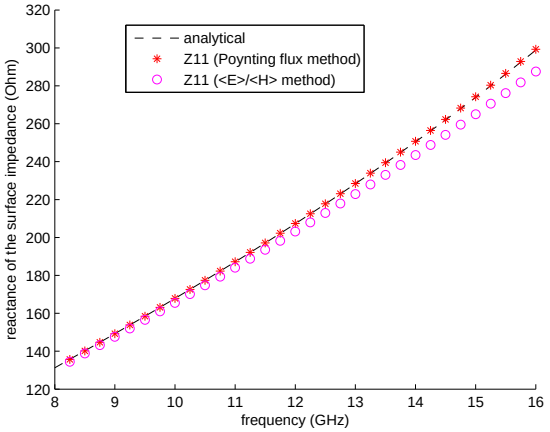

Figure 3.57: With a predefined observation surface

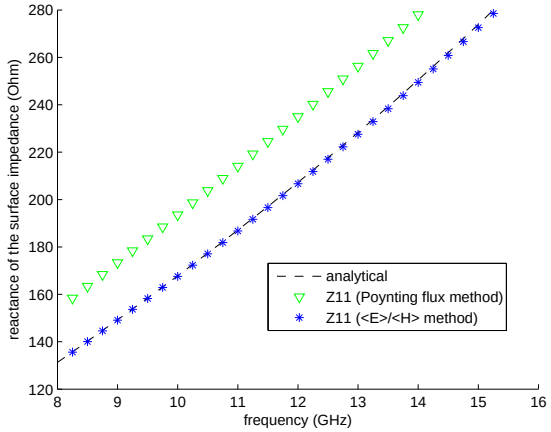

Figure 3.58: With an artificial observation surface

In the following part, we will carry out several simulations to see the influence of the predefined surface. Consider an empty box with dimension of 2 mm x 2 mm x 10 mm, illuminated by a unifrom E-field on the top surface and covered by a perfect electric conductor conductor on the bottom surface.

The surface impedance is calculated at a fixed frequency on the observation surface at $h = 2$ mm by using two different numerical methods and under two different cases: with a predefined observation surface and with an artificial observation surface. Analytical results are also added on the figures as references to judge their accuracies.

In Fig. 3.57, it is observed that the Poynting flux method works better than the $\langle E \rangle / \langle H \rangle$ method. In Fig. 3.58, it is observed that the $\langle E \rangle / \langle H \rangle$ method works better than the Poynting flux method. The results of these simulations confirm that the Poynting flux method requires a geometrically predefined surface and the $\langle E \rangle / \langle H \rangle$ method needs an artifical observation surface.

Chapter 4

Experimental Measurements

In the previous chapter, our two proposed numerical models for calculating the surface impedance of HIS structures have been validated in principle. In this chapter, we check the effectiveness of these models against measurements. Different samples have been fabricated, measured, and these measurements have been compared with numerical results.

4.1 Introduction

Characterization Method

There are different methods to characterize materials, such as the waveguide probe method [104], the resonant cavity method , the coaxial probe method [106]. Since these methods have limits in sample's dimension or in frequency bandwidth, we prefer to use a free space measurement method which is more flexible than those mentioned above.

The working bench is composed of two horn antennas and the sample is placed between them at equal distance, as shown in Fig. 4.1. The dimension of the device is comparable to the wavelength. In free space, the horn antenna emits spherical waves (as seen in Fig. 4.2) and the diffraction is not negligible. More precisely speaking, the emitted beam from the horn antenna is a beam of electromagnetic radiation whose transverse electric field and intensity distributions are well approximated by Gaussian functions, known as Gaussian beams [107].

In order to get a precise characterization using a free space measurement, the amplitude of the wavefront impinging on the sample surface should be uniform. The E-field amplitude of the wavefront at a long distance from the emitted antenna is quasi planar. Unfortunately, the incident power on the sample will be weaker than the one of the parasite signal. To eliminate

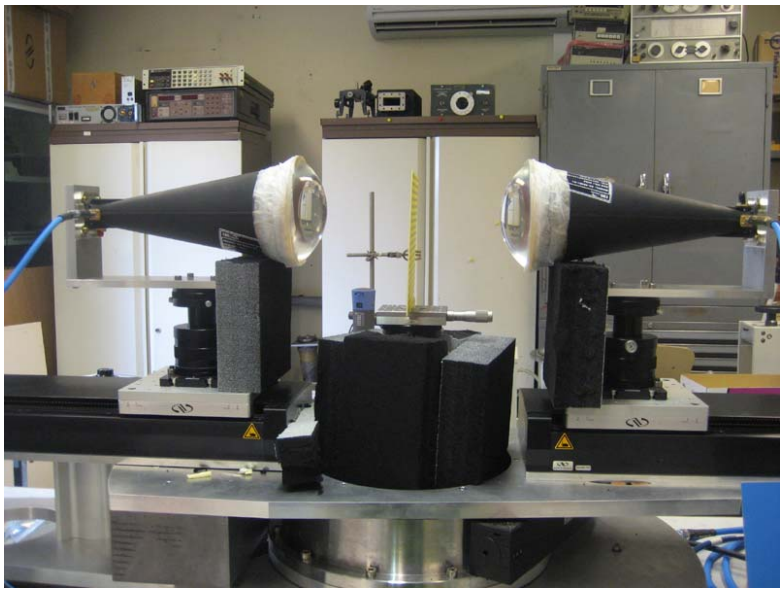

Figure 4.1: Measurement Setup

the perturbed reflected signals, this measurement can be performed in an anechoic chamber, to let the surrounded walls in the chamber absorb parasite signals. An alternative method consist in pasting a lens in front of each horn antennas. These two lenses are added to focus the wave beam and to ensure that a plane wave will impinge on the sample's surface. To reduce financial expenses and measurement space, we selected a focused beam system instead of an operation in an anechoic chamber to characterize our samples. However, this method has the disadvantage that a parasite resonance will appear when the sample's thickness equals half the wavelength.

Experimental Setup

The complete experimental setup consists of a Vectorial Network Analyzer (Agilent, PNA E8364C, 10 MHz - 50 GHz) and two transmit/receive horn antennas (ITT/EDO Corp., AS 48461-01) on the working bench. The two horn antennas operated between 2 GHz and 18 GHz, where the maximum cross polarization is less than -20 dB. The antennas are connected to VNA with flexible and in-phase cables, the connectors of which are APC7 at one side and ADM at another side.

In experiments, the vertically polarized wave is emitted by the horn antenna and the incident electric field is perpendicular to the FSS layer. Figure 4.3 exhibits two photos of our samples: a mushroom sample with vias on the left, a mushroom sample without vias on the right.

During the measurement, the two horn antennas should be precisely aligned and tuned,

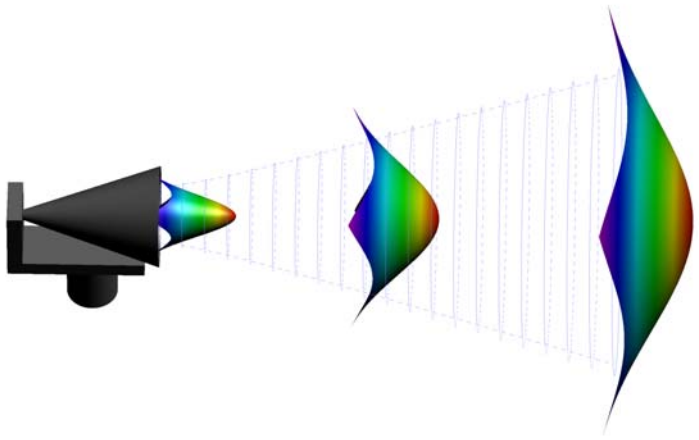

Figure 4.2: Description of the Gaussien beam emitted from a horn antenna

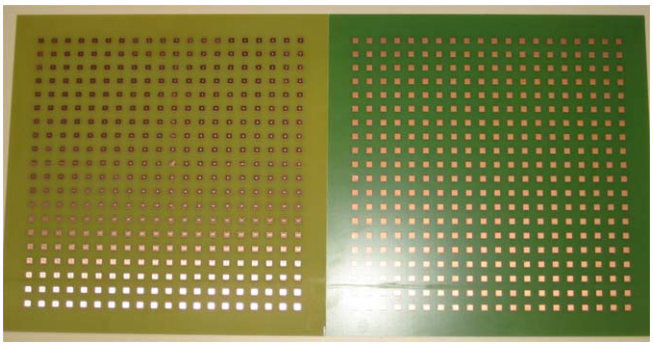

Figure 4.3: Two samples (Left: mushroom structure with vias; Right: mushroom structure without vias)

so the bench is equipped with a micrometer and is piloted via a Labview program. We can not only control the amplitude of the movements, but also set their velocity and acceleration. The bench is solid enough to be rotated, so the antenna's position can be tuned to achieve an oblique incidence. Since the weight of the bench becomes important, the plomb counterweights are added in the device.

Figure 4.4 illustrates the positions of the antenna and the lens and here we give a short introduction on how to choose a suitable lens for our system.

The place where the spot size of the propagating beam has a minimum value is known as the beam waist. The Rayleigh range (from $d_2 - \pi\frac{w^2}{\lambda}$ to $d_2 + \pi\frac{w^2}{\lambda}$) is a region around this waist, in which the wavefront can be considered as planar. To choose such a lens, its beam waist at

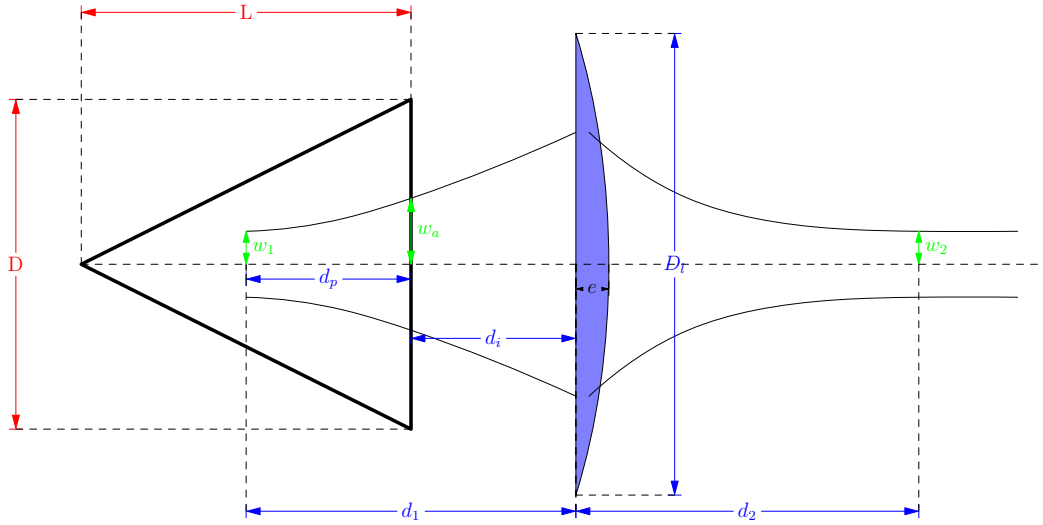

Figure 4.4: Description of the focus of a Gaussien beam by adding a lens

position d_2 is required to be relatively stable in a certain frequency range. Then, during the process of the characterization, there is no need to frequently change the lens. The diameter D_l of the lens's surface should be large enough to cover the aperture of the horn antenna and the width e of the length should be much less than D_l. The radius ($R = D_l/2$) and the thickness e of the lens depend on its focal f and its index n, as follows:

$$R = f(n-1), \tag{4.1}$$

$$e = R - \sqrt{R^2 - (\frac{d}{2})^2}. \tag{4.2}$$

In our case, the lens is made of a Rexolite material (n = 2.45), which is a low-loss material. The distance d_i between the lens and the antenna is considered to be null. This choice may reduce the loss created by the diffraction and the radius of the lens. At the same time, this choice also requires a lens of smaller size. This is because the Gaussian beam will be enlarged after leaving the horn and a larger distance d_i asks for a larger lens. More constraint conditions have been considered in choosing the lens, such as the position of the waist, the operational frequency bandwidth and they are more detailed in [108].

Finally, we opt for a lens with a focus $f = 15cm$ and a thickness $e = 3.5cm$. This lens allows us to place the sample between 3 cm and 13 cm away from the horn antenna, in which region the incident wave impinging on the sample can be considered as plane in the whole measuring band.

Calibration with TRL Technique

The electromagnetic response of a material is analyzed by measuring its scattering parameters (S-parameters). The two most widely-tested parameters in S-parameter measurements are S_{11}(the reflection coefficient) and S_{21}(the transmission coefficient). In measuring all the HIS samples, we are interested in S_{11}, especially in its phase. This reflection phase curve allows us to identify the resonance and the effective working bandwidth of each HIS structure.

The Network Analyzer measures the two-port scattering parameters of a device under test (DUT). This is specifically done by measuring the ratio of the reflected and outward waves of ports one and two, respectively, to the incident wave. However, the response of DUT measurement will be affected by the cables, connectors, measurement errors and port mismatches. To correct the measured results from such bad influences, different calibration procedures or standards have been proposed. One robust technique is the TRL calibration technique, where TRL stands for Thru, Reflect, Line. It allows for calibrating the instrument to take into account discontinuities associated with the cable and on-board connectors. After the calibration procedure, parasitic reflections are removed by a time domain analysis.

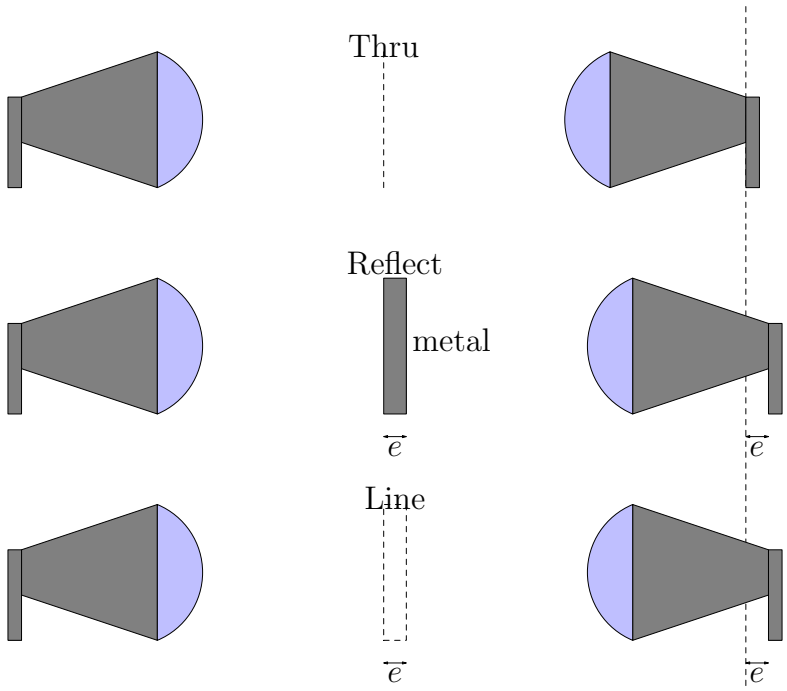

Figure 4.5: Calibration with the Thru, Reflect and Line method

The TRL technique requires three experiments, illustrated in Fig. 4.5.

1) The first measurement is performed in free space without anything between the two

horn antennas, which corresponds to the case "Through". In this case, $S_{11} = S_{22} = 0$ and $S_{12} = S_{21} = 1$.

2) During the second measurement, a totally metallic card having the sample's width is put in middle position of the two antennas. In this process, one antenna will be moved backwards to a distance equal to the sample's width e. This represents the case "Reflection" and the S-parameters become: $S_{11} = S_{22} = -1$ and $S_{12} = S_{21} = 0$.

3) In the third measurement, the two antennas keep the same positions as in the second measurement. We measure an air sample having the same width as the sample. In the case of "Line": we have $S_{11} = S_{22} = 0$ and $S_{12} = S_{21} = e^{j\beta e}$ (the superscript e represents the sample's width, $\beta = \frac{2\pi}{\lambda}$).

Temporal filter

In experiments, one may choose to measure the results either in temporal domain or in frequency domain. The results can be turned from one to the other by Fourier transform. At a given frequency, the frequency result of S parameter accounts for the transmission and the reflection signals in the whole system, while the temporal result of this same parameter will show the mix reaction of the system at a given moment. At the initial moment, the signal is emitted from Port 1 and then it is possible to trace the reflected signal in the temporal domain and view its interaction with various constituents on the workbench (like lens, antennas, samples, lens support, etc.) till its return to Port 1. The response of the sample can be identified and isolated (as seen in Fig. 4.6) from the noise signal by using a filter.

In our test, the S-parameters are measured in the frequency domain. After the calibration, a digital filter in the temporal domain is used in data-processing. Filtering is done by multiplying the inverse Fourier transform of the signal by a window function. This window function (also known as the apodization function) can eliminate the parasite transmission or reflection signals and keep only the useful points relevant to the sample's response. There are many possible forms for the window function (as seen in Fig. 4.7), such as the rectangle window, the Hanning window and so on. After using the filter, we can use Fourier transform to restore the results in frequency domain.

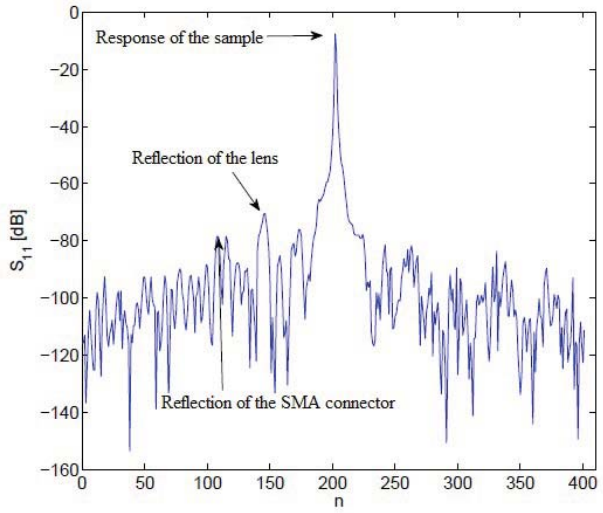

Figure 4.6: Identify the interreflection parasite signal from a temporal response of the reflection parameter

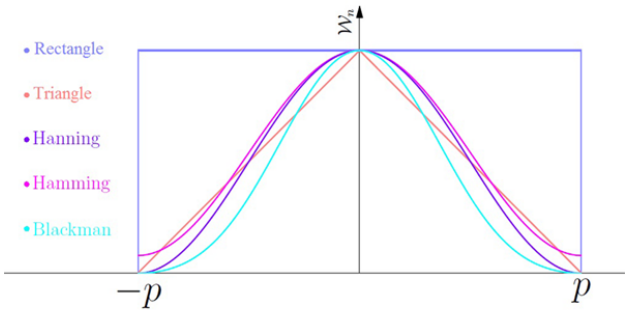

Figure 4.7: Filters with different windows

4.2 Experimental Results

4.2.1 Symmetric HIS Structures

Mushroom Structures

The first sample to be characterized is a mushroom structure without vias, whose dimensions are $150mm \times 150mm$, with 15×15 square patches on one side (machined by photo-lithography) of the substrate and a metal plane on the other side. (The dimensions of a unit cell of Sample M1 are: D= 10 mm, g= 5 mm, h= 1.6 mm.) The relative permittivity of the substrate is considered as a constant value, 4.4.

In Fig. 4.8, we compare the measurement results with analytical results for a Mushroom structure. All the analytical methods have been introduced in detail in Chapter 2. From the figure, the resonant frequency read off from Sievenpiper's effective model [22] is close to the measurement result, whereas the other two analytical methods predict a higher resonant frequency. The transmission-line model proposed by Olli [102] is an improved version of the TL model proposed by Simovski [79] and it really showed a more accurate prediction of the resonance here. However, these two TL analytical models are not suitable for structures in which the unit cell's size is much greater than the height of the HIS structure.

Figure 4.9 shows a comparison between numerical and measurement results. A numerical

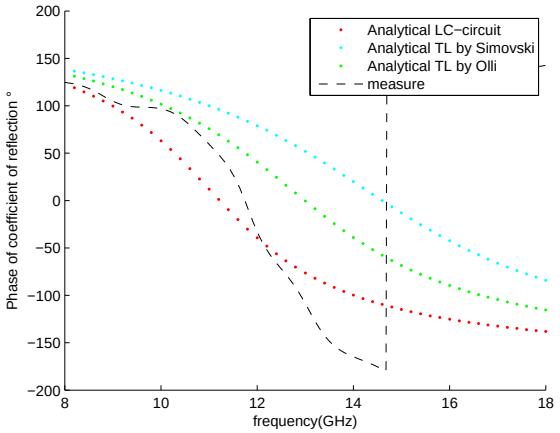

Figure 4.8: Analytical and experimental results of reflection coefficient for a Mushroom structure without via (Sample M1)

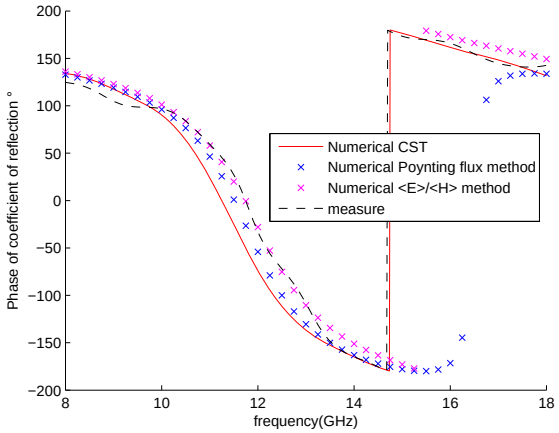

Figure 4.9: Numerical and experimental results of reflection coefficient for a Mushroom structure without via (Sample M1)

simulation performed with the commercial software CST Microwave Studio is also added. Results of our own numerical calculations are close to the CST ones. Below 14GHz, they show a very good agreement between numerical and measurement results. The range of the bandwidth is defined as the phase between $-90°$ and $90°$. Within this range, our numerical simulations and the CST simulation all show satisfying results, which further validate our two proposed numerical methods.

Method	Resonance	Bandwidth
Measurement	11.74	10.33 - 12.77
Analytical method: Sievenpiper	11.2	9.3 - 13.6
Analytical method: Ollis	13	10.5 - 16
Analytical method: Simovski	14.6	11.5 - 18.2
Numerical method: <E>/<H> method	11.74	10.3 - 12.7
Numerical method: Poynting flux method	11.5	10.2 - 12.4
Numerical method: CST	11.02	9.85 - 11.9

Table 4.1: Comparison of resonance and bandwidth with different methods for Sample M1

A summary of the results obtained from different methods is listed in Table 4.1, which offers a clearer view, allowing to see the difference and to compare the methods for accuracy.

Since one measurement cannot suffice, more mushroom samples (dimensions seen in Table 4.2) have been fabricated and tested. Some structures have vias and some without. In fabrication, the vias are the metalized cylinder holes in the middle of each patch.

Sample No.	D (mm)	g (mm)	h (mm)	ε_r	R_{via} (mm)
M1	10	5	1.6	4.4	no
M2	10	4	1.6	4.4	no
M3	7	2	1.6	4.4	no
M4	6	2	1.6	4.4	no
M5	10	4	2.4	4.2	no
M6	10	6	2.4	4.2	no
M7	10	4	2.4	4.2	0.5
M8	10	6	2.4	4.2	0.5

Table 4.2: Dimensions of the samples for the mushroom structure

In the previous test, the substrate had a relative permittivity of 4.4 and a thickness of 1.6 mm. In the following tests, we keep the same substrate, but vary the patch's dimension and the interval between two patches. Instead of making an inventory of all the results in figures, we have summarized the results of in Table 4.3 and Table 4.4. This table shows that the numerical simulations are in good agreement with measurements. Results obtained by the <E>/<H> method are a little bit closer to measurements than those of the Poynting flux method.

	Samples			
Resonance (GHz)	Sample M1	Sample M2	Sample M3	Sample M4
Measurement	11.74	10.35	9.99	10.84
<E>/<H> method	11.74	9.9	10.3	11.9
Poynting flux method	11.5	9.4	10.8	12
CST	11.23	9.54	10.09	11.82

Table 4.3: Bandwidths for different mushroom structures

	Samples			
Bandwidth (GHz)	Sample M1	Sample M2	Sample M3	Sample M4
Measurement	10.33 - 12.77	9.3 - 11.37	8 - 11.25	7.06 - 12.34
<E>/<H> method	10.3 - 12.7	8.8 - 10.8	8.9 - 11.7	10.25 - 13.75
Poynting flux method	10.2 - 12.4	8.3 - 10.3	9.3 - 12.2	10.6 - 13.75
CST	10.00 - 12.17	8.56 - 10.42	8.70 - 11.42	9.97 - 13.76

Table 4.4: Bandwidths for different mushroom structures

In our measurement, the excitation is a TE wave with normal incidence on the samples. Under this circumstance, the presence or the absence of vias will not largely influence the resonance, because there is no electric field traveling across the metal vias. In our numerical

simulations, the presence of the via is seen to cause a slight shift of the resonance to a lower frequency.

In all previous cases, the samples had no vias. In order to further investigate their influence, some samples with vias have been fabricated and measured. Because fabricating vias is a complex process, only two samples are available at present. Figure 4.10 and Figure 4.11 present the numerical and measurement results correspondent to different samples. As a rule, the numerical results agree with measurements.

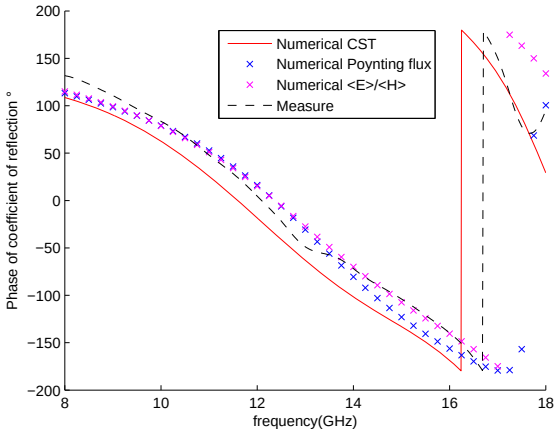

Figure 4.10: Numerical and experimental results for Sample 5

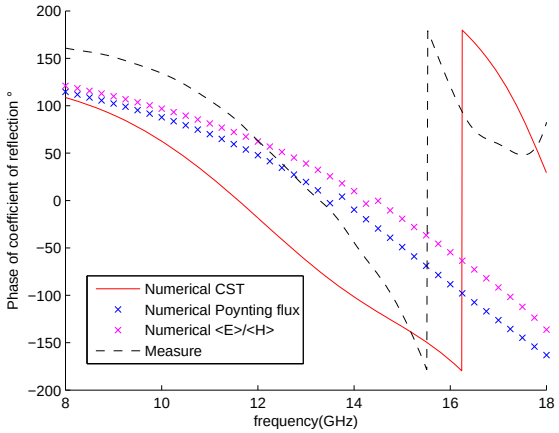

Figure 4.11: Numerical and experimental results for Sample 6

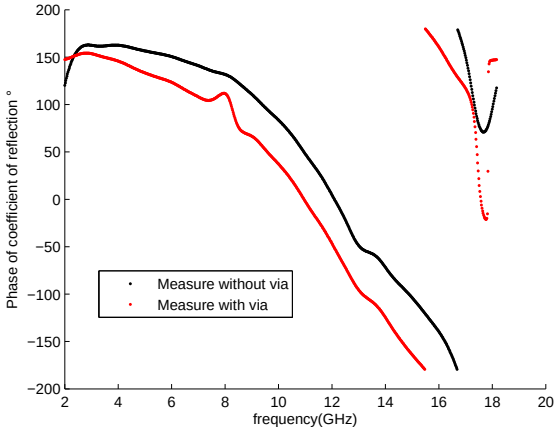

Figure 4.12: Experimental results for Sample 5 and Sample 7

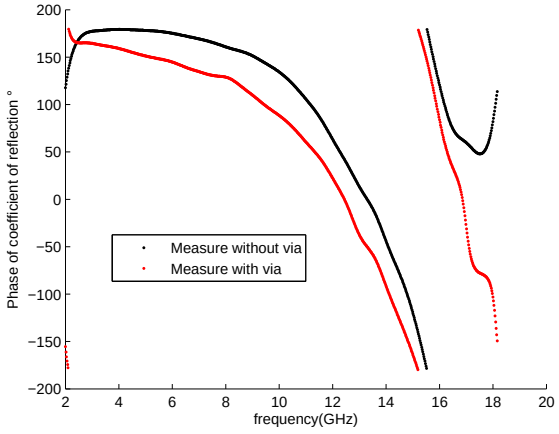

Figure 4.13: Experimental results for Sample 6 and Sample 8

Figure 4.12 and Figure 4.13 present the measurement results for the samples with and

without vias. From the figure, one sees that the influence of the via is more evident than the numerical predictions. This may be attributed to two reasons: 1) The experimental environment is not ideal and the substrate is lossy. The presence of the vias will enforce the lossy part of the effective permittivity, compared to the sample without vias. This will lead to a clearer difference between the samples. 2) During the process of the measurement, the samples are fixed by hand, so the unstable movement may also result in a variance.

Jerusalem-cross Structures

The second type of HIS sample to be examined is the Jerusalem-cross structures. Two JC structure samples (dimensions seen in Table 4.5) without vias are fabricated and measured.

Sample No.	D (mm)	g (mm)	d (mm)	w (mm)	h (mm)	ε_r
J1	2.4	0.4	1.2	0.2	1.6	4.2
J2	10	6	2	1	2.4	4.2

Table 4.5: Sample dimension of mushroom structure

In the following figures, we will compare respectively the analytical calculations and our numerical calculations against the measurements.

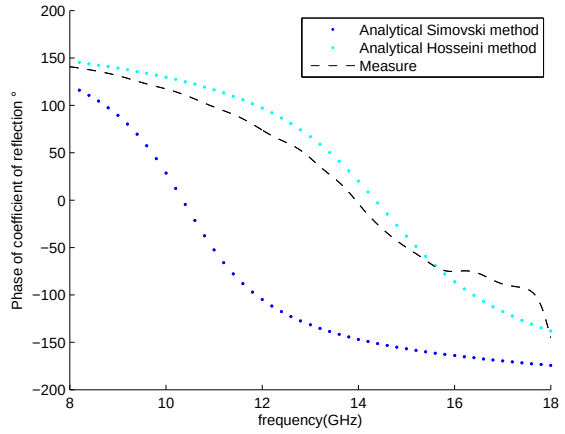

Figure 4.14: Analytical and experimental results for Sample J1

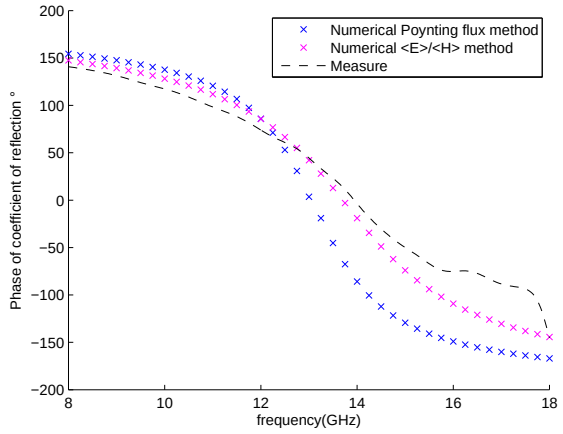

Figure 4.15: Numerical and experimental results for Sample J1

Figure 4.14 presents a comparison between analytical and measurement results for the first JC sample, in which Hosseini's analytical model [81] shows a very good accordance in the frequency range between 10 GHz and 15 GHz. Simovski's analytical model [79] is less effective

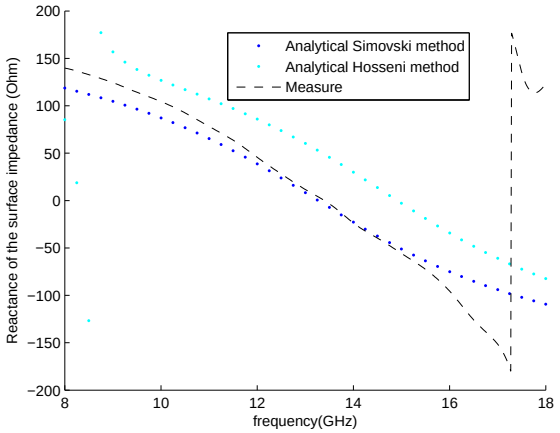

Figure 4.16: Analytical and experimental results for Sample J2

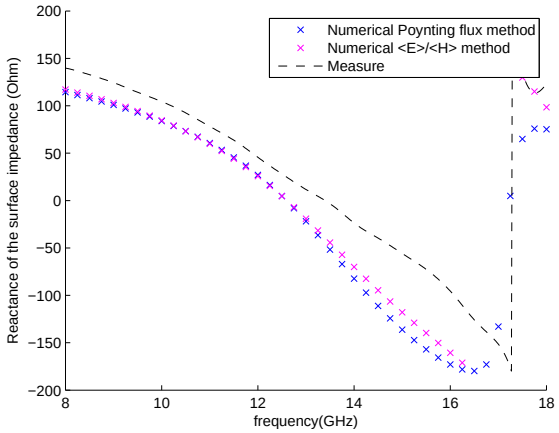

Figure 4.17: Numerical and experimental results for Sample J2

in this case. Figure 4.15 presents a comparison between results for the first JC sample, in which the difference between our numerical results and measurements are acceptable.

Figure 4.16 presents a comparison between analytical and measurement results for the second JC sample, in which Simovski's numerical model shows a better agreement than Hosseni's one with measurements. Figure 4.17 presents a comparison between numerical and measurement results for the second JC sample, in which the results given by the <E>/<H> method are closer to measurements than those obtained with the Poynting flux method.

These figures show that our numerical methods are in satisfying accordance with measurements. As for the analytical models, their effectiveness largely depends on the HIS dimensions.

4.2.2 Asymmetric HIS Structures

Our proposed numerical methods are able to calculate the surface impedance not only for symmetric HIS structures, but for asymmetric HIS structures as well. Same as before, when the E-field excitation is parallel to the x-axis, we say the incident wave is horizontally polarized; when the E-field excitation is parallel to the y-axis, we say the incident wave is vertically polarized. For symmetric structures, the measurements are the same with respect to both polarizations. However, for asymmetric structures, the orientation of the E-field excitation should be taken into account.

In the following part, we'll measure some samples of asymmetric HIS structures and all the samples will be measured twice: 1) with an horizontally polarized incident wave; 2) with a vertically polarized incident wave.

Rectangle HIS Structures

The first asymmetric structure to be characterized is the rectangle HIS structure, which has already been numerically investigated in the previous section. Here, we focus on the comparison between our numerical results and the experimental results. The sample of rectangle HIS structure (Rec1) has the dimension as: Dx = 4 mm, Dy = 6 mm, W = 7 mm, L = 9mm, h = 1.6 mm, $\varepsilon_r = 4.2$.

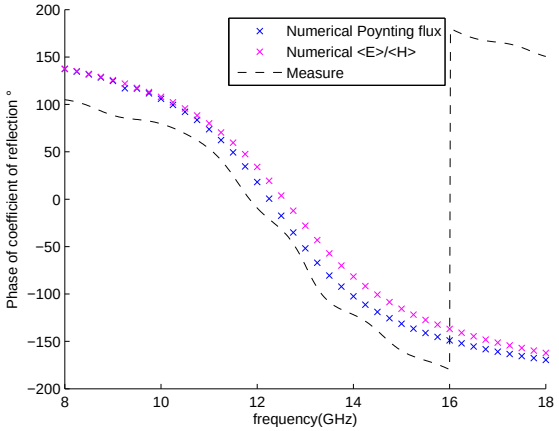

Figure 4.18: Numerical and experimental results for Sample Rec1 with horizontal E-field polarized excitation

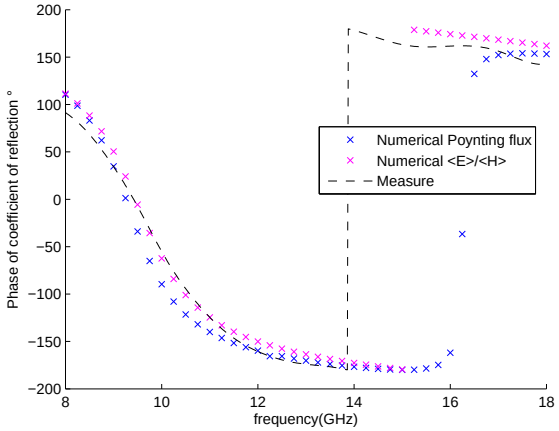

Figure 4.19: Numerical and experimental results for Sample Rec1 with vertical E-field polarized excitation

Figure 4.18 corresponds to the case with a vertically polarized incident wave and Figure 4.19 corresponds to the case with a horizontally polarized incident wave. These two figures confirm that our numerical methods are able to predict the resonances with respect to different polarizations.

Square HIS Structure with Slot Cut

In the previous section, we have already investigated some asymmetric HIS structures, such as fork-like structures, one spiral-arm structures, etc. From results for these structures, one sees that a complicated asymmetric geometry may cause many resonances with narrow bandwidth, leading to an uninterpretable figure. Therefore, we study several asymmetric HIS structures with relatively simple geometries here. In the following part, we will calculate the reflection phase of these structures by our numerical methods and check their effectiveness against the experimental results about some samples.

The Mushroom structure (without via) is a grounded substrate with periodic square patches on its top surface. Based on this structure, we design three asymmetric HIS structures by adding slot cuts on the square patches. The first structure (CutI) has an additional rectangle slot inside the square patch, and the geometry of its unit cell is shown in Fig. 4.20. The second structure (CutA) has an additional rectangle slot on the side of the square patch, and the geometry of its unit cell is shown in Fig. 4.21. The third structure (CutL) has an additional L-shape slot inside the square patch and the geometry of its unit cell can be seen in Fig. 4.22.

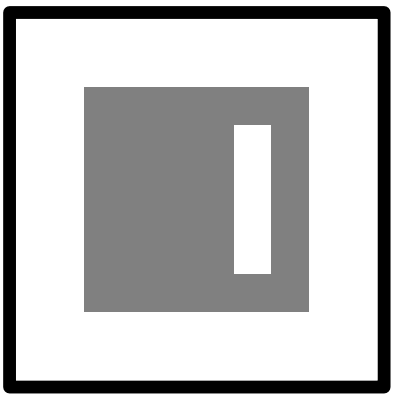

Figure 4.20: Unit cell of structure CutI (top view)

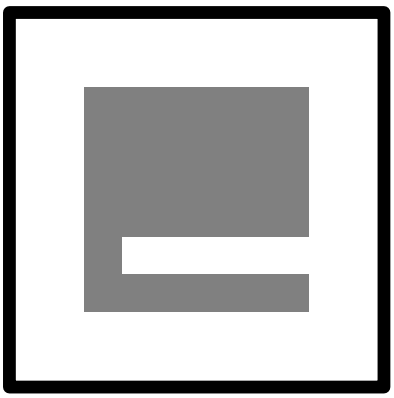

Figure 4.21: Unit cell of structure CutA (top view)

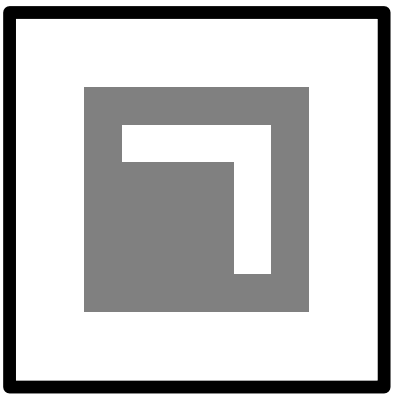

Figure 4.22: Unit cell of structure CutL (top view)

Figure 4.23 and Figure 4.24 present the results for the first structure (with a rectangle slot cut inside the square patch) with respect to two different polarizations. It is observed that the resonances corresponding to two different polarizations are not much different from each other: the resonance corresponding to the horizontally polarized excitation is a little higher than 10 GHz; the resonance corresponding to the vertically polarized excitation is a little lower than 10 GHz. This is because the outline dimension of the structure dominates the principal resonance. The slot cut inside the square patch does do impact on the resonance, but slightly.

Figure 4.25 and Figure 4.26 present the results for the second structure (with a rectangle slot cut aside the square patch) with respect to two different polarizations. It is observed that the resonance with respect to the vertically polarized excitation will be higher than the one with respect to the horizontally polarized excitation. This is mainly due to the fact that the cut aside is so long that it changes the continuity of the metal in one direction and a smaller width yields a higher resonance.

In comparison with the first structure, which has a cut inside, the difference between the numerical and the experimental results for the second structure with a cut aside is more evident. In this case, the outline plays an important role of defining the resonance.

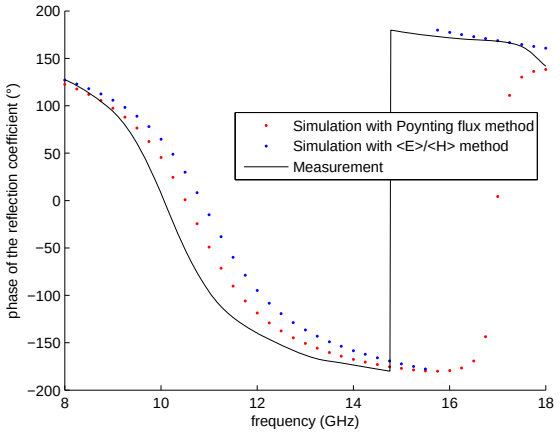

Figure 4.23: Numerical and experimental results for structure CutI with horizontally polarized excitation

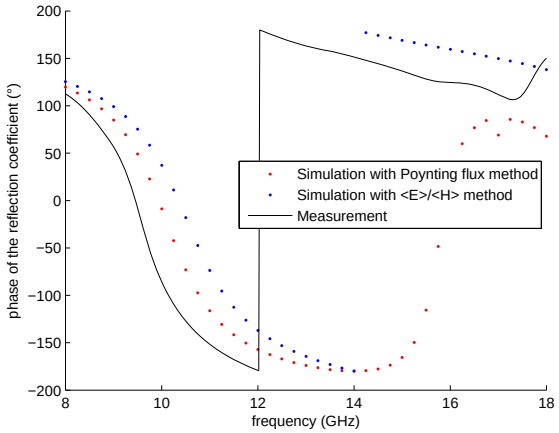

Figure 4.24: Numerical and experimental results for structure CutI with vertically polarized excitation

Figure 4.27 and Figure 4.28 present the results for the third structure (with a L-shaped slot cut aside the square patch) with respect to two different polarizations. This structure is asymmetric with respect to the horizontal line in the middle of the patch, but it is fourfold rotationally symmetric. So, the reflection phase curves for both polarizations almost coincide. As the outline of the square patch doesn't change, the main resonance is still found at around 10 GHz. It is observed that the L-shape cut does have an impact on the results. The numerical results show parasitic resonance around 15 GHz. The measurement results show that the bandwith is a little broadened.

Both the numerical methods and the measurements address the average values of the electromagnetic field on the observation surface. When the geometry inside the patch is complicated, the numerical results and the experimental results are in less accordance.

It is observed that the main resonance of the structure depends on its global dimension. An additional cut may shift the resonance (eg. structure 2), or create one or several parasitic resonances (eg. structure 3). These figures show our numerical results in agreement with the measurements, as a rule. This further confirms that our numerical methods are workable.

In addition, the study on different cuts for a Mushroom structure may give some guidelines in designing HIS geometries.

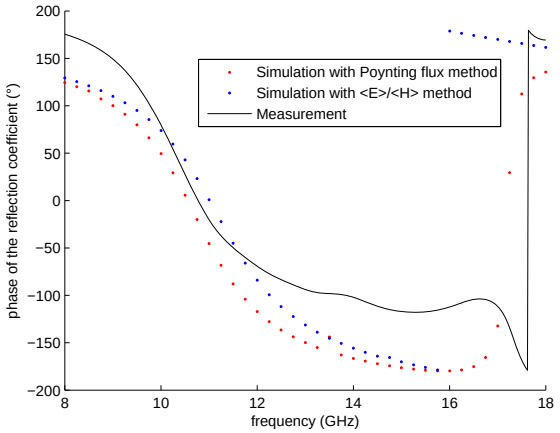

Figure 4.25: Numerical and experimental results for structure CutA with horizontally polarized excitation

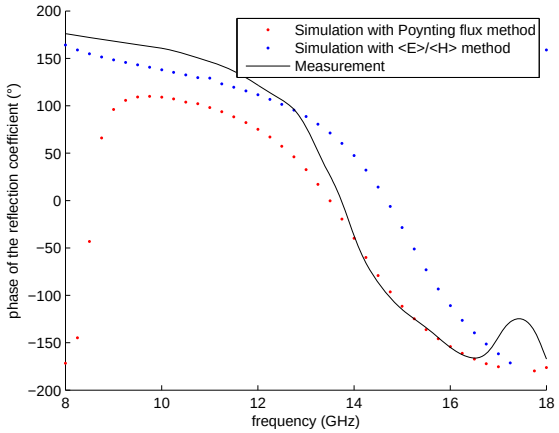

Figure 4.26: Numerical and experimental results for structure CutA with vertically polarized excitation

4.3 Discussions

Effective bandwidth

After the calibration, a digital filter in the temporal domain is used in data-processing. However, the transformation of the filter will cause a distortion on the signal. It is found that the Gibbs phenomenon [109] will occur and introduce big oscillations at the beginning or at the end of the bandwidth. Therefore, the effective band should take the middle part of the band.

Let us take an example to show the impact of the Gibbs phenomenon on our measurement results. Fig. 4.29 and Fig. 4.30 correspond the S-parameters after applying a digital filter with a rectangle window, with two different window widths (including respectively 5 samples and 15 samples). In these two figures, the dashed curves correspond to the theoretical S-parameter and the solid curves correspond to the measured S-parameters. The Gibbs phenomenon is clearly shown at two ends of the working band. The working band with of the horn antenna is from 2 GHz to 18 GHz. However, it is observed that the reliable results are rather between 8 GHz and 16 GHz.

Dielectric properties of the substrate

The dielectric permittivity is a complex value in reality. At low frequency (less than 1 GHz), it is relatively stable, but at high frequency (around 10 GHz) it varies a lot. In our numerical simulations, a small variation on the permittivity may cause a large resonance shift. In some

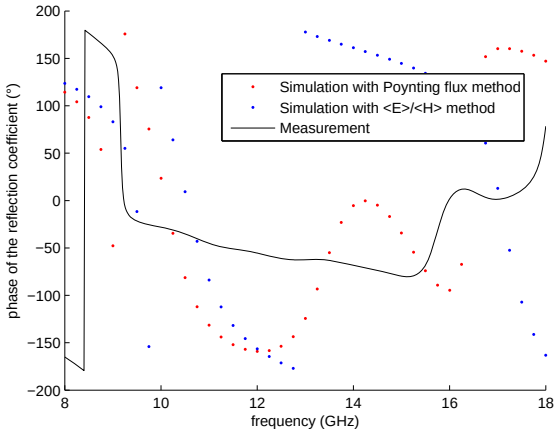

Figure 4.27: Numerical and experimental results for structure CutL with horizontally polarized excitation

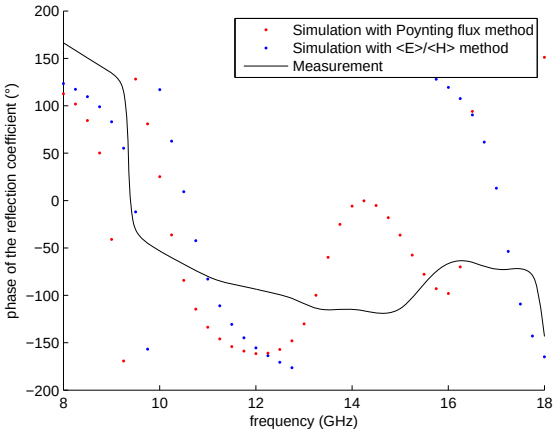

Figure 4.28: Numerical and experimental results for structure CutL with vertically polarized excitation

cases, the shift may reach 0.5 GHz or even more.

The experimental results are mainly used to verify the effectiveness of our numerical models. In our numerical simulations, the relative permittivity is set as a constant value. In order to reduce the difference between the numerical results and the experimental results, it's better to measure the permittivity of the substrate before proceeding with the numerical simulation.

For example, we design a sample with a resonance at around 10 GHz. We will measure the relative permittivity of the sample and verify the value around 10 GHz. As shown in Fig. 4.31, the measured value is between 4.3 and 4.4. Then we may set 4.3 or 4.4 as the relative permittivity of the substrate in the numerical simulations.

Position of the sample

The metal supports can not be used to fix the samples and the non-metallic supports are not available at the moment. In our measurements, some cards are hand-held, which potentially causes more or less unstable results. A small shake may bring about an error, especially for the samples largely covered with metal elements. This is because these samples are more sensitive to the angle of incidence. With a non-metallic support, the accuracy of measurements may be improved.

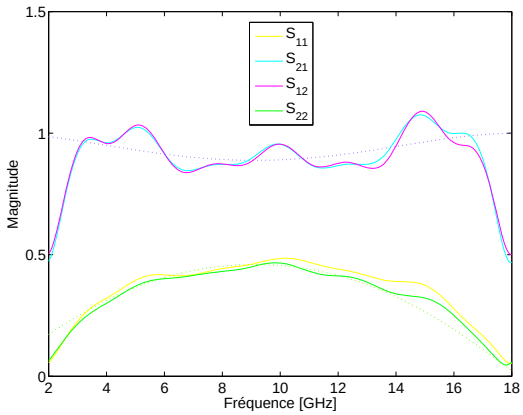

Figure 4.29: Measured and theoretical S-parameters after applying a rectangle window with width = 5 samples

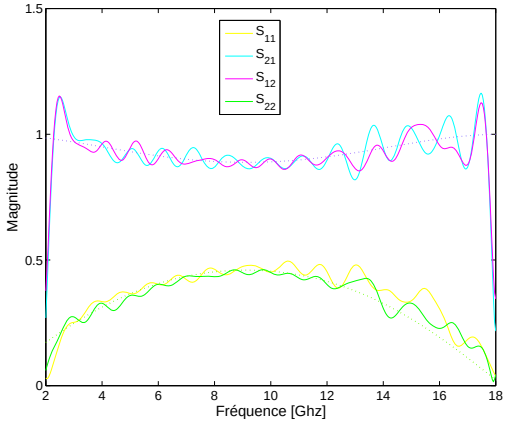

Figure 4.30: Measured and theoretical S-parameters after applying a rectangle window with width = 15 samples

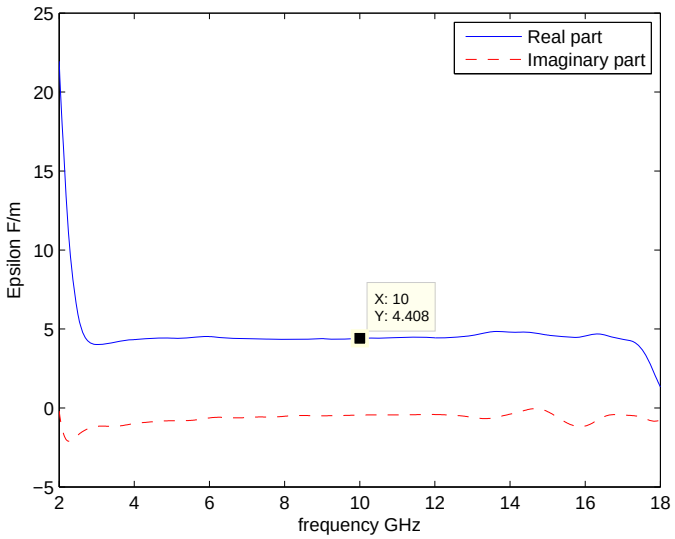

Figure 4.31: Measurements of the relative permittivity

Chapter 5

Equivalent Model

5.1 Concept

Various kinds of HIS structures have been proposed and investigated. Due to the complexity and the diversity of these structures, the presence in them of tiny features requires a fine mesh in numerical simulations, resulting in a big expense of both memory and computing time. This motivates our attempt to find an equivalent model based on the idea of replacing the heterogeneous assembly of patches and vias by a single homogeneous surface. It takes a lot of time to calculate the equivalent impedance surface and build the equivalent model in the first place. However, applying this equivalent model into an antenna system with HIS structures, the computing time of the numerical simulations can be largely reduced, since a more uniform study domain permits the use of a coarser mesh, hence a shortened calculation.

Fig. 5.1 displays the concept of constructing an equivalent model for an antenna system. The model with all the original HIS structures is called "Direct Model", as shown in the left of the figure. The first step is choosing an observation surface located at l in the direct model. The second step is calculating the surface impedance of this chosen surface in the direct model. The third step is cutting the direct model into two parts, one on each side of the observation surface and keeping only the upper part of the model. The last step is applying the surface impedance condition to the bottom surface of the remaining part. Here comes the equivalent model as seen in the right of the figure. The objective of the equivalent model is to serve as a simulation tool for the antenna design. It is to be noted that the observation surface should be higher than the HIS top structures, but lower than the position of the antenna.

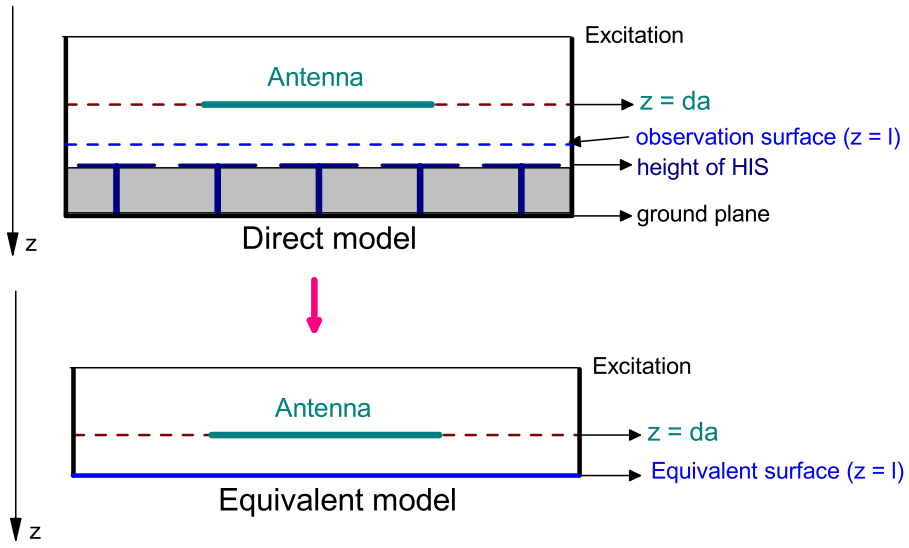

Figure 5.1: The concept of equivalent model in presence of a wire antenna

5.2 Theory

In [117], it is proposed that the incorporation of lumped resistors, inductors, and capacitors is effected through the direct stamping of the state-space voltage-current relationship for these elements in the matrices of the generated state-space form of the discrete model. Using edge elements as basis functions in the Galerkin method, the weak formulation that corresponds to an electromagnetic problem leads to a matrix equation of the following kind:

$$\begin{bmatrix} Y_{11} & \cdots & Y_{1n} \\ \vdots & \ddots & \vdots \\ \vdots & Y_{ee} & \vdots \\ \vdots & \ddots & \vdots \\ Y_{n1} & \cdots & Y_{nn} \end{bmatrix} \cdot \begin{bmatrix} e_1 \\ \cdots \\ e_e \\ \cdots \\ e_n \end{bmatrix} = \begin{bmatrix} i_1 \\ \cdots \\ i_e \\ \cdots \\ i_n \end{bmatrix}, \tag{5.1}$$

where n is the number of degrees of freedom (DOF), $[e]$ is the vector of edge emf's (in volts), $[i]$ is the excitation current vector (in amperes) and $[Y]$ is an admittance matrix which governs the interaction between edges. This admittance matrix is assembled from the volumic integrals in the tetrahedral elements while the excitation current vectors results from the boundary conditions of the EM problem.

In the language of circuit theory, one edge e can be assimilated with a port with its own

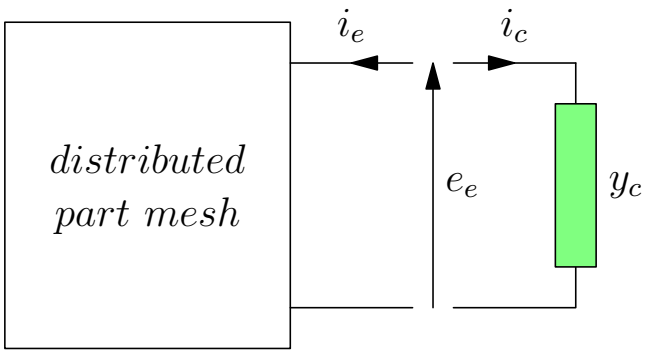

Figure 5.2: A lumped element is connected to an edge element

voltage and current, respectively denoted by e_e, e_i, and one has:

$$i_e = \sum_{k=1}^{n} Y_{ek} e_k. \tag{5.2}$$

where n is the number of DOF. The matrix term Y_{ee} can be seen as the self admittance of the edge e, while a matrix term Y_{ek} gives the mutual admittance between edge e and edge k.

If a lumped element component is connected to this kind of port (illustrated in Fig. 5.2), the Kirchhoff laws can be written as:

$$\sum_{k=1}^{N} Y_{ek} \cdot e_k = -y_c \cdot e_e. \tag{5.3}$$

where y_c is the admittance of the lumped element.

In [116], it is shown that the insertion of a lumped element (a resistor R, a capacitor C, or an inductor L) at an edge e modifies the self admittance of the edge e as follows :

$$Y_{e,e} \to Y_{e,e} + \frac{1}{R}, \tag{5.4}$$

$$Y_{e,e} \to Y_{e,e} + j\omega C, \tag{5.5}$$

$$Y_{e,e} \to Y_{e,e} + \frac{1}{j\omega L}. \tag{5.6}$$

If the lumped element is added at a known position, the problem can easily be resolved by solving the equations above. However, in our case, the lumped elements will be added to a 2D surface, the y_c above will now turn into a 2×2 matrix and the contribution of the lumped elements on each edge should be considered in two dimensions too, as:

$$\begin{bmatrix} Y_{e,e} & Y_{e,e'} \\ Y_{e',e} & Y_{e',e'} \end{bmatrix} \rightarrow \begin{bmatrix} Y_{e,e} + y_{c11} & Y_{e,e'} + y_{c12} \\ Y_{e',e} + y_{c21} & Y_{e',e'} + y_{c22} \end{bmatrix}. \tag{5.7}$$

The modified matrix encodes not only the element's self effects, but also the mutual effects among them.

In the previous part, we considered the equivalent surface problem in a micro view. In the following part, we will directly consider the problem of adding a lumped-element condition into the whole system in a macro view and give the main steps of how to program this condition in the FEM.

In Chapter 1, the weak formulation corresponding to our electromagnetic problem was written as:

$$\int_D \left[\frac{1}{\mu}(\nabla \times E) \cdot (\nabla \times v) + \varepsilon \frac{\partial^2 E}{\partial t^2} \cdot v\right] + \int_S (n \times \nabla \times E) \cdot v = -\int_D \frac{\partial J_e}{\partial t} \cdot v, \tag{5.8}$$

where S is the boundary of the studied domain, n denotes the unit vector normal to S, ε is the permittivity in Ω and μ is the permeability in Ω. This equation must be satisfied for all test functions v.

Suppose that we apply a new boundary condition on the surface S_n ($S_n \subset S$), which means adding a new term to the right-hand side of 5.8:

$\int_D \left[\frac{1}{\mu}(\nabla \times E) \cdot (\nabla \times v) + \varepsilon \frac{\partial^2 E}{\partial t^2} \cdot v\right] + \int_D \frac{\partial J_e}{\partial t} \cdot v =$

$$-\int_S (n \times \nabla \times E) \cdot v + \int_{S_n} (n \times \nabla \times E) \cdot v \; \forall v. \tag{5.9}$$

Generally, the boundary condition is formulated as:

$$n \times H = -Y \cdot E. \tag{5.10}$$

After applying the boundary condition 5.10 and Faraday's law, we have:

$$\int_{S_n} (n \times \nabla \times E) \cdot v = \int_{S_n} n \times (-\mu \frac{\partial H}{\partial t}) \cdot v = \frac{d}{dt} \int_{S_n} \mu Y \cdot E_B \cdot v, \tag{5.11}$$

where E_B is the vector of electric field on surface S_n. Then, discretizing the domain and applying the Galekin method, Eq. 5.11 becomes:

$$\mu \frac{de_i}{dt} \sum_{i=1}^{N_B} \int_{S_n} W_{j(2D)} Y \cdot W_{i(2D)}, \tag{5.12}$$

where $W_{i,j(2D)}$ is a two dimensional Whitney function.

Building the equivalent surface in the equivalent model amounts to adding such a new impedance boundary condition into the system to be solved. The weak formulation complemented with this new impedance boundary condition can now be presented in detail as:

$$\sum_{i=1}^{N}\frac{1}{\mu}e_i\int_D(\nabla\times W_i)\cdot(\nabla\times W_j)+\sum_{i=1}^{N}d^2e_i\int_D\varepsilon W_i\cdot W_j+\int_D W_j\cdot\frac{\partial J_e}{\partial t}$$

$$=-\int_S(\cdot)d(\partial\Omega)+\mu\frac{de_i}{dt}\sum_{i=1}^{N_B}\int_{S_n}W_{j(2D)}Y\cdot W_{i(2D)}.\ (\forall j=1,\cdots,N). \tag{5.13}$$

In programming, in order to add the new defined impedance boundary into the whole system, we have the following tasks to perform:

Step 1: Search for the elements which contain one triangle surface on the equivalent surface and save their element index;

Step 2: Verify all the faces of indexed elements, find the face contained on the equivalent surface and save its index;

Step 3: Add the contribution of the impedance boundary condition to the indexed face of each indexed element;

Step 4: Assemble the contribution of each element to the global stiffness matrix.

5.3 Simulations

The effectiveness of this equivalent model will be verified by comparing the E-field results respectively calculated in the direct model and in the equivalent model. The following test is based on a unit cell of mushroom structure without via.

The direct model displays a mushroom structure (D = 10 mm, g = 2 mm and h = 1.6 mm) in a cubic study domain (10 mm x 10 mm x 10 mm). The relative permittivy of the substrate is 3.4. In Chapter 3, the Poynting flux method and the <E>/<H> method are proposed to calculate the surface impedance of a chosen surface. Since we haven't sorted out which method offers a more accurate result, both of them will be used in obtaining the surface impedance value. In the direct model, the E-field will be calculated on two different lines parallel to the z-axis: One is in the center of the domain which traverses the metal patch (marked "Line 1" in Fig. 5.3); The other lies in the space between the patch and the boundary (marked "Line 2" in Fig. 5.3).

The dimension of the equivalent model depends on the height of the observation surface in the direct model. In this test, the observation surface is chosen at 2 mm from the bottom in

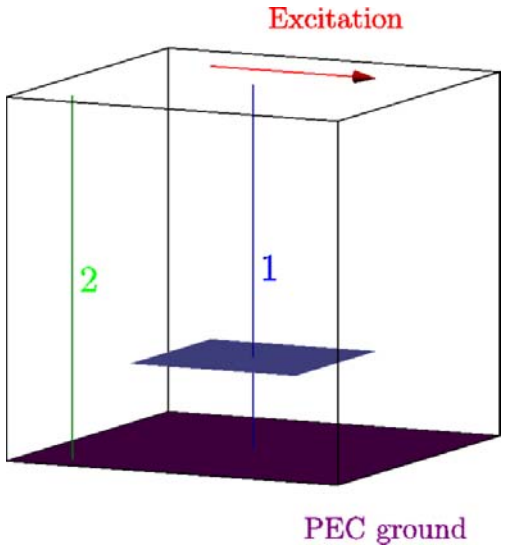

Figure 5.3: Observation lines in the direct model

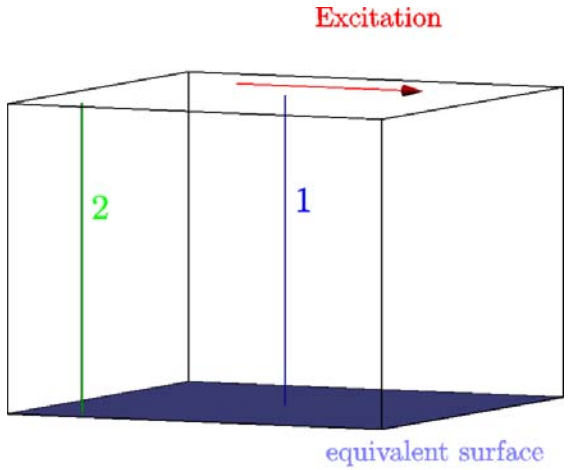

Figure 5.4: Observation lines in the equivalent model

the direct model, so the dimension of the equivalent model is designed as 10 mm x 10 mm x 8 mm. In the equivalent model, we choose two observation lines which have the same positions respectively as "Line 1" and "Line 2" in the direct model, as shown in Fig. 5.4, but shorter along the z-axis.

One should note that the results of E-field on any line parallel to z-axis are actually the same. This is because the bottom surface of the equivalent model is homogeneous and the top surface of the equivalent model is imposed a uniform E-field excitation. So, we only calculate the E-field result on one observation line in following simulations.

Fig. 5.5 presents four results: Two results display the E-field on two different observation lines in the direct model; The other two results display the E-field on two observation lines in the equivalent model by using the surface impedance value obtained from the Poynting flux method and the <E>/<H> method.

Let us first look at the two lines got from the direct model. The black line corresponds to the observation line through the metal patch and an attenuation of the E-field is evidently reduced around z = 1.6 mm, which reflects the existence of the patch. The blue line corresponds to the observation line without touching the metal patch. So, the attenuation of the E-field doesn't occur on this curve.

Then, we observe the E-field results from the equivalent model. Be it with the Poynting flux method or the <E>/<H> method, both lines show the same tendency as those in the direct model. In the region far from the HIS structure, the results are in good agreement, but in the

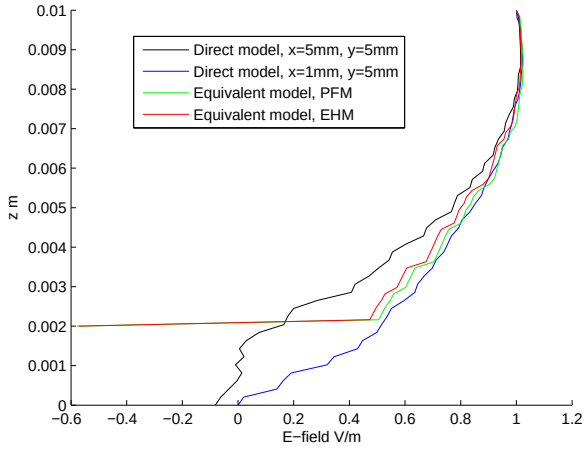

Figure 5.5: Simulations between the direct and the equivalent models

region near the HIS structures, their values differ more. This phenomenon is normal, because the equivalent model,with a largely simplified surface, cannot exhibit all the details as finely as the direct model. Especially, in the region near the HIS structures, the HIS structures have a strong reaction.

It is true that the equivalent model merely offers an approximate result, but the highly reduced computing time makes up for that.

5.4 Discussions

Fineness of the Mesh

Generally, a finer mesh yields a more detailed result. In previous chapters, the mesh with a "normal" type has already achieved the convergence, so here we just compare two mesh types: "normal" and "fine".

Figure 5.6 and Figure 5.7 show the comparisons respectively in the direct model and in the equivalent model. Since there is no big difference when changing the mesh type from "normal" to "fine", it is not necessary to mesh the study domain in a finer way by sacrificing more computing time. Therefore, the following simulations in this chapter will all adopt the "normal" mesh type for the direct model, as well as the equivalent model.

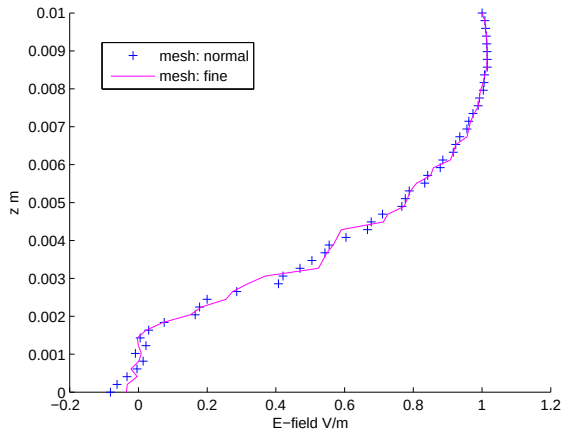

Figure 5.6: E-field in direct model with different mesh grains

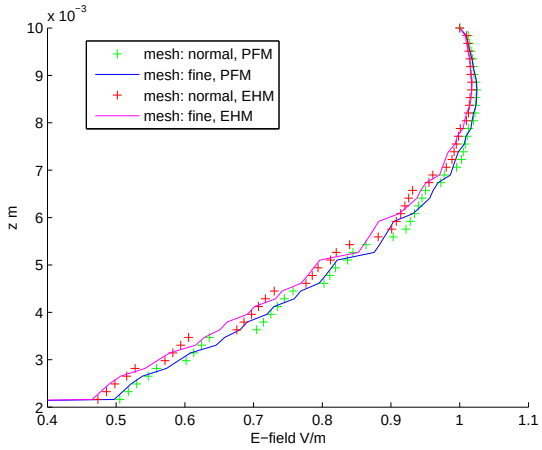

Figure 5.7: E-field in equivalent model with different mesh grains

Observation Surface

In Chapter 3, we discussed the relation between the accuracy of the surface impedance value and the height of the observation surface in the direct model. In order to get a higher accuracy, the height of the observation surface should be set simultaneously as high as possible to allow the recourse to homogenization theory and as low as possible to be useful as equivalent model for an antenna system.

The height of the equivalent model depends on the height of the observation surface in the direct model and the bottom surface of the equivalent model is characterized by the surface impedance calculated on this surface in the direct model. Thus, we carry out different simulations to study the impact of the observation surface height on the equivalent model. Let us take the mushroom structure as an example and suppose that the top surface of the mushroom structure is 1.6 mm. We will vary the height of observation surface ho from 1.8 mm to 2.4 mm with a step of 0.2 mm and then compare the E-fields in equivalent models with the ones in direct models.

Figure 5.8 displays five different E-field calculations on observation line “Line 1” at 8 GHz. One calculation is obtained from the direct model and the other four are obtained from the equivalent models, defined by different heights of observation surfaces. In this case, the surface impedance values are all computed by the Poynting flux method. In this case, it is observed that the results got from different equivalent models are similar to each other and it’s not easy to tell which one offers the best result. Figure 5.9 displays the results of E-field on observation Line “Line 1” at 8 GHz, while the surface impedance value are computed by the <E>/<H> method.

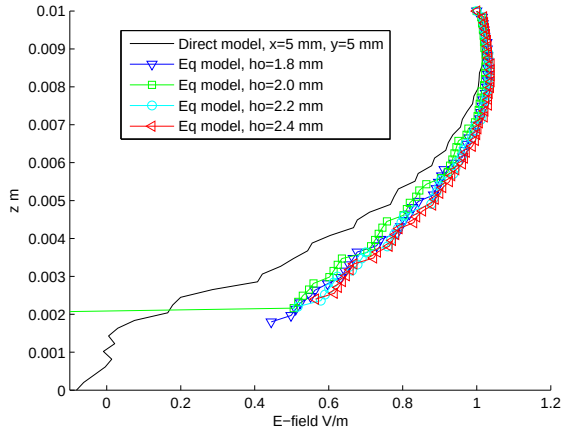

Figure 5.8: Study on different observation surface heights with the Poynting flux method, at 8 GHz, Line 1

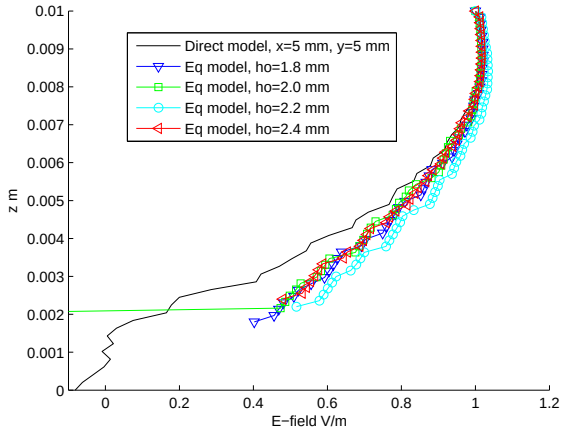

Figure 5.9: Study on different observation surface heights with the <E>/<H> method, at 8 GHz, Line 1

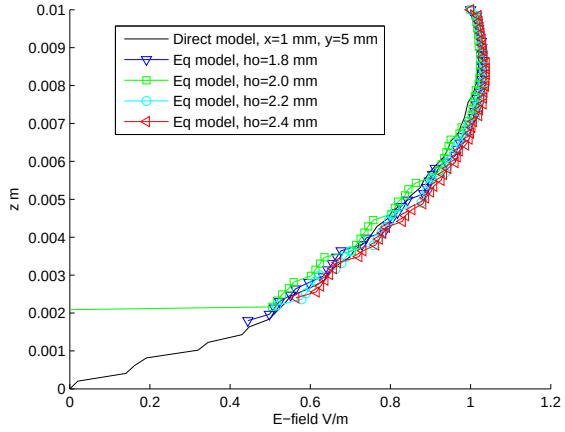

Figure 5.10: Study on different observation surface heights with the Poynting flux method, at 8 GHz, Line 2

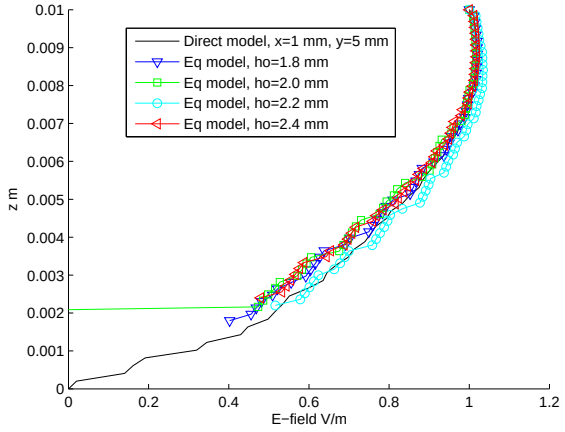

Figure 5.11: Study on different observation surface heights with the <E>/<H> method, at 8 GHz, Line 2

Compared with the results obtained from the other equivalent models, the result at the case of "ho = 2.2 mm" is a little far from the one got from the direct model. However, if we choose the observation line at position "Line 2" (as shown in Fig. 5.3 and Fig. 5.4), it is observed from Fig. 5.11 that the result at the case of "ho = 2.2 mm" becomes the best. From these results, we cannot get a clear conclusion about the relation between the height of observation surface and the accuracy of the equivalent model.

In Chapter 3, we also discussed another issue, the accuracy of the surface impedance value

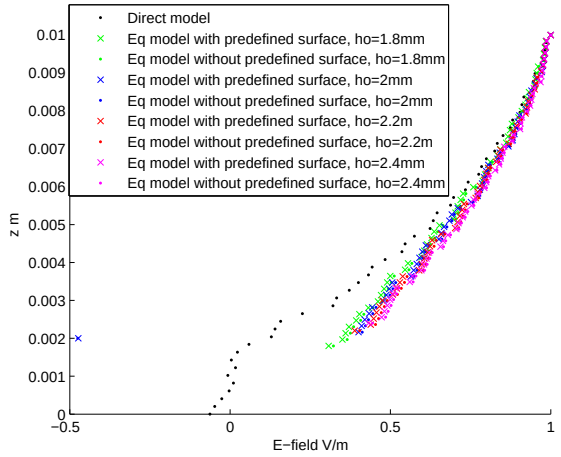

Figure 5.12: Study on the influence of the predefined observation surface by using Poynting flux method at 6 GHz

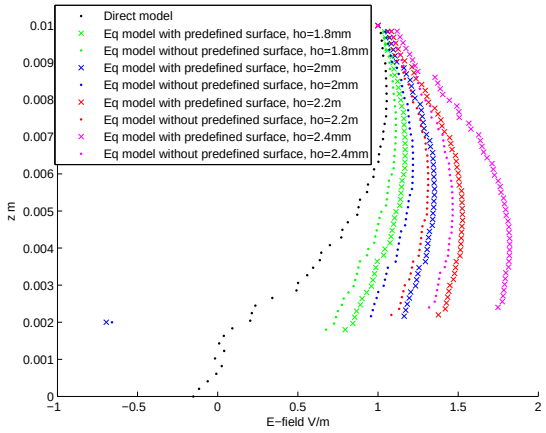

Figure 5.13: Study on the influence of the predefined observation surface by using Poynting flux method at 8 GHz

may be related to the existence of a geometrically predefined observation surface in meshing while using the Poynting flux method. Here, we also carry out several simulations to check the influence of this predefined surface. Again, we consider the mushroom structure without vias (D = 10 mm, g = 4 mm, h = 1.6 mm, $\varepsilon_r = 4.3$) in the direct model and build two corresponding equivalent models. The bottom surface of the first equivalent model is characterized by Z_S, calculated in the direct model with a predefined surface. For the second equivalent model, the model is characterized by Z_S, calculated in the direct model without a predefined surface.

Fig. 5.12 presents the calculations at 6 GHz. At the same time, we also vary the observation surface in the direct model and check their impact. In this case, it is observed that the results of the equivalent models are slightly improved, if the surface impedance valules are calculated in the direct model with a predefined observation surface.

Then, we do the same tests at a higher frequency, 8GHz. In this case, figure 5.13 shows that the existence of the predefined observation surface doesn't help improving the accuracy of the equivalent model and do the contrary. It seems that around the resonance, the influence of the poor condition number is much more important than the advantage brought by a predefined observation surface.

The Operating Frequency

In the previous subsection, the operating frequency is high, but not close enough to the resonance. The resonance corresponds to the observation surface at 2 mm is found around 12 GHz,

thus we carry out more simulations respectively at 10 GHz, 11 GHz and 12 GHz.

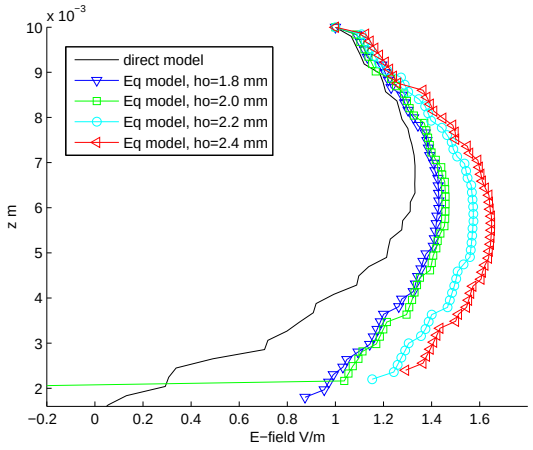

Figure 5.14: E-field in different models at 10 GHz. (The equivalent models are based on the surface impedance obtained by the Poynting flux method.)

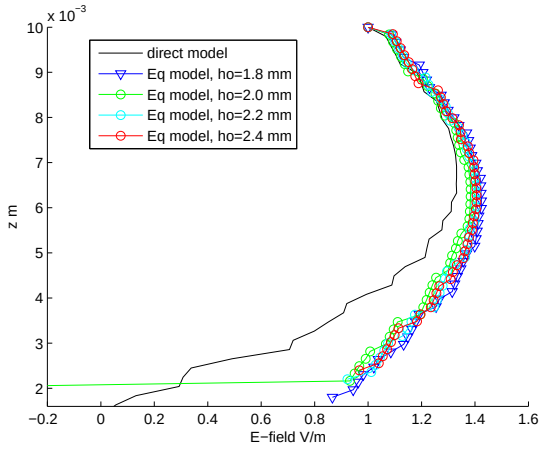

Figure 5.15: E-field in different models at 10 GHz. (The equivalent models are based on the surface impedance obtained by the <E>/<H> method.)

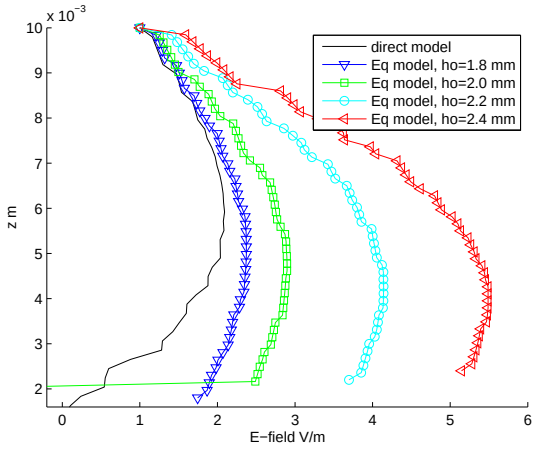

Figure 5.16: E-field in different models at 11 GHz. (The equivalent models are based on the surface impedance obtained by the Poynting flux method.)

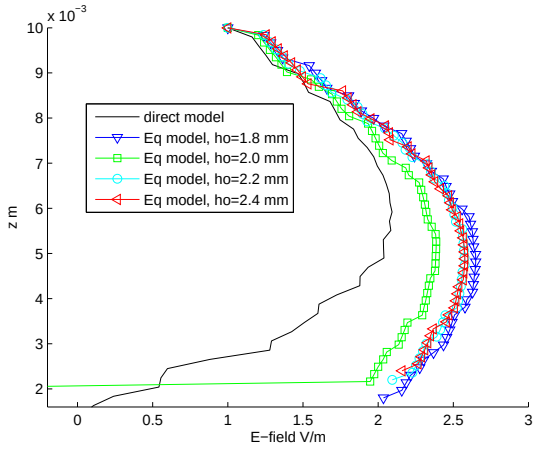

Figure 5.17: E-field in different models at 11 GHz. (The equivalent models are based on the surface impedance obtained by the <E>/<H> method.)

The E-fields in the direct model and in the equivalent model are calculated with different methods at different frequencies and their results are presented from Fig. 5.14 to Fig. 5.19. Generally, the results show that the closer to the resonance, the less effective the equivalent

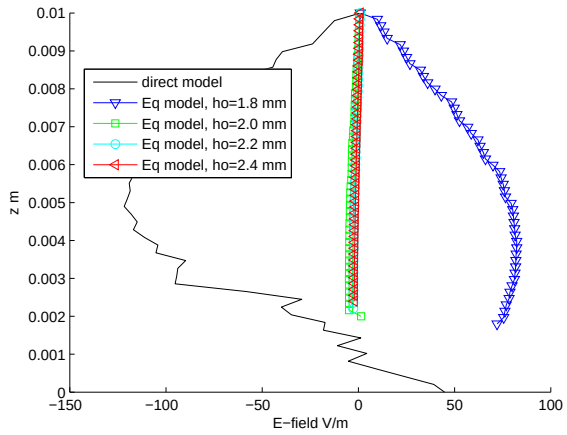

Figure 5.18: E-field in different models at 12 GHz. (The equivalent models are based on the surface impedance obtained by the Poynting flux method.)

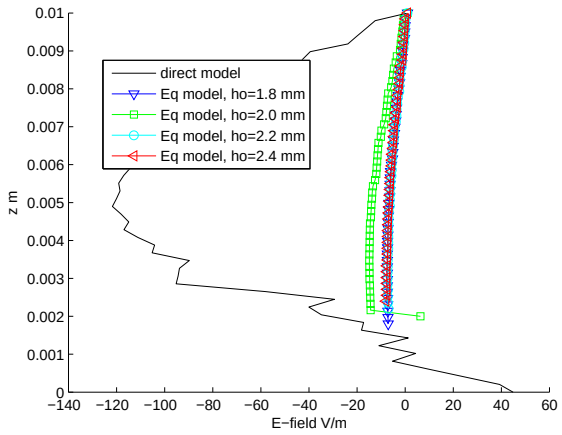

Figure 5.19: E-field in different models at 12 GHz. (The equivalent models are based on the surface impedance obtained by the <E>/<H> method.)

model will be. This phenomenon can be blamed on the poor condition number of the system matrix near the resonance, so it's better to avoid calculations around the resonance in the equivalent model.

When constructing the equivalent model, the surface impedance value can be obtained by two methods. Among the six figures, three correspond to the Poynting flux method, and the rest correspond to the <E>/<H> method. It is found that the variation of the observation surface's height has little influence when using the <E>/<H> method. On the other hand, the height of the observation surface can bring about a dramatic change of the results when using the Poynting flux method. The results show that the closer the observation surface to the HIS structure, the better the results.

Asymmetrical Structures

In the previous chapters, we studied some mushroom HIS structures with simple slot cuts. The structure with a rectangle slot inside or the one with a rectangle slot at the side are no longer symmetric, so their electromagnetic reactions to differently polarized excitations will not be the same.

In the case of the mushroom structure with a rectangle slot at the side, the resonance with x-oriented excitation is found at around 10 GHz, and the resonance with y-oriented excitation is at about 15GHz. Here, we will check the effectiveness of the equivalent models for asymmetric

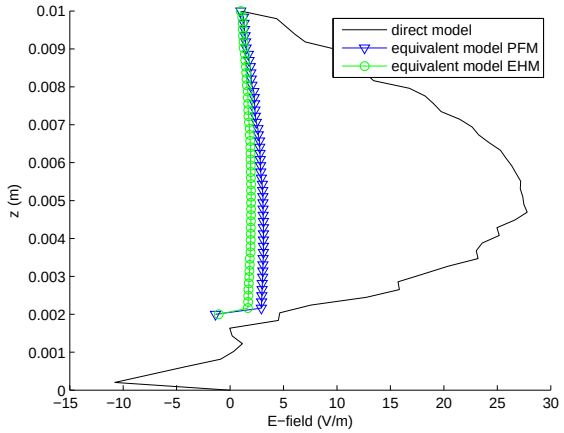

Figure 5.20: Comparison of E-field with an x-oriented excitation, at 10 GHz

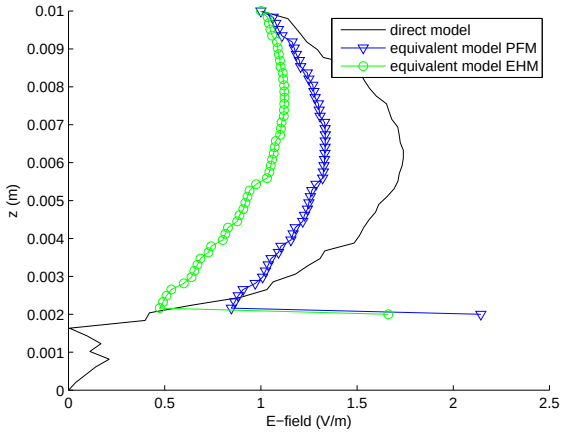

Figure 5.21: Comparison of E-field with a y-oriented excitation, at 10 GHz

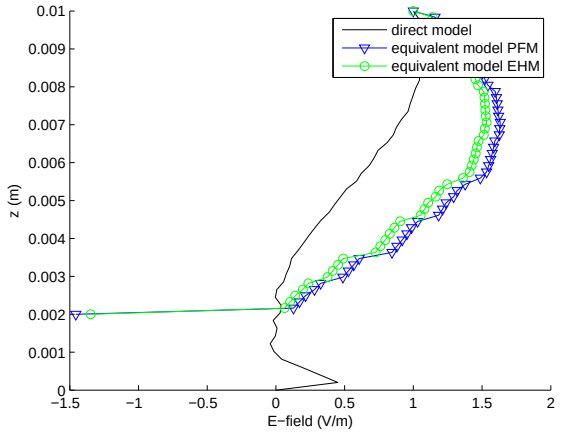

Figure 5.22: E-field in different models with an x-oriented excitation, at 15 GHz

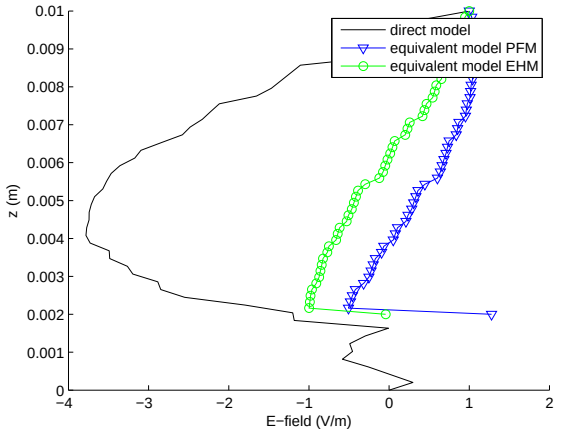

Figure 5.23: E-field in different models with a y-oriented excitation, at 15 GHz

structures.

The simulation results show that the equivalent model is effective a little away from the resonance, but not as good near the resonance. For example, at 10 GHz, the E-field detected in the equivalent model is far from the one in the direct model for an x-oriented excitation, as seen in Fig. 5.20. At 15 GHz, the E-field calculated in the equivalent model is less effective for a y-oriented excitation, as seen in Fig. 5.23. As one sees, the effectiveness of the equivalent model is not only related to the resonance but also related to the orientation of the excitation.

Accuracy Between Two Methods

During the construction of the equivalent model, the value of the surface impedance is obtained from the Poynting flux method or the <E>/<H> method. In Fig. 5.24 and in Fig. 5.25, we compare the E-field calculated in the direct model and in the equivalent model with these two different methods at 7 GHz and at 10 GHz. From these results, it is observed that the equivalent model is more effective when adopting the surface impedance value from the <E>/<H> method. Up to now, we didn't find a good explanation for this phenomenon.

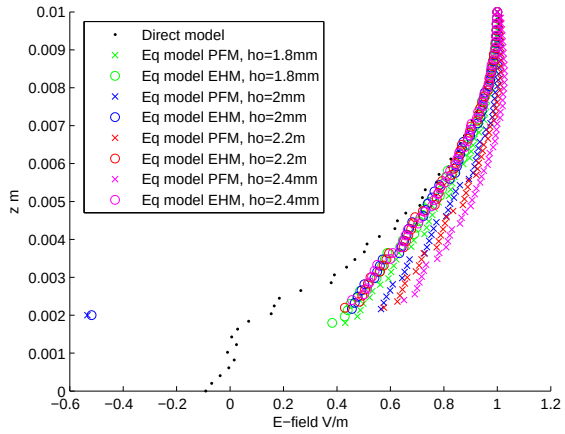

Figure 5.24: Comparison of the accuracy between the Poynting flux method and the <E>/<H> method. (An example with mushroom structure at 7 GHz.)

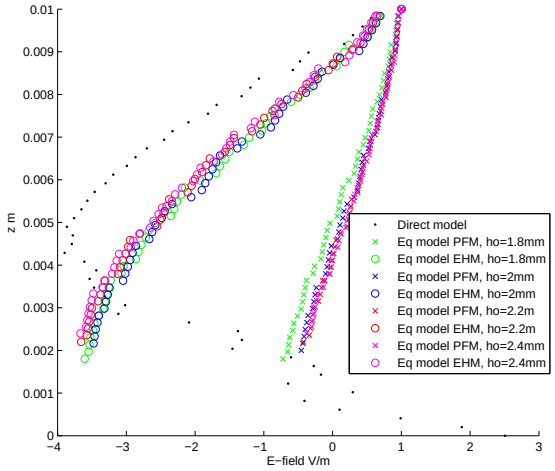

Figure 5.25: Comparison of the accuracy between the Poynting flux method and the <E>/<H> method. (An example with mushroom structure at 10 GHz.)

Moreover, we also compare the equivalent models built with the surface impedance values obtained at different observation surfaces. It is found that the <E>/<H> method is less sensitive to the influence of the observation surface height.

Permittivity of the Substance

In order to further investigate the effectiveness of the equivalent model, we also consider the case with a lossy HIS substrate. A relative permittivity $\varepsilon_r = 2 - j0.01$ is chosen for a mushroom structure. For a lossy structure, both the real part of the E-field and the imaginary part of the E-field should be observed.

Figure 5.26 and Figure 5.27 show that the equivalent model works well with a lossy substrate.

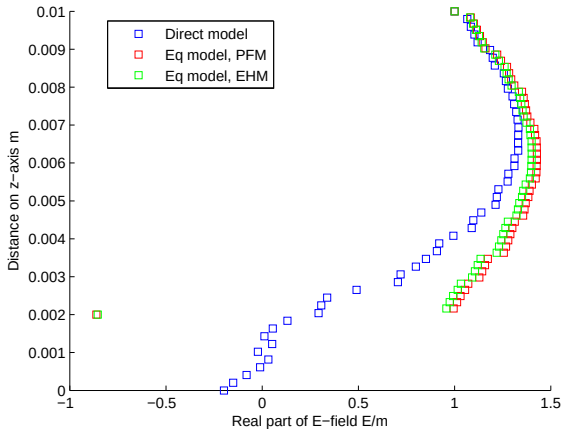

Figure 5.26: Comparison of the real part of E-field for a lossy HIS substrate, at 10 GHz

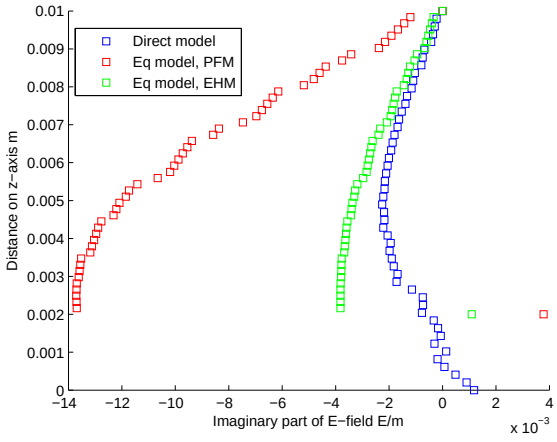

Figure 5.27: Comparison of the imaginary part of E-field for a lossy HIS substrate, at 10 GHz

Nevertheless, the equivalent model designed by using the surface impedance value obtained from the <E>/<H> method is less effective than the one obtained from the Poynting flux method.

Summary

In this chapter, we proposed an equivalent model for HIS structures: All the inhomogeneous HIS structures are replaced by an equivalent surface, characterized by the sheet impedance of the HIS structures. Before building the equivalent model, it takes some time to calculate the surface impedance value at each operating frequency in the direct model. However, calculating the electromagnetic fields in the equivalent model can save a lot of computing time and of core memory, compared with the calculation with the direct model. For instance, if one replaces the direct model for a one mushroom HIS structure by an equivalent model, the calculation of the electromagnetic field is reduced by a factor 10.

This equivalent model can be part of a simulation tool for designing the antenna, which would offer approximate results for the antenna's radiation pattern in a very short time. The mechanism of the design is that the frequency bandgap created by the HIS structures should cover the expected bandwidth of the antenna. Notice that the equivalent model works less effectively near the resonance of the HIS structures.

Chapter 6

Conclusions and Perspectives

Conclusions

In this thesis, several types of high impedance structures have been intensively studied. Emphasis has been on the numerical modeling of these structures by using the finite element method with edge elements. We proposed two numerical methods of calculating the surface impedance for HIS structures, which are applicable not only to symmetric structures, but to asymmetric ones as well. These two methods have been validated through various comparisons among the analytical, numerical and measurement results. Besides, the results obtained from these two methods became the base stone for building an equivalent model for HIS structures, which can reduce the complexity of the mesh in numerical modelling and thus save computing time. An equivalent model like this has been successfully set up in some simplified cases.

In the following part, we will recall the main points and discoveries of our work in this thesis in a concise way.

Our work began by a study on existing analytical modellings for several kinds of HIS structures. Analytical calculations can offer a quick view of HIS structure's characteristics, even though these predictions are less rigorous and more restricted to the structures with a simple geometry.

Then, a numerical modeling for HIS structures was built by using the finite element method based on edge elements and verified by two types of symmetric HIS structures: the mushroom structure and the Jerusalem-cross structure. These two structures have already been studied in analytical models and their analytical results are considered as references to check the validity of our numerical model. By comparing the phase of the reflection coefficient obtained from the analytical calculations and numerical calculations, our numerical model is proved to be effective.

In this process, we tested two schemes of modellings: one is semi-numerical and semi-analytical; another is totally numerical and based on the homogenization theory. The former scheme is discarded because of its inferior effectiveness, especially at high frequencies.

After successfully constructing the numerical model, a series of simulations have been made to analyze its performance. Results around the resonance were found less accurate, this being mainly due to the poor condition number of the stiffness matrix near the resonance. When handling the boundary conditions for the numerical model, two schemes were applied. The first scheme is a combination of the Perfect Electric Conducting boundary condition and the Perfect Magnetic Conducting boundary condition. This scheme has the advantage of easy programming and quick calculation which helps us to accomplish the first numerical calculation. However, this scheme is very sensitive to the asymmetric meshing and is not suitable for asymmetric HIS structures. Hence, the first scheme is not to be recommended and was abandoned in our later simulations. The second scheme applied two groups of periodic boundary conditions to the four lateral walls around the HIS unit cell. When choosing this scheme, one important condition should be satisfied: the meshing on the two corresponding faces must be totally identical. The advantage of this scheme is that it is not limited to asymmetric HIS structures and less sensitive to the asymmetry of the mesh.

For a symmetric HIS structure, the surface impedance's calculation can be simplified into a 1D problem. Since 1D calculation of the surface impedance does not suffice to exhibit the characteristics of an asymmetric HIS structures, new methods of calculating 2D surface impedance are required. Accordingly, we proposed two new numerical methods to calculate the surface impedance for HIS structures, expressed in the form of a 2×2 matrix. The Poynting flux method and the <E>/<H> method both interpret the surface impedance of HIS structure as an impedance boundary condition in a macro view. In simulations, symmetrical structures (Mushroom structures and Jerusalem-cross structures) and asymmetric structures (the rectangle structures, the spiral structures and the structures with slot-cut) were all tested. Furthermore, several samples have been fabricated and measured to verify the effectiveness of these numerical methods. Our numerical calculations are closer to the experimental results than the analytical calculations.

Finally, an equivalent model based on the surface impedance value is put forward, with the help of which the traditionally numerical model, composed of the whole detailed HIS structures, is simplified into an homogeneous impedance surface. As regards the direct model, this equivalent model is capable of calculating the electromagnetic radiation with less computing time and less core memory. Of course, the equivalent model offers only an approximate result,

but it's really attractive to see that the computing time can be largely reduced. For example, by replacing the mushroom HIS structures with an equivalent surface under the case of one unit cell, around 90% CPU time could be saved. Through the simulations, we also found that under most circumstances, the surface impedance value calculated by the <E>/<H> method is more effective than the one got by the Poynting flux method in building the equivalent model. Another important thing should be pointed out: the equivalent model is less effective when the operating frequency is close to the resonance. This phenomenon may also be blamed on the poor condition number in this situation.

In general, this equivalent model is very promising to be a part of an antenna design tool, which can give out a quick prediction of radiation patterns in a relatively short time.

Perspectives

In this thesis, the main contribution was to propose two numerical methods of calculating the 2D surface impedance of HIS structures. The numerical calculations have already been verified by experimental measurements and been used to characterize the HIS features, but there is still room for improvement. In this part, we will discuss a few ideas about how to improve on our numerical models.

Excitation of the numerical model

In our numerical model, the excitation is a plane wave with normal incidence. So, the first effort is going to consider an excitation with an oblique incidence. The second effort is to modify the constant E-field excitation to a TE or TM mode E-field excitation. These two improvements will make the numerical model a real full-wave simulation model and will contribute to get a more precise prediction for HIS properties.

Our equivalent model is only tested under a simplified condition of plane wave. The next effort can be to replace the E-field excitation by a real antenna, excited by an electrical current. This situation is closer to a real case and the effectiveness of this equivalent model can be more thoroughly checked. Under this case, the study domain should be enlarged with more HIS cells, at least enough for the structure to be larger than the antenna.

Design of the homogeneous surface in the equivalent model

In our conceit and test of the equivalent model, we propose a uniform surface characterized by the surface impedance on the basis of the hypothesis that the electromagnetic field on the

surface is homogeneous. However, with extremely asymmetric structures, this hypothesis will be less valid and may even fail to hold.

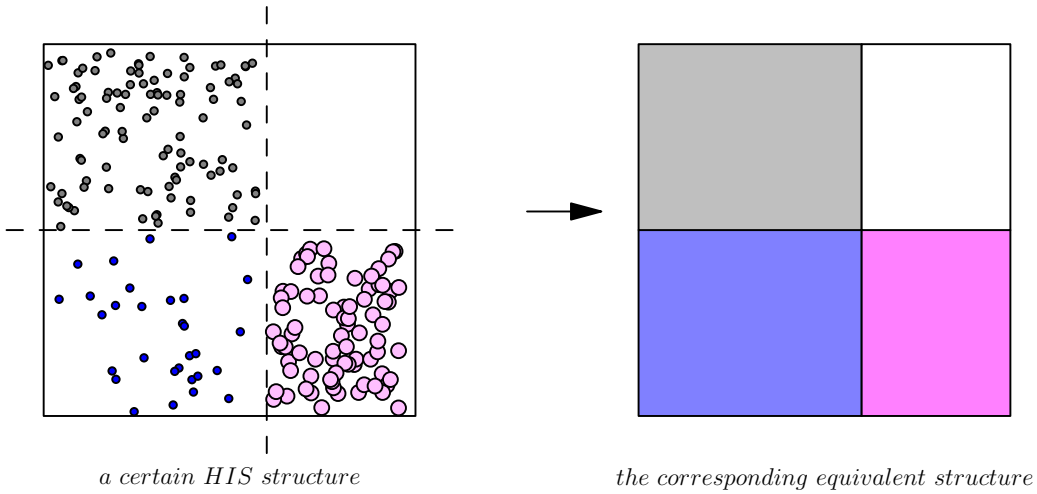

Figure 6.1: Geometry of one unit cell for the mushroom structure

The motivation for building this equivalent model is to save computing time and memory by highly reducing the mesh complexity. Hence, the surface can be divided into two, four or even more uniform sub-surfaces instead of a single uniform equivalent surface. The number and shape of these sub-surfaces depend on the original inhomogeneous distribution. Do a simulation with the original structures, observe the electromagnetic field distribution and decide how to design the sub-surfaces. An example is given in Fig. 6.1 and in this case, the equivalent surface is composed of four sub-surfaces. The surface impedance of each sub-surface can be separately calculated.

Effectiveness at the resonance

It is found that the numerical model is less effective around the resonance, both in the direct model and in the equivalent model. The deflation method may be used to improve the accuracy of the results near the resonance. The first eigen value should be calculated, for example by the iterated power method. Then the solution can be obtained by working in the subspace orthogonal to the eigenmode.

Applications

At the beginning, the numerical model was designed to characterize HIS structures. Afterward, we proposed the equivalent model, aiming at being a useful simulation tool for an antenna

design.

In fact, this model can also be used to study the propagation properties of a waveguide. As mentioned before, the HIS has already been used in designing the resonator and leaky wave antenna. So, our numerical model can also be useful in describing and analyzing such models with certain changes.

Besides, an accurate calculation for the surface impedance at an appropriate position can also create more equivalent models for all kinds of applications.

Bibliography

[1] C. Caloz, and T. Itoh, *Electromagnetic Metamaterials: Transmission Line Theory and Microwave Applications*, A John Wiley & son, Inc., Canada, 2006.

[2] A. Sihvola, "Electromagnetic emergence in metamaterials. Deconstruction of terminology of complex media", *Advances in Electromagnetics of Complex Media and Metamaterials, NATO Science Series II: Mathematics, Physics and Chemistry*, Kluwer Academic Publishers, vol. 89, pp. 1 - 17, 2003

[3] A. Sihvola, "Metamaterials in electromagnetics", *Metamaterials*, vol. 1, no. 1, pp. 2 - 11.

[4] A. Sihvola, "Metamaterials: A Personal View," *Radioengineering*, vol. 18, no. 2, pp. 90 - 94, 2009.

[5] D. R. Smith, "What are Electromagnetic Metamaterials?," *Novel Electromagnetic Materials*, Retrieved Auguest, 2010. http://people.ee.duke.edu/~drsmith/about_metamaterials.html.

[6] J. G. Webster, *Metamaterial*, Wiley Encyclopedia of Electrical and Electronics Engineering, Jan. 2010.

[7] V. G. Veselago, "The Eletrodynamics of Substances with Simultaneously Negative Values of ϵ and μ," *Sov. Phys. Usp*, vol. 10, pp. 509 - 514, 1968.

[8] I. V. Lindell, S. A. Tretyakov, K. I. Nikoskinen, and S. Ilvonen, "BW Media–Media with Negative parameters, Capable of Supporting Backward Waves," *Microwave Opt. Tech. Lett.*, vol. 31, no.2, pp. 129-133, 2001.

[9] J. B. Pendry, A. J. Holden, W. J. Stewart, and I. Youngs, "Extremely Low Frequency Plasmons in Metallic Mesostructures," *Phys. Rev. Lett.,* vol. 76, pp. 4773 - 4776, 1996.

[10] J. B. Pendary, A. J. Holden, D. J. Robbins, and W. J. Stewart, "Magnetism from Conductors and Enhanced Nonlinear Phenomena," *IEEE Trans. Microwave Theory Tech.*, vol. 47, pp. 2075 - 2084, 1999.

[11] D. R. Smith, W. Padilla, D. C. Viers, S. C. Nemat-Nasser, and S. Schultz, "A Composite Medium with Simultaneously Negative Permeability and Permittivity," *Phys. Rev. Lett.,* vol. 84, pp. 4184 - 4187, 2000.

[12] D. V. Smith, and J. B. Pendry, "Homogenization of Metamaterials by Field Averaging," *J. Opt. Soc, Qm.*, vol. 23, no. 3, pp. 391 - 403, 2006.

[13] J. B. Pendry, "Negative Refraction Makes a Perfect Lens," *Phys. Rev. Lett.,* vol. 85, pp. 3966 - 3969, 2000.

[14] M. C. K. Wiltshire, J. V. Hajnal, J. B. Pendry, D. J. Edwards, and C. J. Stevens, "Metamaterial Endoscope for Magnetic Field Transfer: Near Field Imaging with Magnetic Wires," *Optics Express*, vol. 11, no. 7, pp. 709 - 715, 2003.

[15] N. Katsarakis, T. Koschny, M. Kafesaki, E. N. Economou, and C. M. Soukoulis, "Electric Coupling to the Magnetic Resonance of Split Rring Resonators", *Applied Phys. lett.*, vol. 84, no. 15, pp. 2943 - 2945, 2004.

[16] D. Schurig, J. J. Mock, B. J. Justice, S. A. Cummer, J. B. Pendry, A. F. Starr, and D. R. Smith, "Metamaterial Electromagnetic Cloak at Microwave Frequencies," *Science*, vol. 314, no. 5801, pp. 977 - 980, 2006.

[17] A. Alu, and N. Engheta, "Polarizabilities and Effective Parameters for Collections of Spherical Nanoparticles Formed by Pairs of Concentric Double-Negative, Single-Negative, and/or Double-Positive Metamaterial Layers," *Journal of Applied Physics*, vol. 97, no. 9, pp. 094310 1 - 12, 2005.

[18] S. F. Mahmoud, "A New Miniaturized Annular Ring Patch Resonator Partially Loaded by a Metamaterial Ring with Negative Permeability and Permittivity," *IEEE Antennas and Wireless Propagation Letters*, vol. 3, pp. 19 - 22, 2004.

[19] A. Alu, M. G. Silveirinha, A. Salandrino, and N. Engheta, "Epsilon-Near-Zero Metamaterials and Electromagnetic Sources: Tailoring the Radiation Phase Pattern," *Physical Review B*, vol. 75, no. 15, 2007.

[20] C. Caloz, T. Itoh, "Metamaterials for High-Frequency Electronics," *Proceedings of the IEEE*, vol. 93, no. 10, pp. 1744-1752, Oct. 2005 .

[21] H. Raether, *Surface Plasmons on Smooth and Rough Surfaces and on Gratings*, Springer-Verlag, New York, 1988.

[22] D. F. Sievenpiper, *High Impedance Electromagnetic Surfaces*, Ph.D. dissertation, Electrical Engineering Department, University of California, Los Angeles, 1999.

[23] R. Elliot, "On the Theory of Corrugated Plane Surfaces", *IRE Trans. Ant. Prop.*, vol. 2, pp. 71 - 81, 1954.

[24] W. Rotman, "A Study of Single-Surface Corrugated Guides", *Proc. IRE*, vol. 39, pp. 952 - 959, 1951.

[25] P.-S. Kildal, "Artificially Soft and Hard Surfaces in Electromagnetics", *IEEE Trans. Ant. Prop.*, vol. 38, pp. 1537 - 1544, 1990.

[26] S. Lee, and W. Jones, "Surface Waves on Two-Dimensional Corrugated Surfaces", *Radio Science*, vol. 6, pp. 811, 1971.

[27] E. Yablonovitch, "Inhibited Spontaneous Emission in Solid-State Physics and Electronics," *Physical Review Letters*, vol. 58, no. 20, pp. 2059-2062, 1987.

[28] W. Barnes, T. Priest, S. Kitson, J. Sambles, "Photonic Surfaces for Surface-Plasmon Polaritons", *Phys. Rev. B*, vol. 54, pp. 6227, 1996.

[29] S. Kitson, W. Barnes, J. Sambles, "Full Photonic Band Gap for Surface Modes in the Visible", *Phys. Rev. Lett.* , vol. 77, pp. 2670, 1996.

[30] L. Brillouin, *Wave Propagation in Periodic Structures; Electric Filters and Crystal Lattices*, 2nd ed., Dover Publications, New York (1953)

[31] F. Yang, and Y. Rahmat-Samii, "Reflection Phase Characterizations of the EBG Ground Plane for Low Profile Wire Antenna Applications," *IEEE Trans. on Antennas Propag.*, vol. 51, no. 10, Oct. 2003.

[32] J. R. Sohn, H. S. Tae, J. G. Lee, and J. H. Lee, "Comparative Analysis of Four Types of High Impedance Surfaces for Low Profile Antenna Applications," *Ant. and Propagat. Society International Symposium*, vol. 1A, pp. 758 - 761, 2005.

[33] H. Mirshahram, and Q. Wu, "Miniaturised High-Impedance Surface with High Angular Stability of Resonant Frequency", *Electronic letters*, vol. 45, no. 24, pp. 1204-1206, Nov.,2009.

[34] H. Sagan, *Space-Filling Curves*, Springer-Verlag, New York, 1994.

[35] J. Mcvay, N. Engheta, and A. H. Far, "High Impedance Metamaterial Surfaces Hsing Hilbert-Curve Inclusions," *IEEE Microwave and Wireless Components Letters*, vol. 14, no. 3, pp. 130 - 132, 2004.

[36] Y. Li, M. Y. Fan, F. L. Chen, J. Z. She, and Z. H. Feng, "A Novel Compact Electromagnetic- Bandgap (EBG) Structure and Its applications for Microwave Circuits", *IEEE Trans. Microw. Theory Tech.*, vol. 53, no. 1, Jan. 2005.

[37] D. J. Kern, D. H. Werner, A. Monorchio, L. Lanuzza, and M.J. Wilhelm, "The Design Synthesis of Multiband Artifical Magnetic Conductors Using High Impedance Frequency Selective Surfaces", *IEEE Trans. Antennas and Propagat.*, vol. 53, no. 1, Jan. 2005.

[38] M. Silveirinha, and C. A. Fernandes, "Realization of Low Profile High-Impedance Surfaces Using an Array of Densely Packed Crossed Metallic Wires", *Proceedings of 2007 IEEE Antennas and Propagation Society International Symposium*, pp. 1337 - 1340, Honolulu, HI, June 2007.

[39] S. Tse, H. Yang, and C. Parini, "Mushroom-Like High-Impedance Surface (HIS) with Slanted VIAS", *Antennas and Propagation Conference*, pp. 309 - 312, Loughborough, 2007.

[40] G. Zheng, Z. Y. Yu, and B. Z. Wang, "A Simple Theory Model of High Impedance Surface and Application", *Proceedings of 2005 Asia-Pacific Microwave Conference,* SuZhou, 2005.

[41] N. Capet, C. Martel, J. Sokoloff, and O. Pascal, "Study of the Behaviour of a Two Layered High Impedance Surface with Electromagnetic Band Gap", *Proceedings of the Fourth European Conference on Antennas and Propagation (EuCAP)*, Barcelona, Spain, April 2010.

[42] N. Clow, I. Morrow, and A. S. Fairweather, "Polarisation Properties of Electrically Small Antennas on High Impedance Surfaces", *2008 Institution of Engineering and Technology Seminar on Wideband, Multiband Antennas and Arrays for Defence or Civil Applications*, pp. 181 - 188, London, 2008.

[43] S. P. Benham, T. J. Murphy, E. J. Totten, D. J. Knights, and M. Schick, "EM Modelling Design of a Conformal IFF system on an Aircraft", 2010 Proceedings of the European Conference on Antennas and Propagation (EuCAP), Barcelona, Spain, April 2010.

[44] P. Deo, A. Mehta, D. Mirshekar-Syahkal, P. J. Massey, and H. Nakano, "Tickness Reduction and Performance Enhancedment of Steerable Square Loop Antenna Using Hybrid Hhigh Impedance Surface," *IEEE transaction on antennas and propagation*, vol 58, No 5, may 2010

[45] F. Costa, A. Monorchio, S. Talarico, and F. M. Valeri, "An Active High-Impedance Surface for Low-Profile Tunable and Steerable Antennas", *IEEE Antennas Wireless Propag. Lett.*, vol 7, pp. 676 - 680, 2008.

[46] L. Yousefi, B. Mohajer-Iravani, and O. M. Ramahi, "Enhanced Bandwidth Artificial Magnetic Ground Plane for Low-profile Antennas", *IEEE Antennas Wireless Propag. Lett.*, vol. 6, pp. 289-292, 2007.

[47] H. Q. Li, Y. Q. Qin, Z. W. Wei, H. Chen, Y. W. Zhang, L. Zhou, and C. T. Chan, "Directive Metamaterial Antenna Using High Impedance Surface," *Proceedings of the 4th International Conference on Microwave and Millimeter Wave Technology (ICMMT)*, pp. 480 - 482, Aug. 2004.

[48] O. Luukkonen, A.O. Karilainen, J. Vehmas, C. Simovski, and S. A. Tretyakov, "a High Impedance Surface Based Antenna Lose the Antenna", *Proceedings of the Fourth European Conference on Antennas and Propagation (EuCAP)*, 12-16 April 2010, Barcelona.

[49] D. B. Lin, K. C. Hung, C.T. Wu, C. S. Chang, "Partial Uniplanar Compact Electromagnetic Bandgap Combined with High-Impedance Surface to Suppress Simultaneous Switching Noise", *Electronics Letters*, pp. 829-830, 2009.

[50] T. Kamgaing, and O. M. Ramahi, "Design and Modeling of Hig-Impedance Electromagnetic Surfaces for Switching Noise Suppression in Power Planes", *IEEE Trans. Electomagn. Compat.*, vol. 47, no. 3, Aug. 2005.

[51] N. Capet, C. Martel, J. Sokoloff, O. Pascal, "Reduction of the Mutual Coupling Between Two Adjacent Patches Using Various Ideal High Impedance Surface Positionings", *Proceedings of the 3rd European Conference on Antennas and Propagation (EuCAP)*, pp. 3151-3154, Berlin, Germany, 2009.

[52] M. S. Lin, C. H. Huang, and C. I-G. Hsu, "Techniques of Evaluating High Impedance Surfaces Used for SAR Reduction", *2010 asia pacific international symposium on electromagnetic compatibility*, Beijing, China, April 12-16 2010.

[53] S.A. Tretyakov, and S.I. Maslovski, "Thin Absorbing Structure for All Incidence Angles Based on The Use of High-Impedance Surface", *Microw. Opt. Technol. Lett.*, vol. 38, no. 3, Aug. 2003.

[54] L. Li, B. Li, H.-X. Liu, C.-H. Liang, "Locally Resonant Cavity Cell Model for Electromagnetic Band Gap Structures," *IEEE Transactions on Antennas and Propagation*, vol. 54, no. 1, pp. 90-100, 2006.

[55] P. Monk, *Finite Element Methods for Mawwell's Equations*, Clarendon Press, Oxford, 2003.

[56] W. C. Chew, *Waves and Fields in Inhomogenous Media*, Van Nostrand Teinhold, New York, 1990.

[57] J. A. Kong, *Maxwell Equations*, EMW Publishing, Cambridge, MA, 2002.

[58] R. P. Feynman, R. B. Leighton, and M. Sands, *The Feynman Lectures on Physics*, Addison-Wesley, Redwood City, CA, 1989.

[59] J.A. Kong, "Reciprocity relationships for bianisotropic media", Proceedings of IEEE (Letters), vol. 58, no. 12, pp. 1966-1967, 1970.

[60] J. D. Jackson, *Classical Electrodynamics*, 3rd edition, John Wiley & Sons, New York, 1998.

[61] R.F.Harrington, *Time-Harmonic Electromagnetic Fields*, McGraw-Hill, New York, 1961, (p. 34).

[62] J. P. A. Bastos, and N. Sadowski, *Electromagnetic Modelling by Finite Element Methods*, Marcel Dekker, Inc., USA, 2003.

[63] W. K. Saunders, "On Solutions of Maxewell Equations in an Exterior Region," *Proceedings of the National Academy of Sciences*, vol. 38, pp. 342-348, 1952.

[64] A. C. Polycarpou, *Introduction to the Finite Element Method in Electromagnetics*, Morgan & Claypool, USA, 2006.

[65] A. Bossavit, "Whitney forms: A Class of Finite Elements for Three-Dimensional Computations in Electromagnetism," *IEEE proceedings on Physical Science, Measurement and Instrumentation, Management and Education - Reviews A*, vol. 135, no. 8, pp. 493 - 500, Nov. 1988.

[66] H. Whitney, *Geometric Integration Theory*, Princeton University Press, Princeton, 1957.

[67] G. Dhatt, G. Touzot , E. Lefrançois, *Méthode des Elément Finis*, Hermes Science Publications, 2005.

[68] R. Gonzalo, P. D. Maagt, and M. Sorolla, "Enhanced Patch-Antenna Performance by Suppressing Surface Waves Using Photonic-Bandgap Substrates," *IEEE Trans. Microwave Theory Tech.*, vol. 47, no. 11, pp. 2131 - 2138, Nov. 1999.

[69] D. Sievenpiper, J. Schaffner, R. Loo, G. Tangonan, S. Ontiveros, and R. Harold, "A Tunable Impedance Surface Performing As a Reconfigurable Beam Steering Reflector," *IEEE Trans. Antennas Propag.*, vol. 50, no. 3, pp. 384–390, Mar. 2002.

[70] D. Sievenpiper, L. Zhang, R. Broas, and N. G. Alexopoulos, "High-impedance Electromagnetic Surfaces with a Forbidden Frequency Band," *IEEE Trans. Microwave Theory Tech.*, vol.47, no. 11, pp. 2059 - 2074, Nov. 1999.

[71] R. F. J. Broas, D. F. Sievenpiper, and E. Yablonovitch, "An Application of High Impedance Ground Planes to Phased Array Antennas," *IEEE Trans. Microwave Theory Tech.*, vol. 53, no. 4, pp. 1377 - 1381, April 2005.

[72] R. Baggen, M. Martinez-Vazquez, J. Leiss, S. Holzwarth, L. S. Drioli, and P. de Maagt, "Low Profile GALILEO Antenna Using EBG Technology," *IEEE Trans. Antennas Propag.*, vol. 56, no. 3, pp. 667 - 674, March 2008.

[73] D. J. Kern, D. H. Werner, A. Monorchio, L. Lanuzza, and M. J. Wilhelm, "The Design Synthesis of Multiband Artifical Magnetic Conductors Using High Impedance Frequency Selective Surfaces", *IEEE Trans. Antennas and Propagat.*, vol. 53, no. 1, Jan. 2005.

[74] G. G. MacFarlane, "Surface Impedance of an Infinite Wire Grid, at Oblique Angles of Incidence," *J. IEE*, vol. 93 (III E), pp. 1523 - 1527, Dec. 1946.

[75] J. R. Wait, "Reflection at Arbitrary Incidence From a Parallel Wire Grid," *Appl. Sci. Research*, vol. B4, pp. 393–400, 1955.

[76] G. von Trentini, "Gratings as circuit elements of electric waves in space," *Zeit. angew. Phys.*, vol. 5, pp. 221–231, June 1953.

[77] S.-W. Lee, G. Zarrillo, and C.-L. Law, "Simple Formulas for Transmission Through Periodic Metal Grids or Plates," *IEEE Trans. Antennas Propag.*, vol. AP-30, no. 5, pp. 904 - 909, 1982.

[78] M. Rahman, and M. A. Stuchly, "Transmission Line - Periodic Circuit Representation of Planar Microwave Photonic Bandgap Structures," *Microwave Optical Tech. Lett.*, vol. 30, no. 1, 15 - 19, 2001.

[79] C. R. Simovski, P. de Maagt, and I. V. Melchakova, "High-Impedance Surface Having Stable Resonance With Respect to Polarization and Incidence Angle", *IEEE Trans. Antennas Propagat.*, Vol. 53, No. 3, March 2005.

[80] S. A. Tretyakov, and C. R. Simovski, "Dynamic Model of Artificial Reactive Impedance Surfaces", *J. of Electromagn. Waves and Appl.*, vol. 17, no. 1, pp. 131 - 145, 2003.

[81] M. Hosseini, and M.Hakkak, "Characteristics Estimation for Jerusalem Cross-Based Artificial Magnetic Conductors", *IEEE Antennas and wireless propagation letters*, vol. 7, pp. 58 - 61, 2008.

[82] S. A. Tretyakov, *Analytical Modeling in Applied electromagnetics*, Boston, MA: Artech House, 2003.

[83] O. Luukkonen, A. B. Yakovlev, C. R. Simovski, and S. A. Tretyakov, "Comparative study of surface waves on highimpedance surfaces with and without vias", *Proceedings of the 2008 IEEE APS International Symposium on Antennas and Propagation (APS)*, pp. 326-329, San Diego, California, USA, July 2008.

[84] R. C. Compton, L. B. Whitbourn, and R. C. McPherdan, "Strip Gratings at a Dielectric Interface and Application of Babinet's Principle," *Appl. Opt.*, vol. 23, no. 18, pp. 3236 - 3242, Sep. 1984.

[85] S. A. Tretyakov, C. R. Simovski, "Dynamic Model of Artificial Reactive Impedance Surfaces", *J. of Electromagn. Waves and Appl.*, vol. 17, no. 1, pp. 131 - 145, 2003.

[86] C. R. Simovski, and A. A. Sochava, "High-Impedance Surfaces Based on Self-Resonant Grids: Analytical Modelling Numerical Simulations," *Progr. Electromagn. Res. PIER 43*, 239 - 256, 2003.

[87] O. Luukkonen, C. R. Simovski, G. Granet, G. Goussetis, D. Lioubtchenko, A. V. Raisanen, and S. A. Tretyakov, "Simple and Acurate Analytical Model of Planar Grids and High-Impedance Surfaces Comprising Metal strips or Patches", *IEEE Trans. Antennas Propagat.*, vol. 56, No. 6, June, 2008.

[88] H. Lamb, "On the Reflection and Transmission of Electric Waves by a Metallic Grating," *Proc. Math. Soc.*, Ser. 1, vol. 29, pp. 523 - 544, London, 1898.

[89] I. Andersson, "On the Theory of Self-Resonant Grids," *The Bell System Techical Journal*, vol. 55, pp. 1725 - 1731, 1975.

[90] D. B. Davidson, *Computational Electromagnetics for RF and Microwave Engineering*, Cambridge University Press, Cambridge, UK, 2005.

[91] Y. Hao, R. Mittra, *FDTD Modeling of Metamaterials Theory and Applications*, Artech house, 2009, USA.

[92] J. M. Vay, A. Hoorfar, and N. Engheta, "Radiation Characteristics of Microstrip Dipole Antennas Over a High Impedance Metamaterial Surface Made of Hilbert Inclusions", *IEEE 2003 MTT-S International Microwave Symposium digest*, vol. 1, pp. 587 - 590, 2003.

[93] J. M. Jin, *The Finite Element Method in Electromagnetics*, John Wiley&Sons, Inc., New York, 2002.

[94] W. Pereira Carpes Junior, *Modélisation Tridimensionnelle Par Elements Finis Destinée Aux Analyses de Propagation d'Ondes et de Compatibilité Electromagnetique*, Ph.D. thesis, Univ. Paris Sud, Orsay, Juin, 2000.

[95] A. Bossavit, *Computational Electromagnetism*, Acdamic Press, USA, 1998.

[96] A. Bossavit, "Solving Maxwell Equations in a Closed Cavity, and the Question of 'Spurious Modes"', *IEEE Trans. Magnetics*, vol. 26 (2), pp. 702 - 705, 1990.

[97] K. Guilllouard, M.-F Wang, V.-F. Hanna, and J. Citerne, "A New Global Finite Element Analysis of Microwave Circuits Including Lumped Element," *IEEE Trans. Microw. Theory Tech.*, vol 44, no. 12, pp2587-2594, 1996.

[98] P. Curie: "Sur la Symétrie dans les Phénomènes Physiques, Symétrie d'un Champ Electrique et d'un Champ Magnétique", *Journal de Physique.*, Série 3(3), pp. 393-415, 1894.

[99] http://en.wikipedia.org/wiki/Condition_number.

[100] K. Chen, "Matrix Preconditioning Techniques and Applications," *Monographs on Applied and Computational Mathematics*, Cambridge University Press, 2005.

[101] COMSOL Multiphysics v3.4.

[102] O. Luukkonen, *Artifical Impedance Surfaces*, Ph.D. dissertation, Department of Radio Science and Engineering, Helsinki University of Technology, Finland, 2009.

[103] M. Bern, D. Eppstein, J. Gilbert: "Provably Good Mesh Generation", *J. Comp. System Sc.*, no. 48, pp. 384-409, 1994 .

[104] E.W. Seltmann, J. Laskar, K. Smith, R. Gleason, "A Coplanar Waveguide Probe with Applications to Thin Film Dielectric Measurements," *Electrical Performance of Electronic Packaging*, 2-4 Oct 1995.

[105] C. N. Works, T. W. Dakin, F. W. Boggs, "A Resonant-Cavity Method for Measuring Dielectric Properties at Ultrahigh Frequencies", *Transactions of the American Institute of Electrical Engineers*, vol. 63, no. 12, pp. 1092-1098, Dec. 1944.

[106] D. Popovic, C. Beasley, M. Lazebnik, M. Okoniewski, S. C. Hagness, and J. H. Booske. "Precision Open-ended Coaxial Probes for In Vivo and Ex Vivo Dielectric Spectroscopy of Biological Tissues at Microwave Frequencies," *IEEE Transactions on Microwave Theory and Techniques*, vol. 53, no. 5, pp. 1713-1722, 2005.

[107] P. F. Goldsmith, "Quasioptical techniques offer advantages at millimeter frequencies," *Microwave Systems News*, vol. 13, pp. 65 - 84, 1983.

[108] M. H. Belyamoun, *Modélisation et Caractérisation Spectrale de Métamatériaux*, Ph. D. dissertation, Sciences mécaniques, acoustique et électronique de Paris, l'Université Pierre et Marie Curie, 2010.

[109] Agilent Technologies, *Time domain analysis using a network analyser*, Application Note, Agilent, 2007.

[110] F. Yang, and Y. Rahmat-Samii, *Electromagnetic Band Gap Structures in Antenna Engineering*, Cambridge University Press, 2009.

[111] K.-P. Ma, K. Hirose, F.-R. Yang, Y Quian and T.Itoh, "Realization of Magnetic Conducting Surface Using Novel Photonic Bandgap Structure," *Electron. Lett.*, vol.34, no.21, pp. 2041-2042, Oct. 1998.

[112] A. Ishimaru, *Electromagnetic Wave propagation, Radiation, and Scattering.* New Jersey: Prentice hall, 1991.

[113] P. M. T. Ikonen, K. N. Rozanov, A. V. Osipov, P. Alitalo, and S. A. Tretyakov, "Magnetodielectric Substrates in Antenna Miniaturization : Potential and Limitations", *IEEE Trans. Antennas Propag.*, vol. 54 (2), No.11, pp. 3391-3399, 2006.

[114] F. Yang, and Y. Rahmat-Samii, "Microstrip Antennas Integrated with Electromagnetic Band-Gap (EBG) Structures: A Low Mutual Coupling Design for Array Applications," *IEEE Trans. Antennas Propag.*, vol. 51, no. 10, pp. 2936–2946, Oct. 2003.

[115] N. Ida, and J. P. A. Bastos, *Electromagnetics and Calculations of fields*, Springer-Verlag, New York, 1997.

[116] H. Wu, and A. C. Cangellaris, "Model-Order Reduction of Finite-Element Approximations of Passive Electromagnetic Devices Including Lumped Electrical-Circuit Models," *IEEE Trans. Microwave Theory and Techniques*, vol. 52, no. 9, pp. 2305-2313, Sep. 2004.

[117] K. Guillouard, M.-F. Wong, V. F. Hanna, and J. Citerne, "A New Global Finite Element Analysis of Microwave Circuits Including Lumped Elements," *IEEE Trans. on Microwave Theory and Tecniques*, vol. 44, no. 12, pp. 2587-2594, Dec. 1996.

Publication

International Journal

- Y. Zhu, A. Bossavit, and S. Zouhdi, "Surface Impedance Models for High Impedance Surfaces", *Journal of Applied Physics*, vol. 103, no. 3, pp. 677-683, June, 2011.

International Conference

- Y. Zhu, A. Bossavit, Y. Duval, and S. Zouhdi, "Numerical Models, Based on the Finite Element Method, for Asymmetric High Impedance Surfaces", the 29th PIERS, Marrakesh, Morocco, 20-23/03/2011.
- Y. Zhu and S. Zouhdi, "Calculation of Surface Impedance for High Impedance Surface," META'10, 2nd international Conference on Metamaterial, Photonic crystals and plasmonics, Cario, Egypt, 22-25/02/2010.
- Y. Zhu, C.-W, Qiu and S. Zouhdi, "An Homogenization Model for High Impedance surface," 2009 IEEE AP-S International Symposium and USNC/URSI National Radion Science Meeting, Charleston, USA, 1-5/06/2009.
- Y. Zhu, O. Ouchetto, C.-W. Qiu, L. Santandrea and S. Zouhdi, "An Effective Lumped Impedance Surface for HIS", META'08, NATO ARW on Metamaterials for Secure Information Technologies, Marrakesh, Morocco, 7-10/05/2008.